SAND91-2228
Unlimited Release
Printed July 1992

Measured Data for the Sandia 34–Meter Vertical Axis Wind Turbine

Tom D. Ashwill

Prepared by
Sandia National Laboratories
Albuquerque, New Mexico 87185 and
Livermore, California 94550
for the United States Department of Energy
under Contract DE-AC04-76DP00789

Issued by Sandia National Laboratories, operated for the United States Department of Energy by Sandia Corporation.

Available to DOE and DOE contractors from
Office of Scientific and Technical Information
PO Box 62
Oak Ridge, TN 37831

Prices available from (615) 576-8401, FTS 626-8401

Available to the public from
National Technical Information Service
US Department of Commerce
5285 Port Royal Rd
Springfield, VA 22161

NTIS price codes
Printed copy: A03
Microfiche copy: A01

Distribution
Category UC-261

SAND91-2228
Unlimited Release
Printed July 1992

MEASURED DATA FOR THE SANDIA 34-METER VERTICAL AXIS WIND TURBINE

by

Thomas D. Ashwill

Wind Energy Research Division
Sandia National Laboratories
Albuquerque, New Mexico 87185

ABSTRACT

The 34-meter Test Bed is a research-oriented, variable-speed vertical-axis wind turbine located at the USDA Agricultural Research Station in Bushland, Texas. Sandia National Laboratories designed and built this machine to perform research in structural dynamics, aerodynamics, and fatigue. Testing to determine its performance in various wind conditions and rotation rates has been ongoing for over three years. This report documents a broad range of test data and includes comparisons to analytical results.

Table of Contents

Page

LIST OF TABLES vii

LIST OF FIGURES vii

LIST OF APPENDICES xi

1.0 INTRODUCTION 1

1.1 Scope 3
1.2 Turbine Testing 4

2.0 INSTRUMENTATION 6

2.1 Ground-based Instrumentation 6
2.2 Rotor-based Instrumentation 6
2.3 Data Acquisition and Analysis System 8

3.0 AERODYNAMIC PERFORMANCE 12

3.1 Tare and Zero-Wind Drag Measurements 12
3.2 Transmission (Gearbox) and Generator Losses 13
3.3 Performance Data 14
3.3.1 28 RPM 14
3.3.2 34 RPM and 38 RPM 21
3.3.3 Effects of Joint Fairings and Bug Contamination 32

4.0 STRUCTURAL PERFORMANCE 36

4.1 Gravity Stresses 36
4.2 Centrifugal Stresses 36
4.3 Natural Frequencies 38
4.4 Vibratory Stresses 38

5.0 SELECTED TIME HISTORIES AND STRESS AMPLITUDE SPECTRA .. 50

5.1 Start-up Torque 50
5.2 Normal Operation 50
5.3 Braking Data 50
5.4 Torque Ripple 58
5.5 Stress Amplitude Spectra 58

SUMMARY 63

ACKNOWLEDGEMENTS 67

REFERENCES 68

APPENDICES 70

List of Tables

		Page
Table I.	Test Bed Specifications	2
Table II.	Measurement Channels	10
Table III.	Performance Data - 28 RPM	20
Table IV.	Performance Data - 34 RPM	25
Table V.	Performance Data - 38 RPM	29
Table VI.	Performance Data Summary	30
Table VII.	Performance Data with Joint Fairings - 28 RPM	34
Table VIII.	Performance Data with Bug Contamination and Joint Fairings - 28 RPM	35
Table IX.	Parked Modal Frequencies (Hz) - Test and Analysis	40
Table X.	Test Bed Strain Gauges	41
Table XI.	Summary of RMV Stresses (MPa) at 28 RPM	44
Table XII.	Summary of RMV Stresses (MPa) at 34 RPM	45
Table XIII.	Summary of RMV Stresses (MPa) at 38 RPM	46

List of Figures

Figure 1.1.	34-m Test Bed	1
Figure 1.2.	Blade Shape Geometry	3
Figure 2.1.	Test Bed Instrumentation	7

Figure 2.2. Test Site Layout 7

Figure 2.3. Data Acquisition System 9

Figure 3.1. Rotor Torque vs. Wind Speed at 28 RPM 15

Figure 3.2. Rotor Power vs. Wind Speed at 28 RPM 15

Figure 3.3. C_p vs. Tip Speed Ratio at 28 RPM 18

Figure 3.4. K_p vs. Advance Ratio at 28 RPM 18

Figure 3.5. Bin Entry Distribution at 28 RPM 19

Figure 3.6. Rotor Torque vs. Wind Speed at 34 RPM 22

Figure 3.7. Rotor Power vs. Wind Speed at 34 RPM 22

Figure 3.8. C_p vs. Tip Speed Ratio at 34 RPM 23

Figure 3.9. K_p vs. Advance Ratio at 34 RPM 23

Figure 3.10. Bin Entry Distribution at 34 RPM 24

Figure 3.11. Rotor Torque vs. Wind Speed at 38 RPM 26

Figure 3.12. Rotor Power vs. Wind Speed at 38 RPM 26

Figure 3.13. C_p vs. Tip Speed Ratio at 38 RPM 27

Figure 3.14. K_p vs. Advance Ratio at 38 RPM 27

Figure 3.15. Bin Entry Distribution at 38 RPM 28

Figure 3.16. Rotor Power vs. Wind Speed at 28 RPM - Calculated and Measured 31

Figure 3.17. Rotor Power vs. Wind Speed at 34 RPM - Calculated and Measured 31

Figure 3.18. Effects of Joint Fairings on Rotor Power at 28 RPM 33

Figure 3.19. Effects of Bug Contamination on Rotor Power at 28 RPM 33

Figure 4.1. Gravity Stress Distribution 37

Figure 4.2. Upper Root, Flatwise Stress vs. RPM 37

Figure 4.3. Centrifugal Stress Distribution at 28 RPM 39

Figure 4.4. Centrifugal Stress Distribution at 40 RPM 39

Figure 4.5. Rotating Modal Frequencies - Measured and Predicted 40

Figure 4.6. Strain Gauge Locations 42

Figure 4.7. Upper Root, Flatwise RMV Stress vs. Wind Speed at 28 RPM 42

Figure 4.8. Lower Root, Flatwise RMS Stress vs. Wind Speed - Measured and Analytical (FFEVD) Without Turbulence 48

Figure 4.9. Lower Root, Trailing Edge RMS Stress vs. Wind Speed - Measured and Analytical (FFEVD) Without Turbulence 48

Figure 4.10. Lower Root, Flatwise RMS Stress vs. Wind Speed - Measured and Analytical (TRES4) With Turbulence 49

Figure 4.11. Lower Root, Trailing Edge RMS Stress vs. Wind Speed - Measured and Analytical (TRES4) With Turbulence 49

Figure 5.1. Turbine Start and Ramp-up to 28 RPM 51

Figure 5.2. Torque during Start-up 51

Figure 5.3. Normal Operation at 34 RPM - 200 Second Interval 52

Figure 5.4. Normal Operation at 34 RPM - Flatwise and Trailing Edge Gauges 52

Figure 5.5. Stress Amplitude Spectra (4 Blocks) for an Upper Root, Trailing Edge Gauge at 34 RPM 53

Figure 5.6. Stress Amplitude Spectra (4 Blocks) for an Upper Root, Flatwise Gauge at 34 RPM 53

Figure 5.7. Torque during Normal Stop 55

Figure 5.8. Blade Stresses during Normal Stop 55
Figure 5.9. Torque during Alarm Stop from 40 RPM 56
Figure 5.10. Blade Stresses during Alarm Stop 56
Figure 5.11. Torque during Emergency Stop from 28 RPM 57
Figure 5.12. Blade Stresses during Emergency Stop 57
Figure 5.13. Turbine Stand and Drive Train 59
Figure 5.14. Torque Time History at 28 RPM 60
Figure 5.15. System Power Time History at 28 RPM 60
Figure 5.16. Torque Time History at 34 RPM 61
Figure 5.17. System Power Time History at 34 RPM 61
Figure 5.18. Torque Time History at 38 RPM 62
Figure 5.19. System Power Time History at 38 RPM 62
Figure 5.20. Stress Amplitude Spectra for an Upper Root, Trailing Edge Gauge at 28 RPM 64
Figure 5.21. Stress Amplitude Spectra for an Upper Root, Flatwise Gauge at 28 RPM 64
Figure 5.22. Stress Amplitude Spectra for an Upper Root, Trailing Edge Gauge at 34 RPM 65
Figure 5.23. Stress Amplitude Spectra for an Upper Root, Flatwise Gauge at 34 RPM 65
Figure 5.24. Stress Amplitude Spectra for an Upper Root, Trailing Edge Gauge at 38 RPM 66
Figure 5.25. Stress Amplitude Spectra for an Upper Root, Flatwise Gauge at 38 RPM 66

List of Appendices

Appendix A. RMV Stresses at 28 RPM 70

Appendix B. RMV Stresses at 34 RPM 85

Appendix C RMV Stresses at 38 RPM 100

1.0 INTRODUCTION

The 34-meter Test Bed is a research-oriented vertical-axis wind turbine (VAWT) located at the USDA Agricultural Research Service facility in Bushland, Texas. Sandia National Laboratories designed and built this machine to perform research in structural dynamics, aerodynamics, fatigue, and controls. Testing of the Test Bed to determine its performance in various wind conditions and at different rotation rates has been ongoing since before the official dedication on May 10, 1988. This report contains a broad range of Test Bed data collected over the past four years and serves as a reference document for aerodynamic and structural performance data.

The Test Bed is pictured in Fig. 1.1. The rotor is 34 meters in diameter with a swept area of 955 m^2 and a height-to-diameter ratio of 1.25. This variable-speed machine has an operating range of 28 to 38 rpm, and the rated power is 500 kW at a rotation rate of 37.5 rpm in mean winds of 12.5 m/s (28 mph). Table I summarizes the Test Bed specifications.

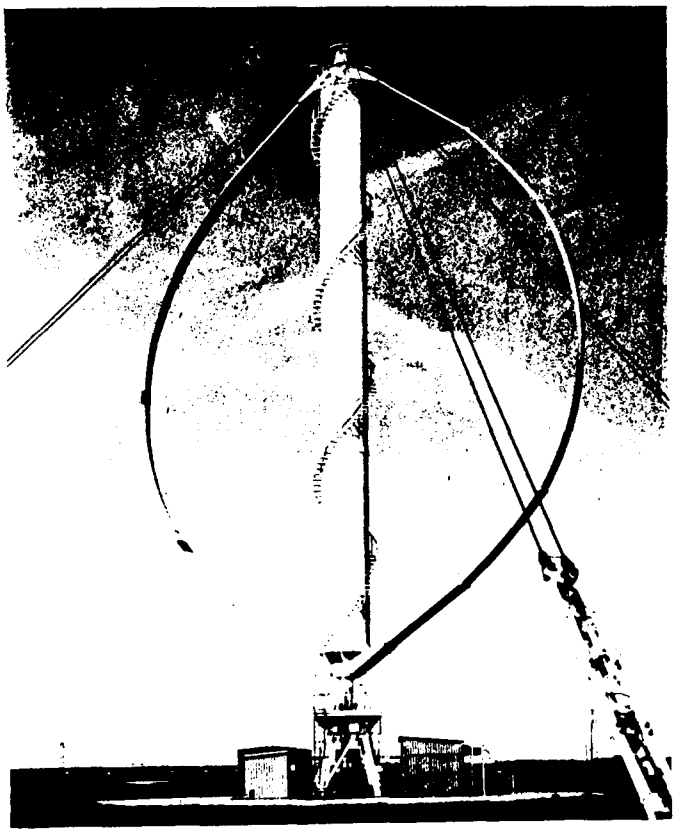

Figure 1.1. 34-m Test Bed

Compared to previously constructed VAWTs, the Test Bed blades are unique in that they are tailored both structurally and aerodynamically to minimize stresses and maximize energy capture. The root sections are straight and consist of 1.22 m (48 in.) chord, NACA 0021 profiles. The equatorial sections are

Table I. Test Bed Specifications

ROTOR

Diameter	34 m
Height	50 m
Ground Clearance	7 m
Speed	28 to 38 RPM
Number of Blades	2
Blade Material	6065-T6 Extruded Aluminum
Blade Length	54.5 m
Aerodynamic Control	Stall Regulation
Airfoils	SNL 0018/50 NACA 0021
Chord Dimensions,m	0.91,1.07,1.22
Swept Area	955 m^2
Solidity	0.13
Central Column	
Material	Aluminum
Diameter	3 m
Wall Thickness	12.5mm
Guy Cables	
Number	3 Sets of 2
Tension	750-830 kN/Set
Material	Steel Bridge Strand
Diameter	64 mm

GEARBOX

Type	Three-Stage Parallel
Step-up Ratio	47.5 : 1
Rating	709 kW

GENERATOR

Type	Variable Speed Synchronous AC
Rating	625 kVA
Voltage	1200
Speed	280 to 1900 RPM
Frequency	60 Hz

CONTROLS

System-
Programmable Industrial Controller
Generator Speed and Torque-
Load Commutated Inverter

PERFORMANCE

Rated Power	500 kWe
RPM at Rated	37.5
Wind Speed at Equator, m/s	
Rated	12.5
Cut-out	20
Survival	67

DATA ACQUISITION AND ANALYSIS

Number of Channels	128
Maximum Data Throughput Rate	200 kHz

curved, 0.91 m (36 in.) chord, SNL 0018/50 profiles, and the transition sections are curved, 1.07 m (42 in.) chord, SNL 0018/50 profiles. The schematic of Fig. 1.2 details the blade shape geometry including the spanwise lengths of each blade section. The SNL 0018/50 profiles are part of a series of natural laminar flow airfoils developed at Sandia specifically for use on VAWTs (Klimas 1984). The turbine and its environment are heavily instrumented to measure blade strains at many locations, wind speed and direction, temperature, rotor torque, electrical power output and rotational speed.

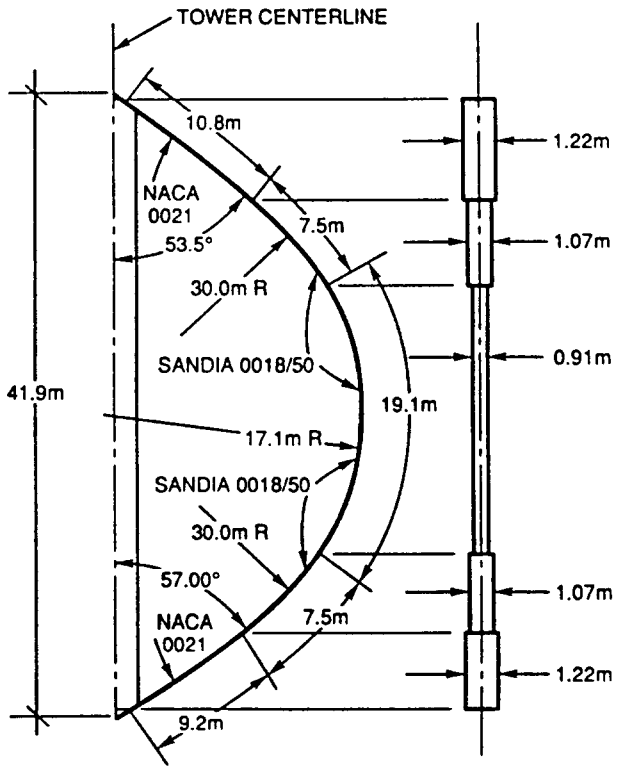

Figure 1.2. Blade Shape Geometry

1.1 Scope

This report begins with a brief description of the test program for the 34-meter Test Bed (Section 1.2). Section 2.0 provides details of the instrumentation system (both rotor-based and ground-based) and the data acquisition and analysis system (DAAS).

Turbine test data are discussed in Sections 3.0, 4.0, and 5.0. Section 3.0 emphasizes aerodynamic performance data, which includes tare and drag measurements, rotor torque data at the three primary rotation rates, and C_p and K_p curves. In addition, measured rotor power is compared to analytical calculations, and the effects of joint fairings and bug contamination on performance are shown. Section 4.0 contains structural performance data composed of centrifugal- and gravity-induced blade responses, operating stresses at the three primary rotation rates, and measured natural frequencies. Included are comparisons between measured data and analytical calculations. Section 5.0

shows selected time histories during normal turbine operation, start-up and braking, and examples of blade stress amplitude spectra at three rotation rates. Appendices A, B, and C contain complete sets of RMV stresses at three rotation rates.

1.2 Turbine Testing

The turbine testing program began with a series of assembly and start-up tests [Phase I of the 34-Meter Test Plan, Stephenson (1986)]. These tests were performed during and immediately after construction to make fundamental measurements not easily repeated after the machine was operational. The major tests performed in Phase I are described below:

1) Testing and calibration of instrumentation and equipment during installation and validation of the data collection system.

2) Weighing of rotor components.

3) Testing of the variable-speed generator by the manufacturer, General Electric.

4) Checkouts of the Allen Bradley controller to determine the enable/interrupt functions.

5) Determination of the power required to start the turbine with no blades and turn the turbine with and without blades (tare and zero-wind drag tests).

6) Modal vibration tests on the stationary rotor and individual components including blades, column, and guy cables.

7) Brake tests to determine the dynamic coefficient of friction of the brake pads and to insure correct operation of the entire brake system.

8) Calibration of blade strain gauges by subjecting the blades to known static loads.

9) Initial start-up tests for checkout of the entire turbine system.

In Phase II, the machine characterization phase, resonance surveys were performed to determine the location of natural frequencies at several rotation

rates and to approximate cyclic stresses at various wind speeds. Other tests provided additional controller checkouts and full aerodynamic and structural performance characterizations.

Phase III, the current stage of testing, supports the study of advanced concepts. Flow visualization tests, including tuft studies, are complete, and tests to determine the effects of bug contamination and joint fairings on performance have recently been performed. Tests to validate different variable-speed control algorithms are next on the agenda.

The measured data shown in this report are from Phase I and II testing with the exception of the results from the bug contamination and joint fairing studies.

2.0 INSTRUMENTATION

To meet current and future research needs, the turbine and its environment were equipped with a large array of sensors (see Fig. 2.1) to monitor all aspects of the machine's performance. Current instrumentation includes 57 strain signals from the blades, 13 strain signals from the tower, 8 strain signals from the brakes, 5 crack propagation signals, 25 environmental signals, 22 turbine performance signals, and 29 electrical performance signals. The rotor instrumentation is described in detail in Sutherland and Stephenson (1988).

Figure 2.2 is a Test Bed site plan. It shows the two data acquisition and analysis system (DAAS) meteorological towers northeast (North tower) and southwest (South tower) of the turbine. Each DAAS tower has two anemometers, which measure wind speed and direction at the equator height of 28.2 m (92.5 ft). Wind information from the anemometer tower upwind of the turbine is used by the DAAS software in the data collection process. The location of the guy cables and associated tie-downs are also indicated in Fig. 2.2. A third meteorological tower, southeast of the south tower (not shown in Fig. 2.2), has five anemometers at heights of 10, 20, 30, 40, and 48 meters. These anemometers supply wind information to a data logger, which records long-term wind speeds and directions (Ralph 1990). The 30-meter anemometer also provides wind information to the turbine controller.

2.1 Ground-Based Instrumentation

The ground-based instrumentation includes sensors that measure wind speed and direction, environmental conditions (temperature and barometric pressure), rotor and generator rpm, rotor torque, generator current and voltage, blade position, guy cable tension, transmission and generator bearing vibration, and brake paddle strains. Analog signals from these sensors are transmitted through ground cables to an instrumentation room adjacent to the turbine pad and then to an analog-to-digital (A/D) convertor located in the control building, which is over 122 m (400 ft) west of the turbine base (See Fig. 2.2).

2.2 Rotor-Based Instrumentation

The rotor-based instrumentation consists primarily of blade and column strain gauges. These analog signals travel through cables located inside the blades, down the outside of the column, and to the pulse code modulation (PCM) system, which resides in the base of the column. The PCM converts the signals into a

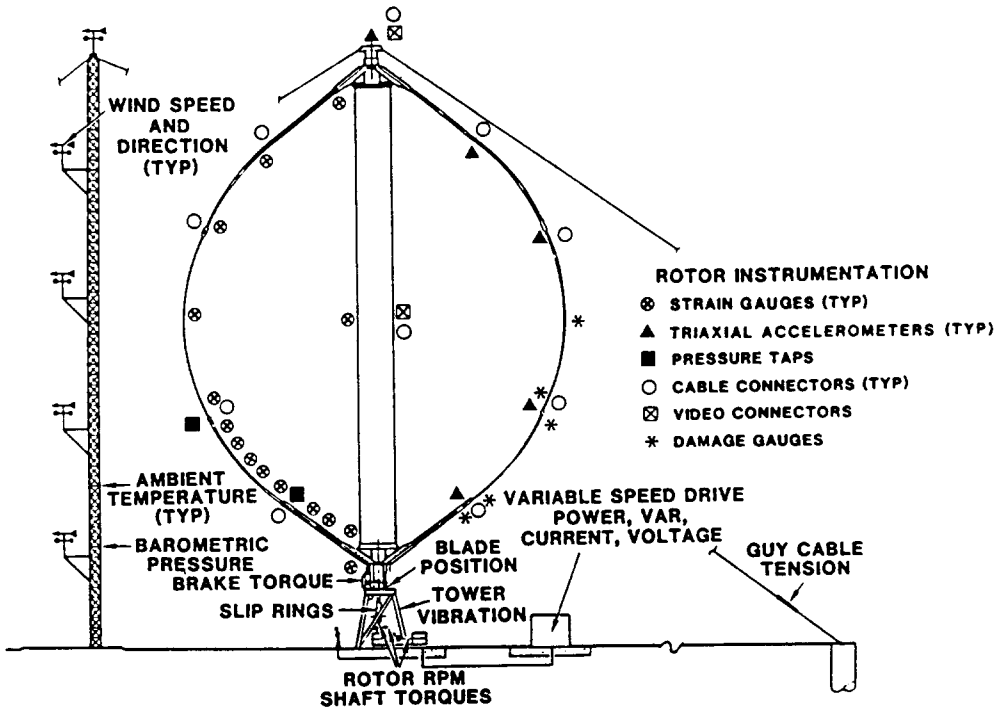

Figure 2.1. Test Bed Instrumentation

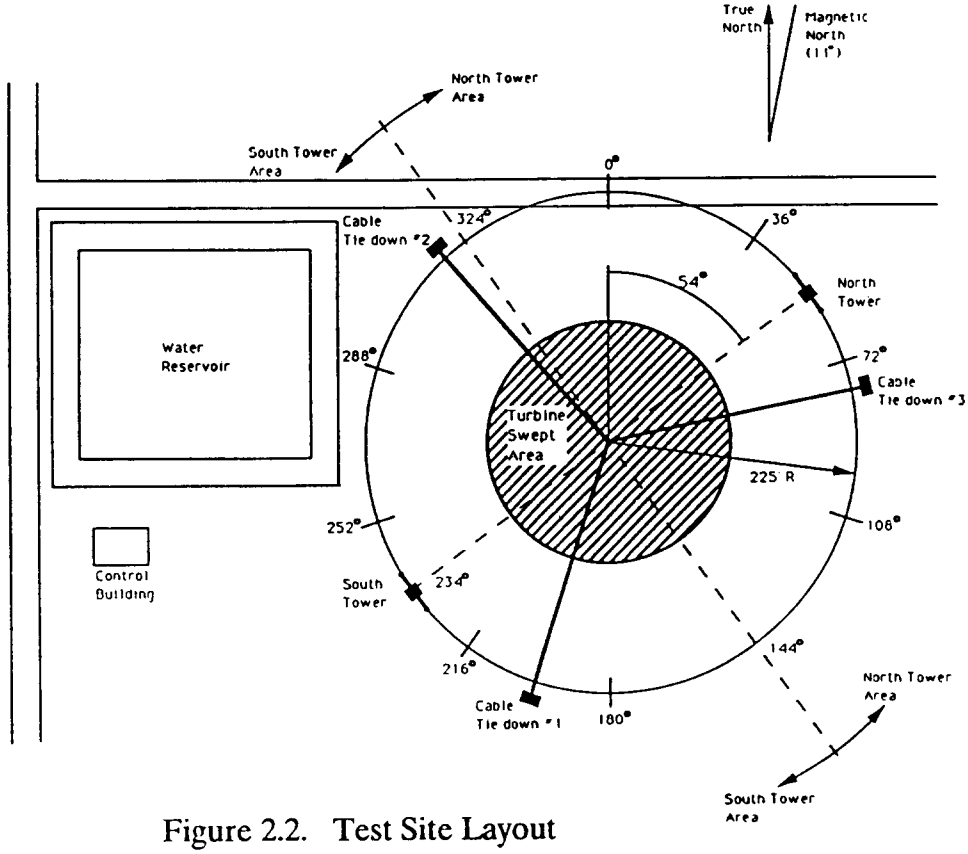

Figure 2.2. Test Site Layout

high-speed serial stream, which is passed through slip rings to the instrumentation room. From there the signals travel to the control building where they are decommutated, sent to a D/A convertor, synchronized with the ground-based signals, and reconverted by an A/D convertor. Pressure taps, cable connectors, and video connectors are available on the column or blades for future testing hookups.

2.3 Data Acquisition and Analysis System

Figure 2.3 shows a schematic of the data collection system. The signals from both the ground-based and rotor-based instrumentation arrive at the data acquisition and analysis (DAAS) processor, a Hewlett Packard (HP) 1000 minicomputer, from the A/D convertor. Some of the signals are also routed to the data logger, a separate HP 1000 minicomputer, through a smaller A/D convertor.

Data are collected in the form of time histories. With the use of our data acquisition and analysis system (Berg et al. 1988), data can be processed in any of several ways. The data can simply be plotted as a function of time (time histories) or data segments can be averaged to obtain values of mean and root mean variance. Also, frequency analyses may be performed by executing spectral and cross-spectral programs.

Much of the data is processed with the BINS program, which uses the Method of Bins (Akins 1978) to reduce data for field performance evaluation. In this methodology the range of anticipated wind speed readings is partitioned into equal intervals or wind bins, which are 0.5 m/s wide. Measurements of turbine output (torque, strain, vibration, etc.) and a reference anemometer are sampled, usually at 20 Hz. The mean, standard deviation and variance are calculated for every data channel each rotation to create a bin entry for each of these three parameters. [For example, at 34 rpm one revolution occurs every 1.764 seconds. Approximately 35 samples, then, occur in a revolution (1.764 seconds X 20 samples per second) and are averaged to determine a bin entry for the mean.] The average wind speed for that rotation identifies the proper wind bin. The bin entries for the mean, standard deviation, and variance are added to the appropriate running totals in each wind bin for each channel and then stored. The stored record, which consists of a wind speed distribution and the corresponding summations, may be combined with other records to provide quantitative measures of performance. For a complete data set it is desirable to obtain over 1000 revolutions or bin entries for each wind bin, although this is usually difficult at the high and low end of the wind spectrum.

All sensors are zeroed at prescribed intervals to eliminate drifting. Because the low-speed torque sensor is the instrument that determines aerodynamic

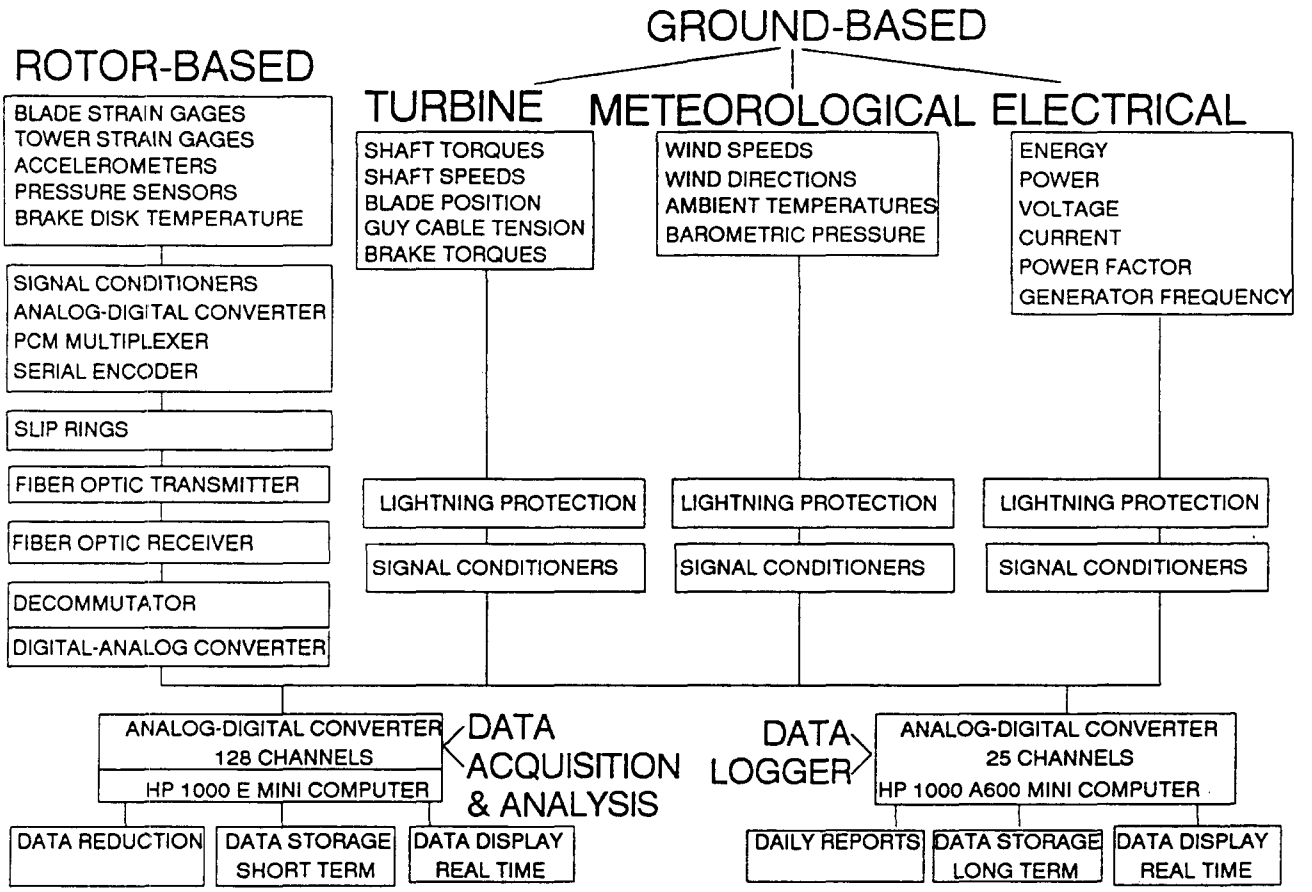

Figure 2.3. Data Acquisition System

performance, its zeroing occurs more often--both before and during the collection of a data set.

Table II lists the measurement channels available on the DAAS. Included are the channel numbers, the measurement code, and the measurement type with associated units. For the strain gauges the measurement code contains information that indicates the gauge location on the rotor and the type of strain measurement. This strain gauge location code is further described in the structural performance section (Section 4.0). Sutherland and Stephenson (1988) describe the details of the strain gauge circuits.

Table II. Measurement Channels

Channel Number	Code	Measurement Type (Units)
1 - 30	(see Section 4.4)	Strain Gauges (MPa)
31	WSNE	Wind Speed North East (m/s)
32	WSNW	Wind Speed North West (m/s)
33	WSSE	Wind Speed South East (m/s)
34	WSSW	Wind Speed South West (m/s)
35	WDN	Wind Direction North Tower
36	WDS	Wind Direction South Tower
37	KPA	Barometric Pressure (kPa)
38	C 10	Temperature @ 10m height (deg C)
39	C 48	Temperature @ 48m height (deg C)
40	RPMO	Low Speed Shaft RPM (optical)
41	KNML	Low Speed Shaft Torque (kNm)
42	KWG	Generator Power (kW)
43	KWSY	System Power (kW)
44	PFSY	System Power Factor
45	AG	Generator Current (A)
46	KVG	Generator Volts (kV)
47	ASY	System Current (A)
48	KVSY	System Voltage (kV)
49	KWAE	Auxiliary Equipment Power (kW)
50	ACMC	AC Voltage Motor Control Center
51	KN#1	Tension in Guy Cable #1 (kN)
52	KN#2	Tension in Guy Cable #2 (kN)
53	KN#3	Tension in Guy Cable #3 (kN)

Table II. (continued)

54	GENR	Generator Radial Vibration (in/s)
55	TRNR	Transmission Radial Vibration(in/s)
56	TRNA	Transmission Axial Vibration (in/s)
57	UBRG	Upper Bearing Vibration (in/s)
58	LBRG	Lower Bearing Vibration (in/s)
59	RPMG	Generator Shaft RPM
61	BRKS	South Brake Strain Gauge (MPa)
62	BRKN	North Brake Strain Gauge (MPa)
63	BRKE	East Brake Strain Gauge (MPa)
64	BRKW	West Brake Strain Gauge (MPa)
65	RPML	Low Speed Shaft RPM (Lebow)
66	NMHS	High Speed Shaft Torque (Nm)
67	HRPM	RPM High Speed Shaft (Lebow)
68	DEG	Blade Position
69	PLC2	Comm Line to Remote Controller
70	RRPM	Rotor RPM
71	LCAC	LCI AC Voltage
72	ACCB	AC Waveform at Control Bldg.
79	MS48	Wind Speed at 48m Height (m/s)
80	MS40	Wind Speed at 40m Height (m/s)
81	MS30	Wind Speed at 30m Height (m/s)
82	MS20	Wind Speed at 20m Height (m/s)
83	MS10	Wind Speed at 10m Height (m/s)
84	WD48	Wind Direction at 48m Height (deg)
85	WD40	Wind Direction at 40m Height (deg)
86	WD30	Wind Direction at 30m Height (deg)
87	WD20	Wind Direction at 20m Height (deg)
88	WD10	Wind Direction at 10m Height (deg)
125	PCM0	Zero Volt Check (PCM)
126	PCMV	Nominal 4.1 Volt Check (PCM)
127	PH0	Phoenix Zero Volt Check
128	PHV	Phoenix 8.0 Volt Check

3.0 AERODYNAMIC PERFORMANCE

3.1 Tare Loss and Zero-Wind Drag Measurements

Tare losses are those losses that occur in the rotor bearings due to friction. The torque required to turn the center column without blades is a measure of the tare loss and is known as the tare torque. The tare torque is measured by the torque sensor on the low-speed shaft. The tare and rotor torques, when added together, determine the aerodynamic torque. Several tests to determine the tare losses under different conditions were performed in Phase I testing. Tares were measured at different guy cable tension levels, temperatures, operation times, and rotation rates before the blades were installed.

Several conclusions resulted from the tare tests (Stephenson 1990): 1) The effects on tare torque of changes in machine rotation rate or guy cable tension are minimal and can be neglected. 2) The average value for tare loss in turning the rotor at any rpm was initially estimated to be 5.0 kNm, but later revised to 3.0 kNm. 3) This average tare loss varies somewhat with ambient temperature and duration of operation. At a given ambient temperature approximately 30 to 40 minutes of machine operation minimizes the tare loss.

After blade installation, a value for zero-wind drag plus tare loss at 10 rpm was measured to be about 5.0 kNm - the same value as that measured for the tare loss only. An analytical calculation determined a likely value for zero-wind drag to be 2.0 kNm; this results in a more likely value of 3.0 kNm for the tare loss. This value, 3.0 kNm, is used in the binsing process to adjust the low speed torque to aerodynamic torque. The drop in tare torque from 5.0 kNm was probably due to a loosening of the bearing seals with additional operation. (The zero-wind-plus-tare torques at 28, 34, and 38 rpm are 12.3, 16.2 and 20.7 kNm, respectively - Section 3.3.)

These levels of torque measurement (2-5 kNm), however, are close to being in the noise for the size of torque sensor in use. The Test Bed torque sensor, a Lebow Model 1121, has a maximum range of 339 kNm; the measured value of tare plus drag is only 1 to 1.5 % of this range. For such small measurements a smaller torque sensor would be more appropriate, but would be undersized for the maximum operating torque.

3.2 Transmission (Gearbox) and Generator Losses

In the original construction a high-speed torque sensor was located between the transmission and generator on the high-speed shaft. Its use would facilitate the measurement of losses in the transmission and generator. Due to high vibrations, however, the high-speed torque sensor was damaged and became inoperable. Taking the difference between measurements of system power and low-speed torque gives a value for the combined transmission and generator losses; however, calibration of the system power transducer was not obtained. Estimates of these losses are provided in the remainder of this subsection.

The Test Bed gearbox, a Brad Foote Model 3RV-2250-S, is a triple reduction unit (47.1 gear ratio) with a right-angle spiral bevel-gear on the last stage. With a service factor of 1.0 it has a rating of 902 hp (673 kW) at 1750 rpm (37.1 rpm low-speed shaft), 760 hp (567 kW) at 1450 rpm (30.8 rpm low-speed shaft), and approximately 700 hp (522 kW) at 28 rpm on the low-speed shaft. The following information is published in the Brad Foote catalog and lists losses for different units as a percentage of full load.

Brad Foote Gearbox Losses (% of Full Load)

Single Reduction	1-1/2%
Double Reduction	3%
Triple Reduction	4-1/2%
Quadruple Reduction	6%

A right-angle gear adds 0.3-0.4 % to these losses.

For losses at less than full load, the following estimates were obtained from a different gearbox manufacturer and applied to the Test Bed gearbox.

Losses (%) For Parallel Shaft Reducers

	100% Load	75% Load	50% Load	25% Load
Triple Reduction	4.0	4.25	4.75	6.0
Test Bed Gearbox- (approximate)	4.5	4.75	5.25	6.5

Again, a right-angle gear adds 0.3-0.4% to these numbers.

Estimates of the total Test Bed transmission losses are given below.

Estimated Transmission Losses (kW)

	100% Load	75% Load	50% Load	25% Load
28 RPM	26	20	15	9
37.1 RPM	33	26	19	12

The generator is a General Electric 700-kW synchronous motor with an adjustable-speed load-commutated inverter (LCI) drive. The motor itself is 94.4% efficient at rated load. The total losses at full load including the LCI, inductor, reactor, and motor/generator and excluding the transformer are estimated below.

Estimated Generator Losses (kW)

RPM	1190	1430	1670	1790	1900
Losses (kW)	23	24	36	42	42

3.3 Performance Data

The design operating range of the turbine spans from 28 to 38 rpm. Three rotational rates - 28, 34, and 38 rpm - were chosen as major data collection points. The turbine was operated at each of these rotation rates at all wind speeds up to the cutout (20 m/s at 28 and 34 rpm and 13 m/s at 38 rpm) to collect data to fully characterize the machine structurally and aerodynamically.

For the data plots included in this report, the reference velocity is the wind velocity at the turbine equator, which is 28.2 m (92 ft) above ground level. The measurements of rotor torque and power are adjusted to sea-level air density. [The elevation at the Bushland site is 1183 m (3880 ft) above sea level.]

3.3.1 28 RPM

Figure 3.1 shows the binsed rotor torque (mean average) curve of the Test Bed at 28 rpm for winds from 0 to 21.25 m/s. The rotor torque is measured at the low-

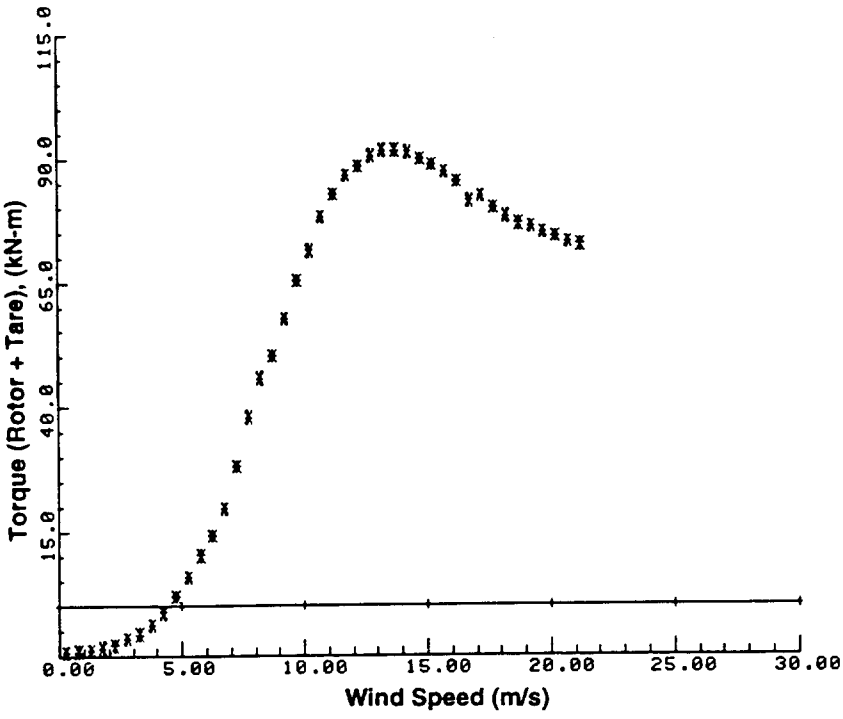

Figure 3.1. Rotor Torque vs. Wind Speed at 28 RPM

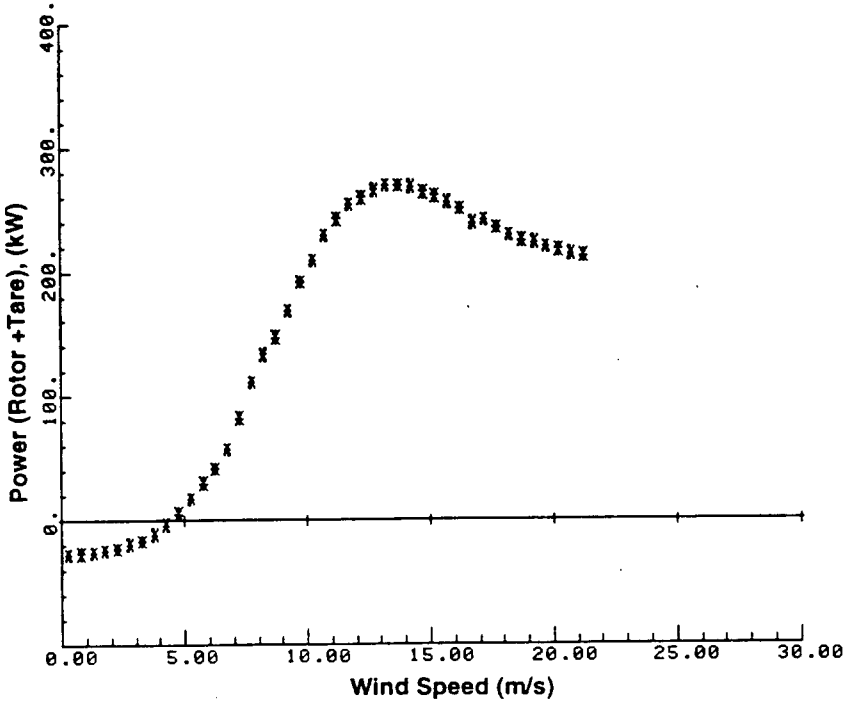

Figure 3.2. Rotor Power vs. Wind Speed at 28 RPM

speed shaft; therefore, these values have been adjusted upwards by the addition of the tare torque of 3.0 kNm (See Section 3.1). The binsed rotor power (mean average) is shown in Fig. 3.2. Both Figs. 3.1 and 3.2 clearly exhibit the desired characteristic of power regulation or power rollover in moderate to high winds. This effect is caused by the sharp stall behavior of the laminar flow airfoil sections. The peak torque of 91.5 kNm and peak power of 268 kW both occur at a 13.75 m/s wind speed. Positive rotor power first takes place at 4.5 m/s; however, positive electrical power occurs at a higher wind speed because of the transmission and generator losses.

In the Method of Bins two nondimensional quantities, C_p and K_p, are defined as indicated below (Akins 1978):

$$C_p = \frac{T(V_R)\,\omega}{1/2\,\rho\,A\,V_R^3}$$

$$K_p = \frac{T(V_R)\,\omega}{1/2\,\rho\,A\,(R\omega)^3}$$

where

$T(V_R)$ is the average torque for a particular bin

ρ is the density of ambient air during the test

A is the swept area of the turbine

V_R is the reference wind velocity for the bin corresponding to the torque, $T(V_R)$

R is the radius of the turbine

ω is the angular velocity of the turbine.

The power coefficient*, C_p, is a measure of the fraction of available power extracted from a stream-tube of air passing through the turbine cross section. The performance coefficient*, K_p, is a measure of power output and is

* The terms, power and performance coefficient, are often interchanged when describing C_p and K_p.

proportional to turbine power in a constant rpm mode of operation.

The coefficient C_p, as a function of the tip-speed ratio, Rw/V_R, is illustrated in Fig. 3.3 for the 28 rpm data set. The peak C_p is 0.409 and occurs at a wind speed of 7.75 m/s (tip-speed ratio of 6.34). The coefficient K_p, as a function of advance ratio, V_R/Rw, is shown in Fig. 3.4.

The distribution of bin entries for this 28 rpm data set is shown in Fig. 3.5. This curve was developed by dividing the number of entries in each bin by the total number of bin entries. To minimize biasing of the data, it is desirable to obtain a fairly even distribution of bin entries.

A listing of the 28 rpm data set is presented in Table III. Over 1000 bin entries reside in the wind bins from 2.75 to 13.25 m/s. In plotting Figs. 3.1 - 3.5, the minimum number of bin entries in each bin was chosen to be 100. Table III has 10 data columns, which are described below.

Column 1 is the value of wind speed at the middle of each 0.5 m/s bin.

Column 2 is the number of bin entries in each bin. Each entry is the average of the data points sampled during one revolution.

Column 3 is the % of total entries that occur in that particular bin.

Column 4 is the mean average of the rotor torque.

Column 5 is the root mean variance (square root of the average of the variances for that bin) of the rotor torque.

Column 6 is the tip speed ratio.

Column 7 lists C_p values.

Column 8 lists K_p values.

Column 9 is the rotor power in kW.

A standard heading is printed at the beginning of Table III. The first line of the heading provides a title of the data collected. For example, in Table III the title is B280290: BU-34. BU-34 refers to the current turbine configuration, and

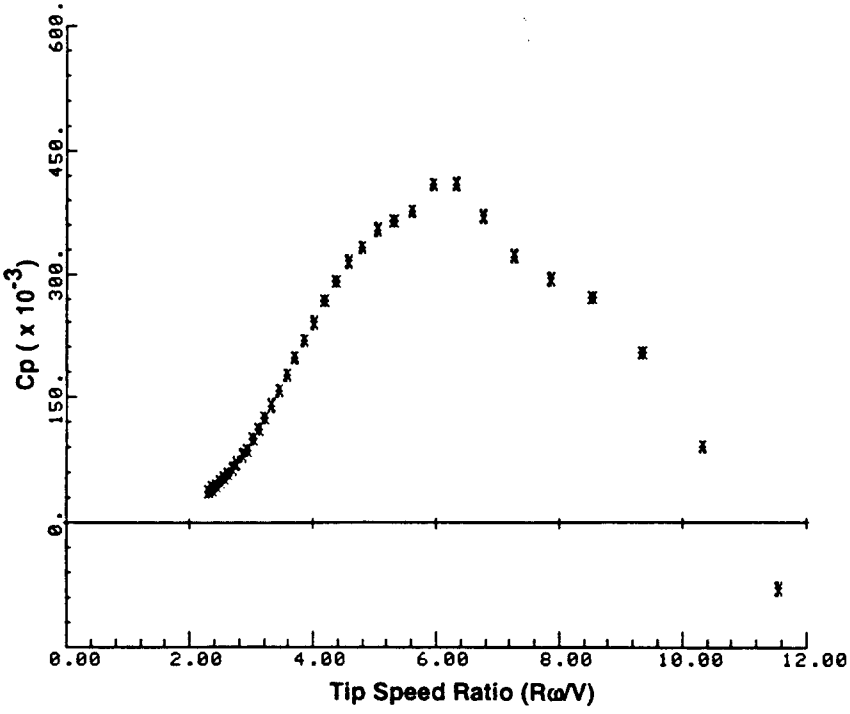

Figure 3.3. C_p vs. Tip Speed Ratio at 28 RPM

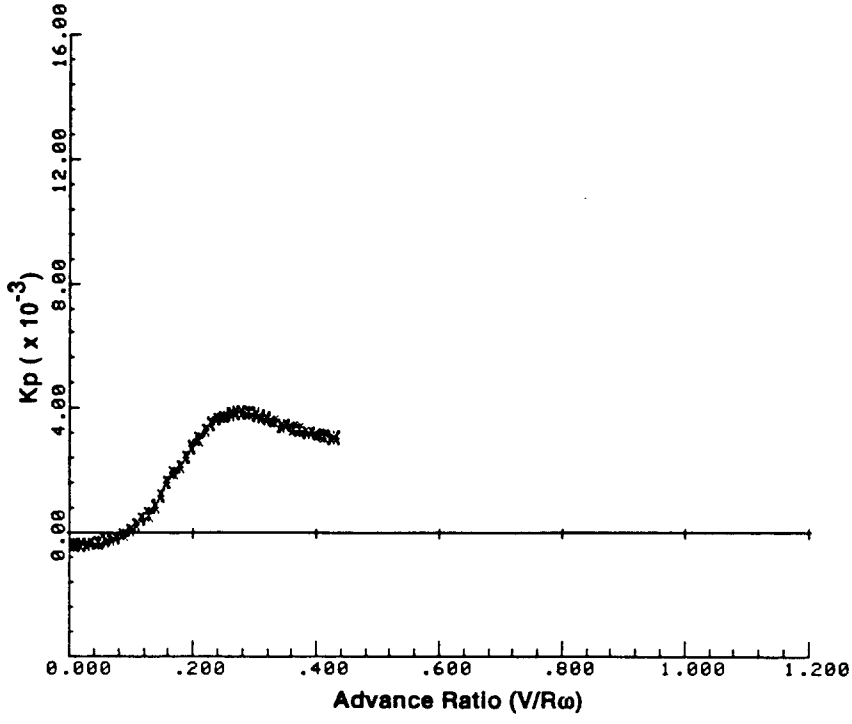

Figure 3.4. K_p vs. Advance Ratio at 28 RPM

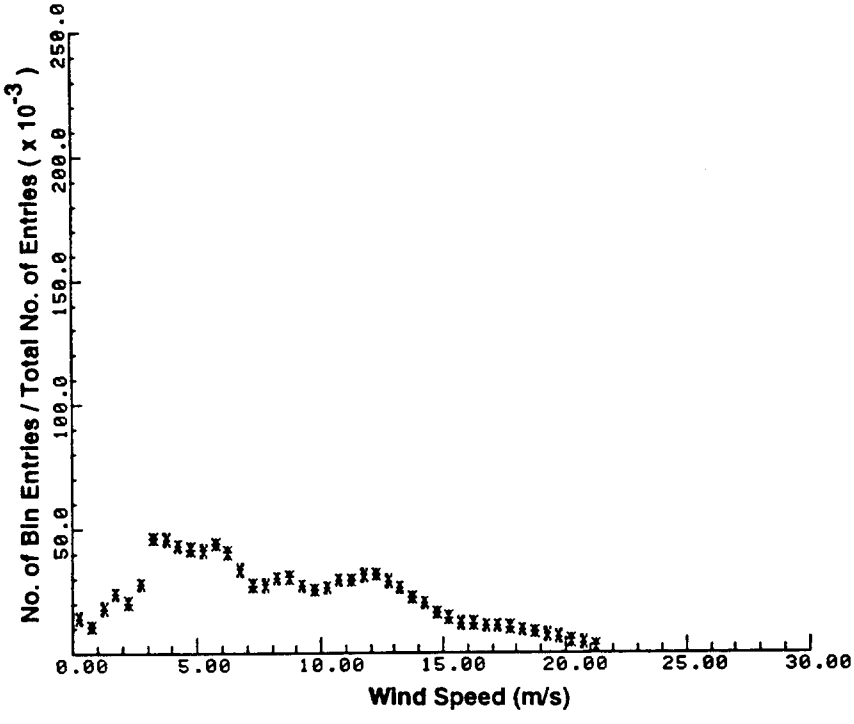

Figure 3.5. Bin Entry Distribution at 28 RPM

Table III. Performance Data - 28 RPM

B280290: BU-34 Turbine at 28.0 RPM, Total # pts = 43725.
Sample rate = 20.000 HZ, Samples/pt = 43, min pts/bin = 1.
Air Density = 1.226 Kg/m**3(CH 41 Corrected)
CH 41 Tare Torque = .3000E+04 (Nm)
Series # Records:

1	1 2 3 4 5 6 7 8 9 10 11 12 13 14 15 16
2	1 2 3 4 5 6 7 8 9 10 11 12 13 14 15 16
3	1 2 3 4 5 6 7 8 9 10 11 12 13 14 15 16
4	1 2 3 4 5 6 7 8 9 10 11 12 13 14 15 16
5	1

CHAN # 41 (KNML) + TARE [Nm]

M/S	#PTS	PROB	MAV	RMV	RW/V	CP	KP	KW
.25	623	.0142	-.927E+04	.111E+04	196.45	-2969.551	-.00039	-27.17
.75	473	.0108	-.904E+04	.121E+04	65.48	-107.289	-.00038	-26.50
1.25	791	.0181	-.892E+04	.123E+04	39.29	-22.862	-.00038	-26.14
1.75	1042	.0238	-.833E+04	.135E+04	28.06	-7.785	-.00035	-24.43
2.25	892	.0204	-.778E+04	.157E+04	21.83	-3.422	-.00033	-22.82
2.75	1220	.0279	-.650E+04	.190E+04	17.86	-1.565	-.00027	-19.06
3.25	2026	.0463	-.555E+04	.220E+04	15.11	-.810	-.00023	-16.27
3.75	2007	.0459	-.386E+04	.242E+04	13.10	-.367	-.00016	-11.32
4.25	1889	.0432	-.121E+04	.263E+04	11.56	-.079	-.00005	-3.54
4.75	1834	.0419	.194E+04	.281E+04	10.34	.091	.00008	5.69
5.25	1812	.0414	.590E+04	.370E+04	9.35	.204	.00025	17.30
5.75	1926	.0440	.103E+05	.486E+04	8.54	.271	.00043	30.15
6.25	1780	.0407	.143E+05	.590E+04	7.86	.294	.00061	41.98
6.75	1477	.0338	.197E+05	.690E+04	7.28	.321	.00083	57.79
7.25	1193	.0273	.281E+05	.793E+04	6.77	.370	.00119	82.51
7.75	1206	.0276	.380E+05	.893E+04	6.34	.409	.00161	111.35
8.25	1312	.0300	.457E+05	.945E+04	5.95	.407	.00193	133.92
8.75	1340	.0306	.502E+05	.968E+04	5.61	.376	.00212	147.30
9.25	1181	.0270	.575E+05	.993E+04	5.31	.364	.00243	168.55
9.75	1121	.0256	.653E+05	.102E+05	5.04	.353	.00276	191.48
10.25	1149	.0263	.712E+05	.105E+05	4.79	.331	.00301	208.82
10.75	1279	.0293	.780E+05	.108E+05	4.57	.314	.00330	228.61
11.25	1287	.0294	.825E+05	.110E+05	4.37	.290	.00349	242.03
11.75	1375	.0314	.864E+05	.110E+05	4.18	.267	.00365	253.37
12.25	1379	.0315	.883E+05	.110E+05	4.01	.240	.00373	258.84
12.75	1260	.0288	.904E+05	.108E+05	3.85	.219	.00382	265.19
13.25	1152	.0263	.916E+05	.106E+05	3.71	.197	.00387	268.49
13.75	986	.0226	.916E+05	.103E+05	3.57	.176	.00387	268.51
14.25	875	.0200	.913E+05	.988E+04	3.45	.158	.00386	267.77
14.75	717	.0164	.899E+05	.946E+04	3.33	.140	.00380	263.45
15.25	619	.0142	.888E+05	.909E+04	3.22	.125	.00375	260.33
15.75	518	.0118	.871E+05	.855E+04	3.12	.112	.00368	255.48
16.25	518	.0118	.853E+05	.813E+04	3.02	.100	.00361	250.20
16.75	483	.0110	.813E+05	.758E+04	2.93	.087	.00344	238.37
17.25	472	.0108	.822E+05	.757E+04	2.85	.080	.00347	240.88
17.75	455	.0104	.800E+05	.722E+04	2.77	.072	.00338	234.45
18.25	410	.0094	.781E+05	.717E+04	2.69	.064	.00330	228.98
18.75	371	.0085	.766E+05	.696E+04	2.62	.058	.00324	224.63
19.25	325	.0074	.761E+05	.695E+04	2.55	.053	.00322	223.08
19.75	281	.0064	.748E+05	.696E+04	2.49	.049	.00316	219.24
20.25	226	.0052	.742E+05	.690E+04	2.43	.045	.00313	217.44
20.75	183	.0042	.729E+05	.700E+04	2.37	.041	.00308	213.75
21.25	121	.0028	.724E+05	.695E+04	2.31	.038	.00306	212.37
21.75	70	.0016	.710E+05	.693E+04	2.26	.035	.00300	208.30
22.25	37	.0008	.712E+05	.732E+04	2.21	.032	.00301	208.79
22.75	11	.0003	.685E+05	.765E+04	2.16	.029	.00289	200.79
23.25	9	.0002	.715E+05	.681E+04	2.11	.028	.00302	209.61
23.75	6	.0001	.683E+05	.734E+04	2.07	.026	.00289	200.14
24.25	5	.0001	.701E+05	.874E+04	2.03	.025	.00296	205.47
24.75	1	.0000	.698E+05	.845E+04	1.98	.023	.00295	204.68

B280290 signifies a 28 rpm data set that was collected starting in February 1990. The total number of bin entries is 43,725. The sample rate, samples per entry, air density to which the data are corrected, and tare torque are all part of the header information. Finally, a list of the user-chosen bins records is provided, and in this case, we have chosen all available records, which consist of four series with 16 records each and one series with one record.

3.3.2 34 RPM and 38 RPM

A set of performance plots is included in this subsection for both the 34 rpm data set (Figs. 3.6 to 3.10 and Table IV) and the 38 rpm data set (Figs. 3.11 to 3.15 and Table V).

The 34 rpm torque and power curves show the rollover due to stall regulation that occurs in the higher winds (Figs. 3.6 and 3.7). Peak power is 484 kW at 17.25 m/s (Fig. 3.7), and positive rotor power is first produced at 5.5 m/s. Peak C_p is 0.401 and occurs at a tip speed ratio of 6.12 or a 9.75 m/s wind speed (Fig. 3.8). The K_p curve is shown in Fig. 3.9 and the distribution of bin entries in Fig. 3.10. Over 1000 bin entries were gathered in wind bins from 1.25 m/s to 16.25 m/s (Table IV).

The turbine is not operated at 38 rpm in winds with sufficient velocity to observe stall regulation. Design constraints limit turbine operation to 13 m/s at 38 rpm; the drive train, including the generator, was designed for a maximum sustained power production of 500 kW. With overload factors the generator system can safely produce as much as 625 kW, however, above 625 kW a runaway condition could occur. Stall regulation at 38 rpm would take place in the 700 - 800 kW range, well above the design limits. Figures 3.11 to 3.15 show torque, power, C_p, K_p, and bin entry distribution for the 38 rpm data set, and Table V lists the data plotted in these figures. The goal of 1000 points in each bin was achieved to wind speeds of only 9.25 m/s.

Table VI summarizes the rotor power data for several wind speeds (in 2.5 m/s increments) at the three rotation rates. Included for each rpm are the peak C_p, peak power, and the wind speed at which positive rotor power is first achieved. As expected, the amount of power required to turn the turbine in zero winds increases with rpm. The maximum C_p achieved is 0.409 occurring at 28 rpm in winds of 7.75 m/s.

The measured powers at the three preselected rotation rates are very consistent with predicted values (Berg et al. 1990). Figures 3.16 and 3.17 are reproduced from that report and compare the measured rotor (shaft) powers at 28 and 34 rpm to predictions developed with SLICEIT, a momentum-based, double

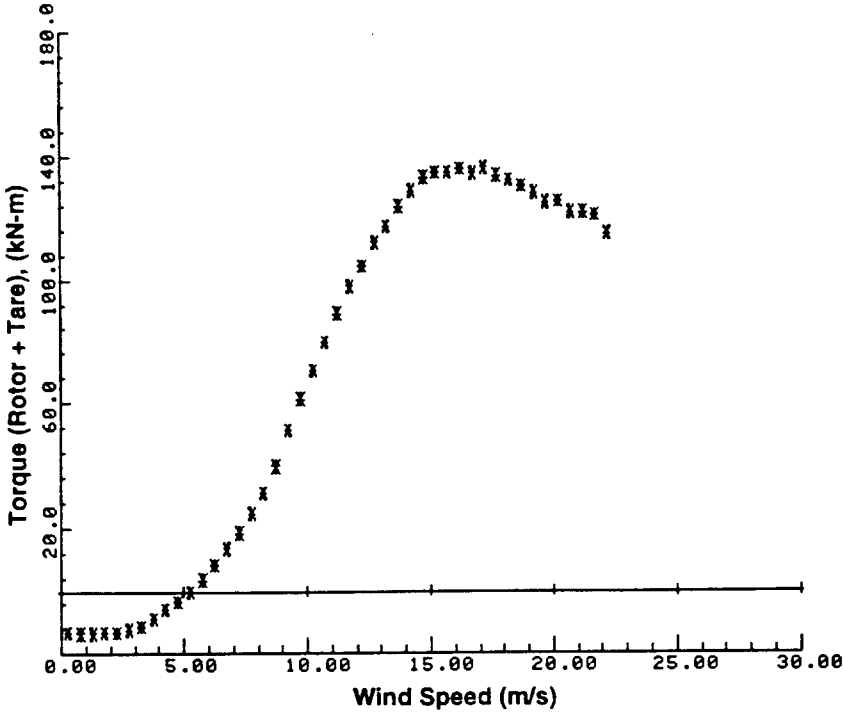

Figure 3.6. Rotor Torque vs. Wind Speed at 34 RPM

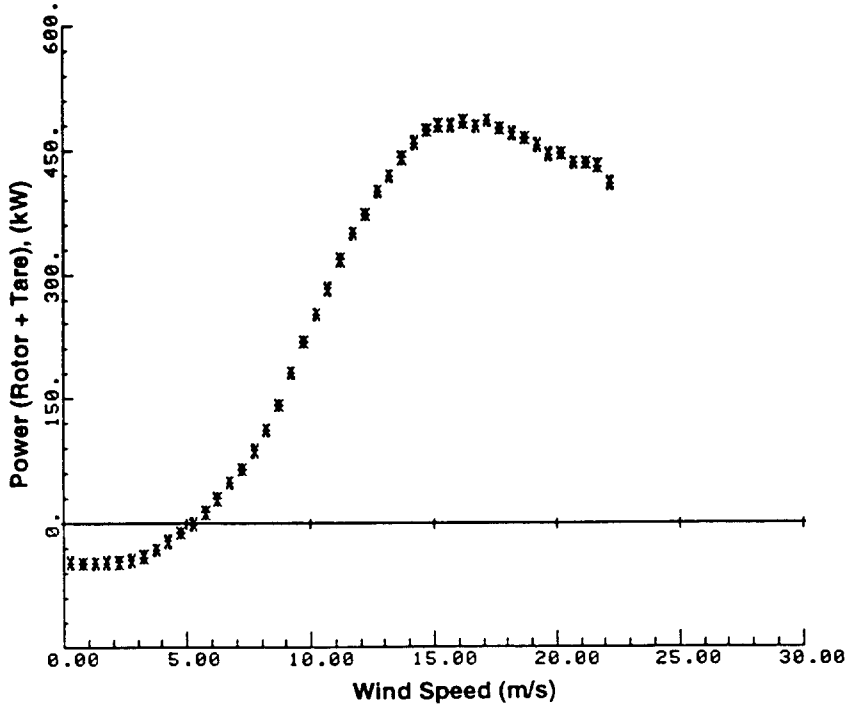

Figure 3.7. Rotor Power vs. Wind Speed at 34 RPM

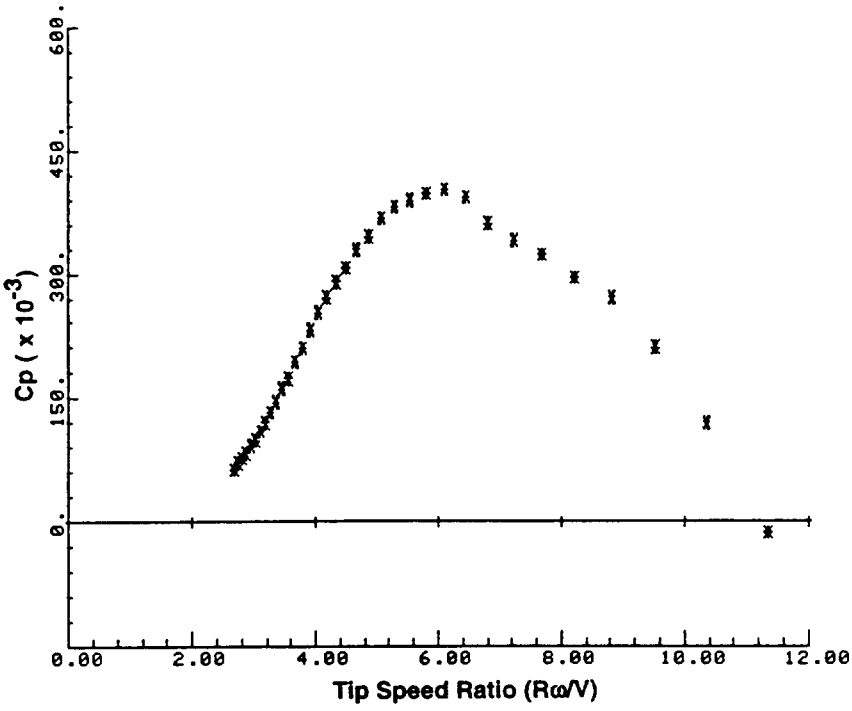

Figure 3.8. C_p vs. Tip Speed Ratio at 34 RPM

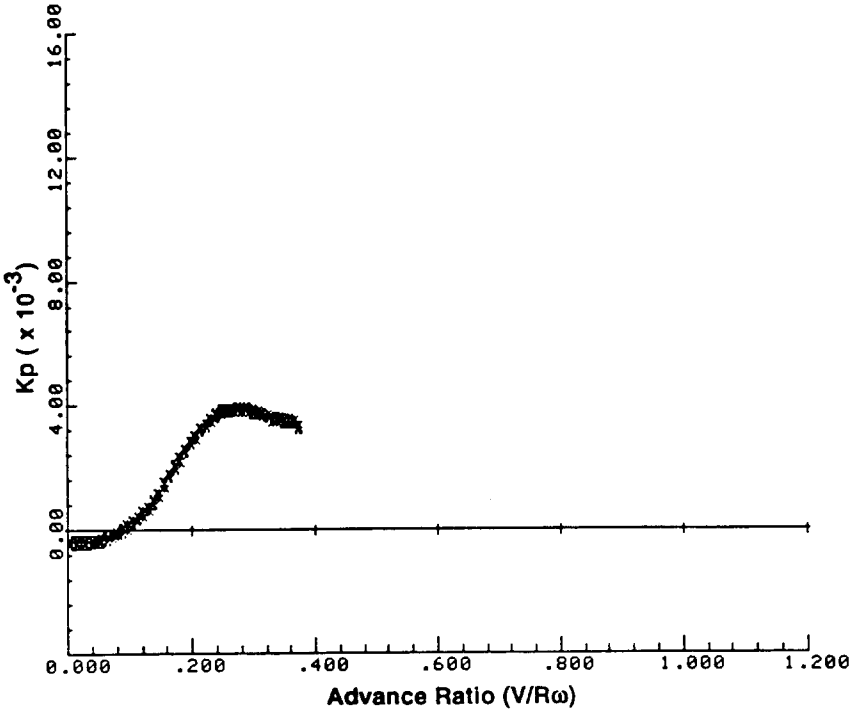

Figure 3.9. K_p vs. Advance Ratio at 34 RPM

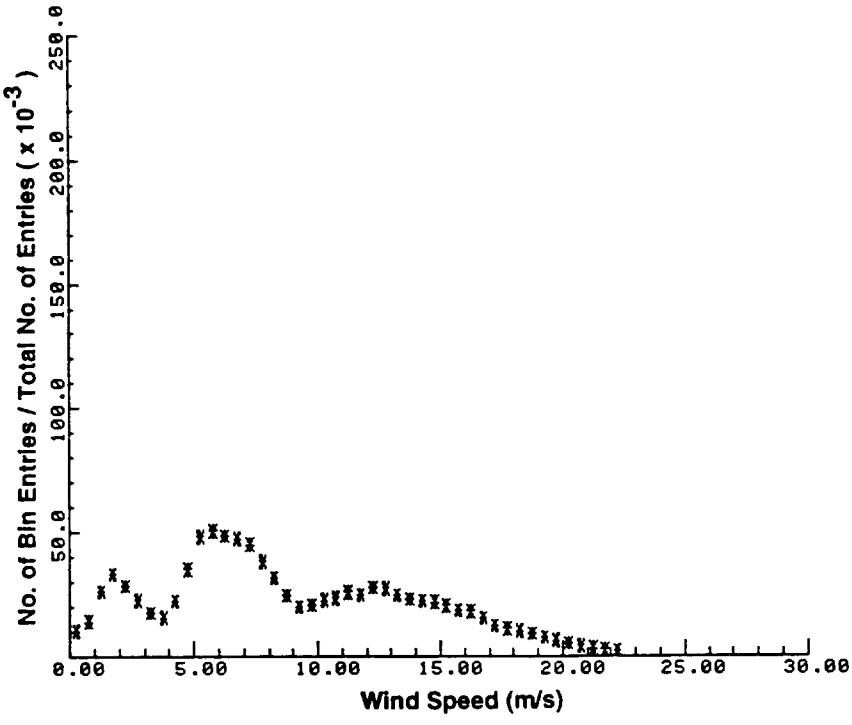

Figure 3.10. Bin Entry Distribution at 34 RPM

Table IV. Performance Data - 34 RPM

B340290: BU-34 Turbine at 34.0 RPM, Total # pts = 60890.
Sample rate = 20.000 HZ, Samples/pt = 35, min pts/bin = 1.
Air Density = 1.226 Kg/m**3(CH 41 Corrected)
CH 41 Tare Torque = .3000E+04 (Nm)
Series # Records:

1	1	2	3	4	5	6	7	8	9	10	11	12	13	14	15	16
2	1	2	3	4	5	6	7	8	9	10	11	12	13	14	15	16
3	1	2	3	4	5	6	7	8	9	10	11	12	13	14	15	16
4	1	2	3	4	5	6	7	8	9	10	11	12	13	14	15	16
5	1	2	3	4	5	6	7	8	9	10	11	12	13	14	15	16
6	1	2	3	4	5	6										

CHAN # 41 (KNML) + TARE [Nm]

M/S	#PTS	PROB	MAV	RMV	RW/V	CP	KP	KW
.25	635	.0104	-.132E+05	.102E+04	238.55	-5133.195	-.00038	-46.96
.75	867	.0142	-.133E+05	.102E+04	79.52	-192.189	-.00038	-47.47
1.25	1596	.0262	-.133E+05	.104E+04	47.71	-41.556	-.00038	-47.52
1.75	2026	.0333	-.133E+05	.110E+04	34.08	-15.077	-.00038	-47.31
2.25	1752	.0288	-.131E+05	.114E+04	26.51	-7.014	-.00038	-46.78
2.75	1396	.0229	-.124E+05	.121E+04	21.69	-3.618	-.00035	-44.06
3.25	1086	.0178	-.113E+05	.129E+04	18.35	-2.001	-.00032	-40.23
3.75	956	.0157	-.889E+04	.146E+04	15.90	-1.026	-.00025	-31.67
4.25	1365	.0224	-.592E+04	.168E+04	14.03	-.469	-.00017	-21.07
4.75	2145	.0352	-.325E+04	.186E+04	12.56	-.184	-.00009	-11.57
5.25	2941	.0483	-.329E+03	.201E+04	11.36	-.014	-.00001	-1.17
5.75	3085	.0507	.375E+04	.231E+04	10.37	.120	.00011	13.35
6.25	2962	.0486	.842E+04	.274E+04	9.54	.210	.00024	29.97
6.75	2884	.0474	.137E+05	.324E+04	8.84	.270	.00039	48.66
7.25	2741	.0450	.185E+05	.371E+04	8.23	.295	.00053	65.80
7.75	2334	.0383	.246E+05	.418E+04	7.70	.322	.00071	87.68
8.25	1931	.0317	.313E+05	.457E+04	7.23	.339	.00090	111.60
8.75	1508	.0248	.397E+05	.496E+04	6.82	.360	.00114	141.20
9.25	1231	.0202	.510E+05	.536E+04	6.45	.392	.00146	181.46
9.75	1263	.0207	.611E+05	.570E+04	6.12	.401	.00175	217.70
10.25	1386	.0228	.702E+05	.610E+04	5.82	.396	.00201	249.98
10.75	1445	.0237	.792E+05	.650E+04	5.55	.388	.00227	282.15
11.25	1583	.0260	.889E+05	.692E+04	5.30	.380	.00255	316.61
11.75	1511	.0248	.976E+05	.731E+04	5.08	.366	.00280	347.56
12.25	1703	.0280	.104E+06	.762E+04	4.87	.344	.00298	370.31
12.75	1672	.0275	.112E+06	.801E+04	4.68	.328	.00321	398.45
13.25	1500	.0246	.117E+06	.832E+04	4.50	.306	.00336	416.79
13.75	1408	.0231	.123E+06	.864E+04	4.34	.289	.00354	439.40
14.25	1371	.0225	.128E+06	.878E+04	4.19	.270	.00368	456.98
14.75	1341	.0220	.133E+06	.895E+04	4.04	.251	.00380	472.25
15.25	1253	.0206	.134E+06	.887E+04	3.91	.230	.00385	478.03
15.75	1141	.0187	.134E+06	.878E+04	3.79	.209	.00385	478.09
16.25	1114	.0183	.136E+06	.864E+04	3.67	.192	.00389	482.90
16.75	938	.0154	.134E+06	.843E+04	3.56	.173	.00384	477.28
17.25	762	.0125	.136E+06	.822E+04	3.46	.161	.00390	484.08
17.75	691	.0113	.133E+06	.804E+04	3.36	.145	.00382	474.73
18.25	629	.0103	.132E+06	.775E+04	3.27	.132	.00378	469.57
18.75	560	.0092	.130E+06	.752E+04	3.18	.120	.00373	462.87
19.25	473	.0078	.128E+06	.724E+04	3.10	.109	.00366	454.89
19.75	402	.0066	.125E+06	.699E+04	3.02	.098	.00357	443.56
20.25	330	.0054	.125E+06	.692E+04	2.95	.091	.00358	444.69
20.75	269	.0044	.122E+06	.675E+04	2.87	.083	.00349	433.04
21.25	209	.0034	.122E+06	.662E+04	2.81	.077	.00349	432.93
21.75	169	.0028	.121E+06	.642E+04	2.74	.071	.00346	429.26
22.25	134	.0022	.115E+06	.627E+04	2.68	.063	.00329	408.48
22.75	77	.0013	.116E+06	.612E+04	2.62	.060	.00332	411.73
23.25	55	.0009	.114E+06	.642E+04	2.57	.055	.00326	405.00
23.75	33	.0005	.111E+06	.660E+04	2.51	.050	.00317	394.17
24.25	10	.0002	.106E+06	.646E+04	2.46	.045	.00305	378.70
24.75	8	.0001	.103E+06	.552E+04	2.41	.041	.00297	368.34
25.25	4	.0001	.114E+06	.560E+04	2.36	.043	.00327	405.77
25.75	3	.0000	.108E+06	.609E+04	2.32	.038	.00308	383.06
26.75	2	.0000	.107E+06	.635E+04	2.23	.034	.00306	379.60

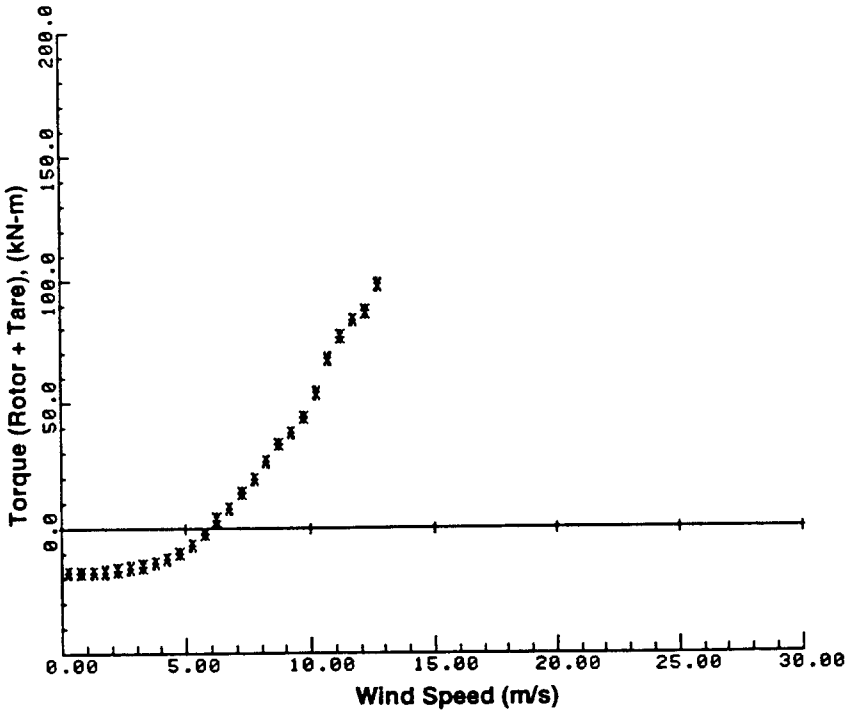

Figure 3.11. Rotor Torque vs. Wind Speed at 38 RPM

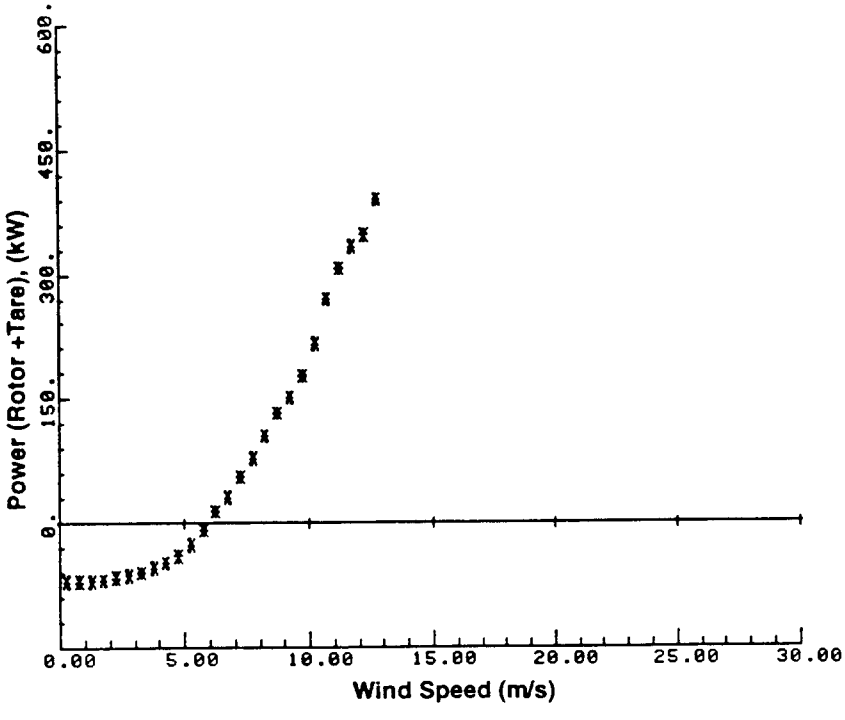

Figure 3.12. Rotor Power vs. Wind Speed at 38 RPM

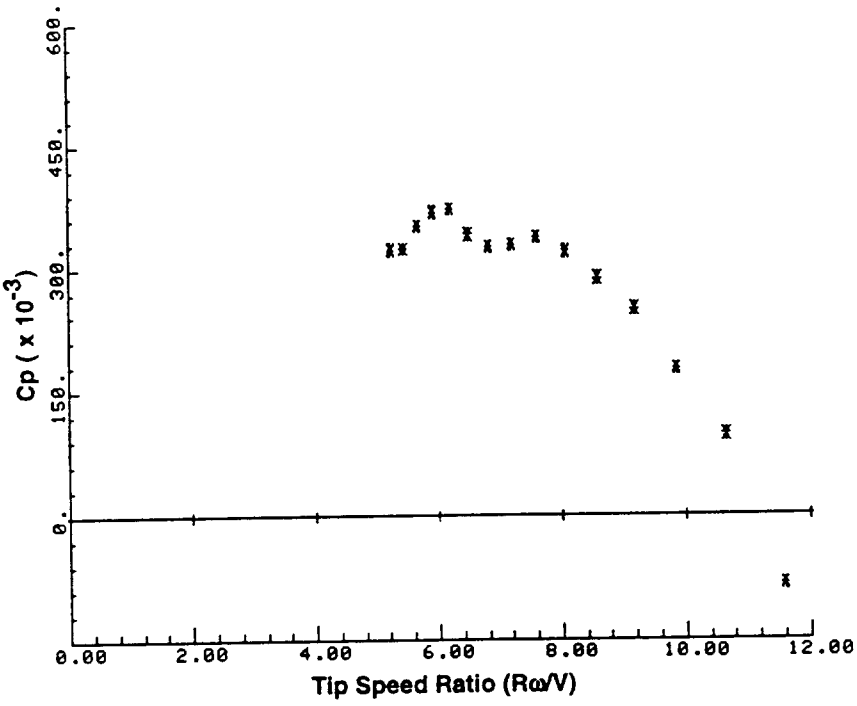

Figure 3.13. C_p vs. Tip Speed Ratio at 38 RPM

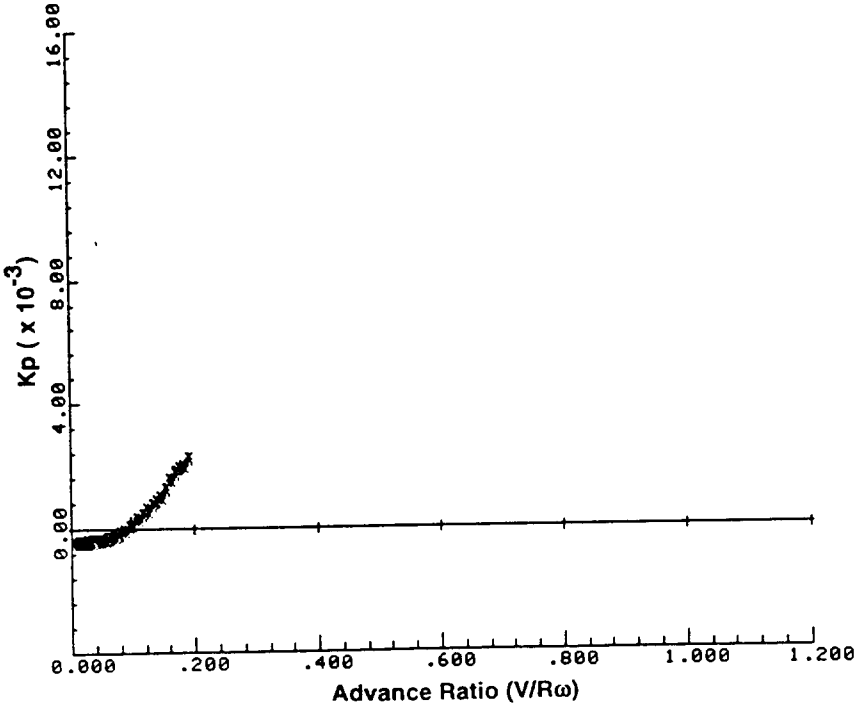

Figure 3.14. K_p vs. Advance Ratio at 38 RPM

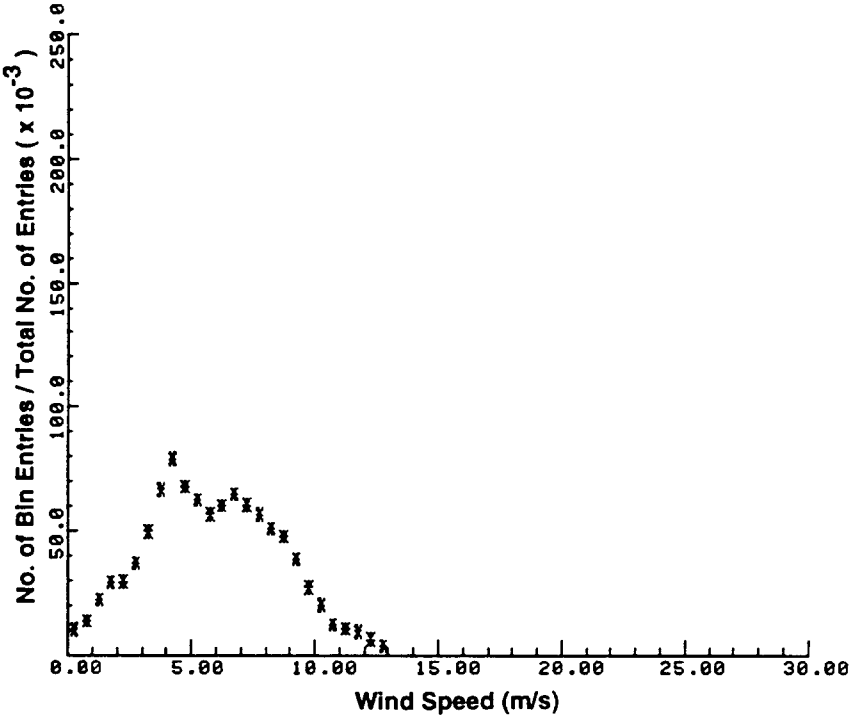

Figure 3.15. Bin Entry Distribution at 38 RPM

Table V. Performance Data - 38 RPM

B380290: BU-34 Turbine at 38.0 RPM, Total # pts = 28496.
Sample rate = 20.000 HZ, Samples/pt = 32, min pts/bin = 1.
Air Density = 1.226 Kg/m**3(CH 41 Corrected)
CH 41 Tare Torque = .3000E+04 (Nm)
Series # Records:
1 1 2 3 4 5 6 7 8 9 10 11 12 13 14 15 16
2 1 2 3 4 5 6 7 8 9 10 11 12 13 14 15

CHAN # 41 (KNML) + TARE [Nm]

M/S	#PTS	PROB	MAV	RMV	RW/V	CP	KP	KW
.25	301	.0106	-.177E+05	.121E+04	266.62	-7689.044	-.00041	-70.34
.75	394	.0138	-.177E+05	.124E+04	88.87	-284.927	-.00041	-70.38
1.25	637	.0224	-.175E+05	.125E+04	53.32	-60.994	-.00040	-69.75
1.75	839	.0294	-.172E+05	.128E+04	38.09	-21.780	-.00039	-68.34
2.25	846	.0297	-.165E+05	.135E+04	29.62	-9.869	-.00038	-65.82
2.75	1054	.0370	-.158E+05	.153E+04	24.24	-5.160	-.00036	-62.83
3.25	1424	.0500	-.150E+05	.166E+04	20.51	-2.960	-.00034	-59.50
3.75	1905	.0669	-.136E+05	.178E+04	17.77	-1.752	-.00031	-54.10
4.25	2251	.0790	-.122E+05	.181E+04	15.68	-1.076	-.00028	-48.35
4.75	1939	.0680	-.992E+04	.184E+04	14.03	-.629	-.00023	-39.46
5.25	1784	.0626	-.660E+04	.197E+04	12.70	-.310	-.00015	-26.26
5.75	1620	.0569	-.230E+04	.213E+04	11.59	-.082	-.00005	-9.15
6.25	1716	.0602	.349E+04	.241E+04	10.66	.097	.00008	13.87
6.75	1850	.0649	.798E+04	.263E+04	9.87	.176	.00018	31.77
7.25	1722	.0604	.140E+05	.298E+04	9.19	.249	.00032	55.53
7.75	1615	.0567	.196E+05	.337E+04	8.60	.286	.00045	77.96
8.25	1457	.0511	.264E+05	.371E+04	8.08	.319	.00061	104.91
8.75	1363	.0478	.332E+05	.407E+04	7.62	.337	.00076	132.01
9.25	1097	.0385	.380E+05	.427E+04	7.21	.326	.00087	151.23
9.75	783	.0275	.442E+05	.450E+04	6.84	.324	.00102	176.03
10.25	580	.0204	.538E+05	.475E+04	6.50	.340	.00124	214.22
10.75	350	.0123	.677E+05	.503E+04	6.20	.370	.00155	269.40
11.25	314	.0110	.769E+05	.531E+04	5.92	.367	.00176	305.86
11.75	278	.0098	.835E+05	.560E+04	5.67	.350	.00192	332.28
12.25	183	.0064	.871E+05	.585E+04	5.44	.322	.00200	346.52
12.75	109	.0038	.978E+05	.611E+04	5.23	.321	.00224	389.03
13.25	42	.0015	.106E+06	.638E+04	5.03	.310	.00244	422.84
13.75	30	.0011	.109E+06	.642E+04	4.85	.284	.00249	431.76
14.25	12	.0004	.968E+05	.643E+04	4.68	.227	.00222	385.07
14.75	1	.0000	.939E+05	.663E+04	4.52	.199	.00216	373.71

Table VI. Performance Data Summary

	Wind Speed	28 RPM	34 RPM	38 RPM
Power (kW)	0	-27.2	-47.0	-70.3
	2.75	-19.1	-44.1	-62.8
	5.25	17.3	-1.2	-26.3
	7.75	111.4	87.7	78.0
	10.25	208.8	250.0	214.2
	12.75	265.2	398.4	389.0
	15.25	260.3	478.0	--
	17.75	234.4	474.7	--
	20.25	217.4	444.7	--
Peak Cp		0.409 @ 7.75 m/s	0.401 @ 9.75 m/s	Insufficient Data
Peak Power (kW)		268.5 @ 13.75 m/s	484.1 @ 17.25 m/s	Exceeds 625 kW
Wind Speed at Initial Positive Power		4.5 m/s	5.3 m/s	5.9 m/s

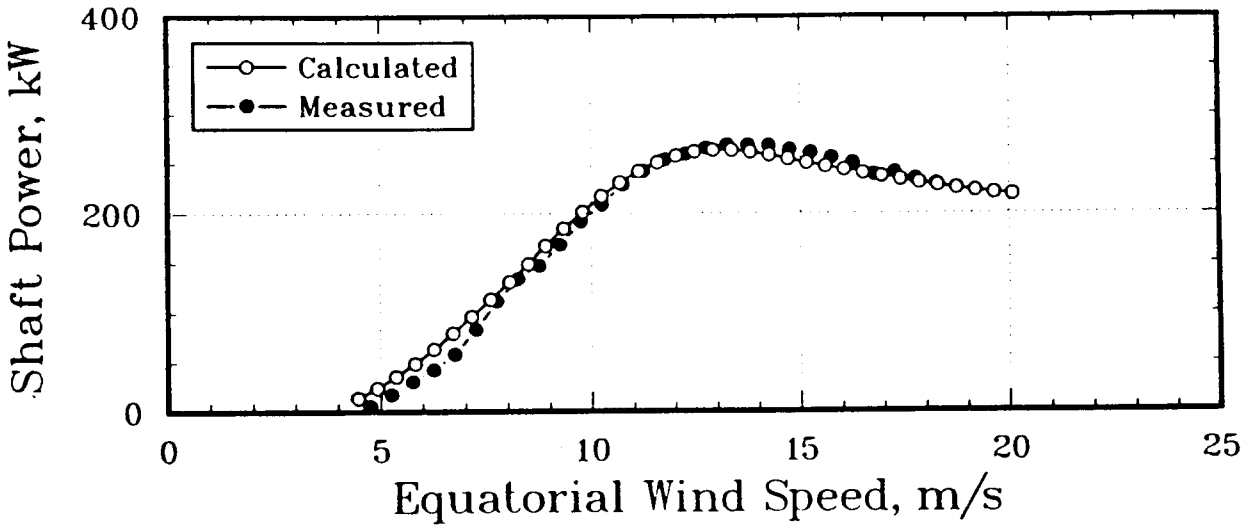

Figure 3.16. Rotor Power vs. Wind Speed at 28 RPM - Calculated and Measured

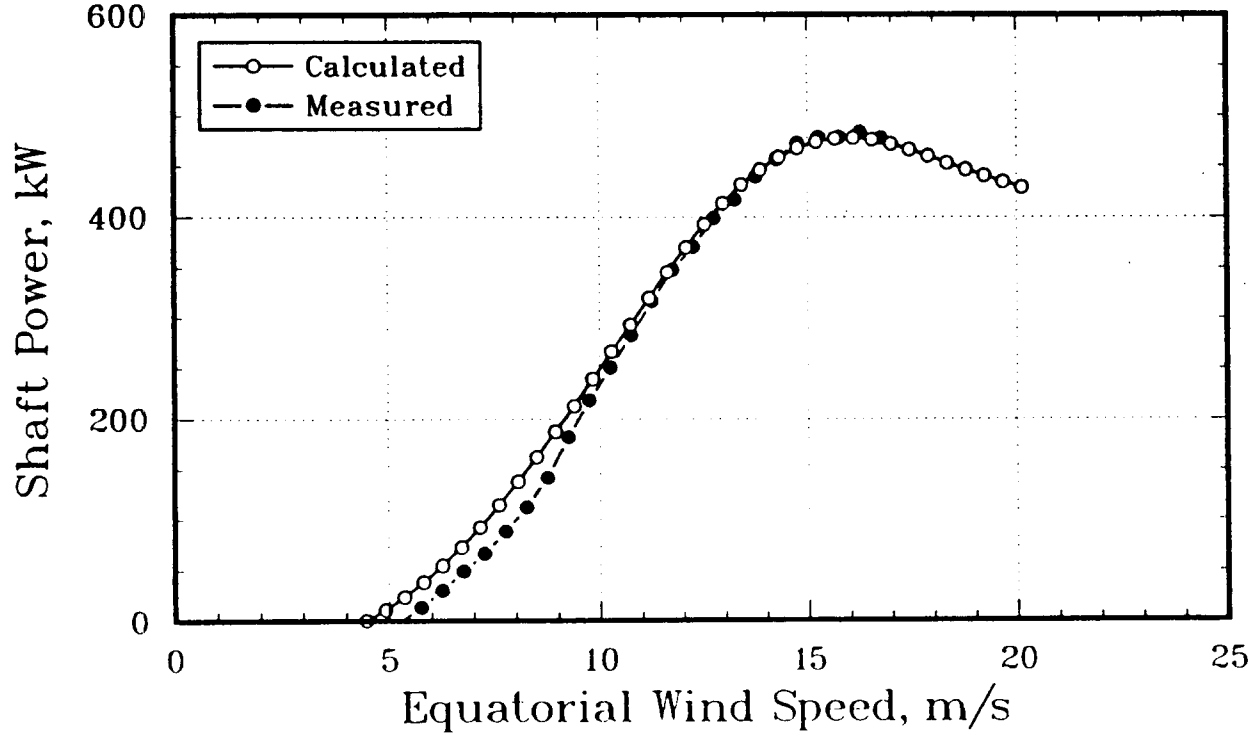

Figure 3.17. Rotor Power vs. Wind Speed at 34 RPM - Calculated and Measured

multiple streamtube code based on the CARDAA code (Paraschivoiu 1981). SLICEIT is a steady wind code and incorporates the Gormont dynamic stall model. In Figs. 3.16 and 3.17 SLICEIT calculations predict the values of maximum power and the associated wind speeds but over-predict the performance in winds of 5 to 10 m/s.

3.3.3 Effects of Joint Fairings and Bug Contamination

The over-predictions in the low winds observed in Figs. 3.16 and 3.17 are thought to be due primarily to drag on the blade-to-blade joints, which have many exposed bolt heads. To verify this, joint fairings were constructed over the four blade-to-blade joints on each blade. The fairings, made of lightweight foam epoxy, extend over the entire joint and were shaped to an aerodynamic surface. Test data collected with the faired blade joints are compared to the previous 28 rpm data set in Fig. 3.18. The 2/90 data set is the unfaired, clean blade data already shown, and the 12/90 data set is the case of clean blades with fairings installed. When compared to the "clean blades with no fairings" data, the "clean blades with fairings" data show improved performance at the low wind speeds from 4 to 11 m/s. Also, the "clean blades with fairings" data show significant improvement in winds greater than 17 m/s. This behavior may be partly due to stochastic effects and the availability of less data at these high winds.

Later in the spring of 1990 the blades became contaminated with bug residue. A set of data was collected at 28 rpm with the dirty, faired blades (4/90) and is compared to the clean, faired blade data in Fig. 3.19. Here we observe that the dirty blades exhibit lower performance in winds to 11 m/s, but then significantly outperform the clean blades in winds greater than 11 m/s. This increased performance in high winds by the dirty blades is the opposite of anything observed before on either HAWTs or VAWTs. This behavior is not clearly understood, but it is speculated that the bugs are acting like tiny vortex generators. Further study is underway to understand this phenomenon.

Tables VII and VIII present the 4/90 and 12/90 data in detail.

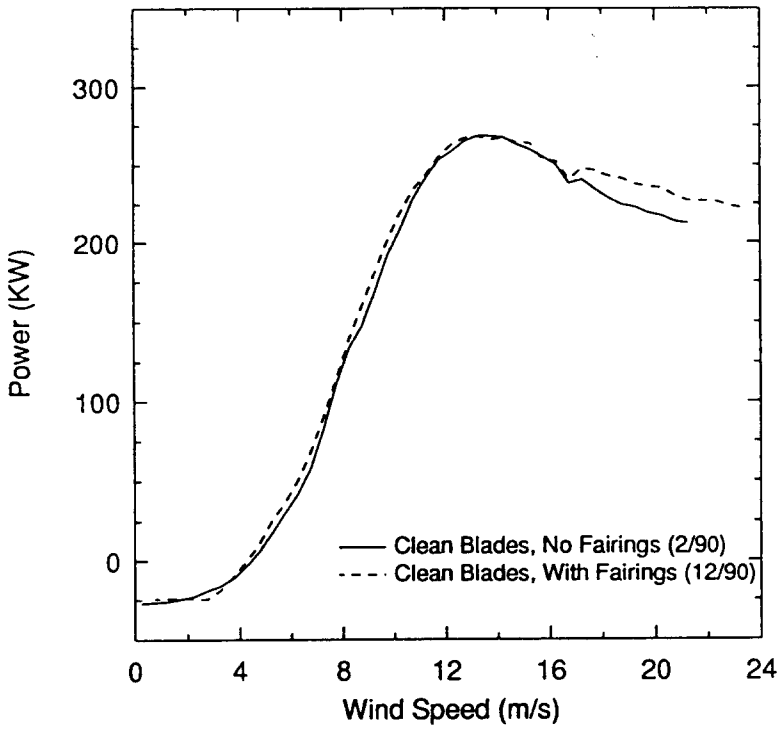

Figure 3.18. Effects of Joint Fairings on Rotor Power at 28 RPM

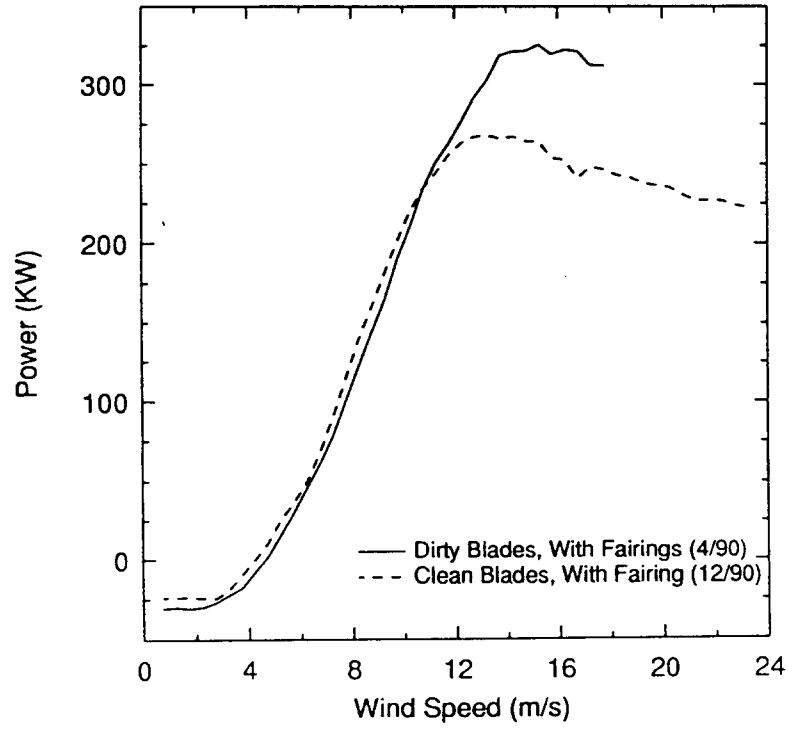

Figure 3.19 Effects of Bug Contamination on Rotor Power at 28 RPM

Table VII. Performance Data with Joint Fairings - 28 RPM

B281290: BU-34 Turbine at 28.0 RPM, Total # pts = 46520.
Sample rate = 20.000 HZ, Samples/pt = 43, min pts/bin = 100.
Air Density = 1.226 Kg/m**3(CH 41 Corrected)
CH 41 Tare Torque = .3000E+04 (Nm)
Series # Records:

1	1 2 3 4 5 6 7 8 9 10 11 12 13 14 15 16
2	1 2 3 4 5 6 7 8 9 10 11 12 13 14 15 16
3	1 2 3 4 5 6 7 8 9 10 11 12 13 14 15 16
4	1 2 3 4 5 6 7 8 9 10 11 12 13 14 15 16
5	1 2 3

CHAN # 41 (KNML) + TARE [Nm]

M/S	#PTS	PROB	MAV	RMV	RW/V	CP	KP	KW
.75	201	.0043	-.826E+04	.117E+04	65.48	-98.068	-.00035	-24.22
1.25	1162	.0249	-.821E+04	.123E+04	39.29	-21.057	-.00035	-24.08
1.75	1684	.0361	-.810E+04	.131E+04	28.06	-7.565	-.00034	-23.74
2.25	1034	.0221	-.835E+04	.162E+04	21.83	-3.669	-.00035	-24.47
2.75	1081	.0231	-.840E+04	.222E+04	17.86	-2.022	-.00035	-24.62
3.25	1226	.0263	-.646E+04	.265E+04	15.11	-.943	-.00027	-18.96
3.75	1205	.0258	-.339E+04	.286E+04	13.10	-.322	-.00014	-9.94
4.25	1409	.0302	-.116E+03	.276E+04	11.56	-.008	-.00000	-.34
4.75	1232	.0264	.355E+04	.319E+04	10.34	.166	.00015	10.40
5.25	1418	.0304	.871E+04	.450E+04	9.35	.301	.00037	25.53
5.75	1556	.0333	.126E+05	.538E+04	8.54	.331	.00053	36.85
6.25	1494	.0320	.171E+05	.630E+04	7.86	.351	.00072	50.12
6.75	1311	.0281	.232E+05	.725E+04	7.28	.378	.00098	68.09
7.25	1092	.0234	.308E+05	.820E+04	6.77	.404	.00130	90.17
7.75	1173	.0251	.391E+05	.908E+04	6.34	.421	.00165	114.75
8.25	1194	.0256	.476E+05	.967E+04	5.95	.425	.00201	139.69
8.75	1504	.0322	.544E+05	.102E+05	5.61	.407	.00230	159.65
9.25	1926	.0412	.616E+05	.107E+05	5.31	.390	.00261	180.75
9.75	1769	.0379	.685E+05	.110E+05	5.04	.370	.00290	200.88
10.25	1795	.0384	.749E+05	.112E+05	4.79	.348	.00317	219.66
10.75	1863	.0399	.799E+05	.113E+05	4.57	.322	.00338	234.19
11.25	1818	.0389	.833E+05	.114E+05	4.37	.293	.00352	244.16
11.75	1859	.0398	.871E+05	.114E+05	4.18	.269	.00368	255.45
12.25	1779	.0381	.898E+05	.113E+05	4.01	.245	.00379	263.19
12.75	1563	.0335	.911E+05	.111E+05	3.85	.220	.00385	267.20
13.25	1441	.0309	.915E+05	.108E+05	3.71	.197	.00387	268.21
13.75	1113	.0238	.908E+05	.104E+05	3.57	.175	.00384	266.11
14.25	861	.0184	.912E+05	.996E+04	3.45	.158	.00385	267.32
14.75	712	.0152	.902E+05	.949E+04	3.33	.141	.00381	264.50
15.25	680	.0146	.901E+05	.906E+04	3.22	.127	.00381	264.28
15.75	587	.0126	.865E+05	.860E+04	3.12	.111	.00366	253.75
16.25	582	.0125	.861E+05	.832E+04	3.02	.101	.00364	252.58
16.75	526	.0113	.821E+05	.798E+04	2.93	.088	.00347	240.84
17.25	540	.0116	.846E+05	.788E+04	2.85	.083	.00358	248.18
17.75	504	.0108	.841E+05	.779E+04	2.77	.075	.00355	246.45
18.25	534	.0114	.829E+05	.766E+04	2.69	.068	.00350	243.02
18.75	494	.0106	.823E+05	.742E+04	2.62	.063	.00348	241.46
19.25	418	.0090	.811E+05	.746E+04	2.55	.057	.00343	237.81
19.75	414	.0089	.806E+05	.751E+04	2.49	.052	.00341	236.29
20.25	366	.0078	.803E+05	.737E+04	2.43	.048	.00339	235.33
20.75	356	.0076	.786E+05	.736E+04	2.37	.044	.00332	230.55
21.25	326	.0070	.774E+05	.727E+04	2.31	.040	.00327	227.08
21.75	246	.0053	.774E+05	.730E+04	2.26	.038	.00327	226.99
22.25	189	.0040	.775E+05	.722E+04	2.21	.035	.00327	227.11
22.75	160	.0034	.765E+05	.751E+04	2.16	.033	.00323	224.27

Table VIII. Performance Data with Bug Contamination and Joint Fairings - 28 RPM

B280490: BU-34 Turbine at 28.0 RPM, Total # pts = 45939.
Sample rate = 20.000 HZ, Samples/pt = 43, min pts/bin = 100.
Air Density = 1.226 Kg/m**3(CH 41 Corrected)
CH 41 Tare Torque = .3000E+04 (Nm)
Series # Records:

1	1 2 3 4 5 6 7 8 9 10 11 12 13 14 15 16
2	1 2 3 4 5 6 7 8 9 10 11 12 13 14 15 16
3	1 2 3 4 5 6 7 8 9 10 11 12 13 14 15 16
4	1 2 3 4 5 6 7 8 9 10 11 12 13 14 15 16
5	1 2 3 4 5 6 7 8

CHAN # 41 (KNML) + TARE [Nm]

M/S	#PTS	PROB	MAV	RMV	RW/V	CP	KP	KW
.75	320	.0069	-.105E+05	.122E+04	65.48	-124.837	-.00044	-30.84
1.25	710	.0153	-.103E+05	.127E+04	39.29	-26.289	-.00043	-30.06
1.75	1160	.0250	-.105E+05	.132E+04	28.06	-9.838	-.00045	-30.87
2.25	1423	.0306	-.102E+05	.144E+04	21.83	-4.486	-.00043	-29.92
2.75	1363	.0293	-.929E+04	.168E+04	17.86	-2.237	-.00039	-27.24
3.25	1374	.0296	-.767E+04	.207E+04	15.11	-1.120	-.00032	-22.50
3.75	1430	.0308	-.613E+04	.233E+04	13.10	-.582	-.00026	-17.97
4.25	1480	.0319	-.281E+04	.266E+04	11.56	-.183	-.00012	-8.23
4.75	1621	.0349	.631E+03	.299E+04	10.34	.029	.00003	1.85
5.25	1782	.0384	.540E+04	.372E+04	9.35	.187	.00023	15.83
5.75	2024	.0436	.104E+05	.480E+04	8.54	.273	.00044	30.39
6.25	2249	.0484	.157E+05	.594E+04	7.86	.323	.00067	46.17
6.75	2454	.0528	.208E+05	.676E+04	7.28	.339	.00088	61.04
7.25	2337	.0503	.267E+05	.746E+04	6.77	.351	.00113	78.31
7.75	2195	.0473	.343E+05	.821E+04	6.34	.369	.00145	100.49
8.25	2073	.0446	.418E+05	.885E+04	5.95	.372	.00177	122.44
8.75	1999	.0430	.490E+05	.939E+04	5.61	.366	.00207	143.75
9.25	1983	.0427	.559E+05	.982E+04	5.31	.354	.00236	164.04
9.75	1954	.0421	.646E+05	.103E+05	5.04	.349	.00273	189.43
10.25	2002	.0431	.717E+05	.105E+05	4.79	.333	.00303	210.13
10.75	1802	.0388	.796E+05	.107E+05	4.57	.321	.00337	233.47
11.25	1725	.0371	.856E+05	.109E+05	4.37	.301	.00362	250.88
11.75	1691	.0364	.895E+05	.111E+05	4.18	.276	.00379	262.56
12.25	1557	.0335	.943E+05	.113E+05	4.01	.257	.00399	276.44
12.75	1258	.0271	.995E+05	.115E+05	3.85	.240	.00420	291.60
13.25	976	.0210	.103E+06	.116E+05	3.71	.222	.00436	302.54
13.75	729	.0157	.109E+06	.118E+05	3.57	.209	.00459	318.69
14.25	612	.0132	.110E+06	.116E+05	3.45	.190	.00463	321.26
14.75	443	.0095	.110E+06	.114E+05	3.33	.171	.00464	321.72
15.25	330	.0071	.111E+06	.111E+05	3.22	.157	.00469	325.61
15.75	249	.0054	.109E+06	.107E+05	3.12	.140	.00461	319.51
16.25	195	.0042	.110E+06	.105E+05	3.02	.128	.00465	322.39
16.75	166	.0036	.110E+06	.103E+05	2.93	.117	.00464	321.57
17.25	135	.0029	.107E+06	.979E+04	2.85	.104	.00450	312.42
17.75	138	.0030	.107E+06	.943E+04	2.77	.095	.00450	312.30

4.0 STRUCTURAL PERFORMANCE

A VAWT blade, as it rotates, is subjected to two main types of loading--steady loading, which consists of loads due to gravity and centrifugal effects, and vibratory loading, which is caused by the wind and consists of both harmonic (due to blade rotation) and random (due to turbulence in the wind) components. This section presents measured structural response data including gravity stresses, centrifugal stresses, and vibratory stresses consisting of both the harmonic and random components.

4.1 Gravity Stresses

After the completion of blade instrumention and before rotor assembly, the strain gauges were calibrated by hanging known weights from each blade section, recording the resulting strains, and comparing the measurements to analytical values. The entire set of gauges functioned correctly, and the measured strains agreed with predictions to within 2 % (Sutherland 1988).

To measure gravity stresses, the strain gauges were zeroed with the blades on the ground and then monitored immediately after blade mounting. The resulting strains were converted to stress values in MPa. Figure 4.1 illustrates the measured flatwise gravity stress distribution. Stresses along the blade (from top to bottom of the turbine) are plotted left to right on the x-axis, and positive stress corresponds to tension on the outboard side of the blade. The location of the different blade sections that make up the blade are noted along the x-axis. Also shown in Fig. 4.1 are analytical values, and it can be seen that the measured stress distribution is generally as predicted (Ashwill 1990). Discontinuities in the stress distribution occur at the joints where the blade stiffness changes; differences in the measured data between blades one and two are observed in the 36-inch and lower 42-inch sections.

4.2 Centrifugal Stresses

Figure 4.2 shows a time series record of rotation speed and an upper root, flatwise gauge. Since the strain gauges are zeroed before testing, the mean component of the flatwise stress signal during rotation is caused by centrifugal loading only. As the rpm increases from 0 to 40 rpm in Fig. 4.2, flatwise blade bending at the upper root increases due to the larger centrifugal loading. By averaging each flatwise gauge for 40 seconds at each rpm, centrifugal stresses are

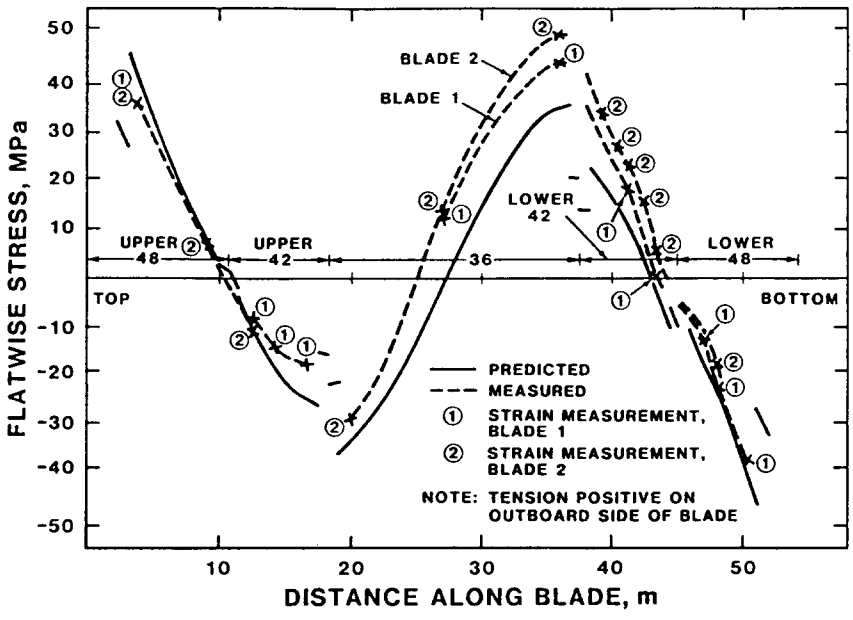

Figure 4.1. Gravity Stress Distribution

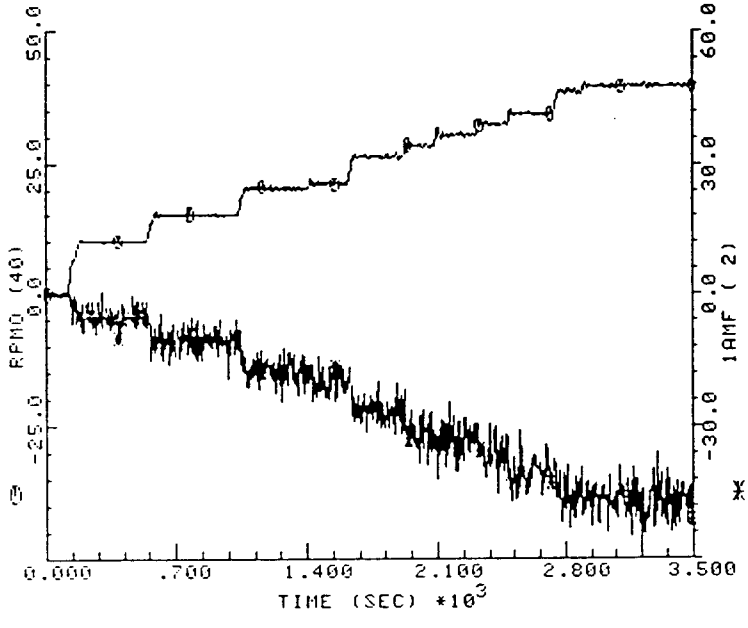

Figure 4.2. Upper Root, Flatwise Stress vs. RPM

determined. The increase of centrifugal stresses with higher rpm continues to offset the bending stresses due to gravity until the mean stresses are minimized at 37.5 rpm, the troposkien rpm (Ashwill and Leonard 1986). Figures 4.3 and 4.4 show the distribution of measured and predicted flatwise centrifugal stresses along the blade at 28 and 40 rpm. The stresses at the top (bottom) of the blade are plotted on the left (right) side of the x-axis. These plots show the very good agreement between measurements and predictions at both 28 and 40 rpm (Ashwill 1990).

4.3 Natural Frequencies

Before initial turbine operation, a modal test was performed on the parked rotor by Sandia's Modal Test Group. Accelerometers temporarily attached to the blades, tower and guy cables measured turbine motion. The measurements were used to estimate the mode shapes, their frequencies of vibration and modal damping values (Carne et al. 1989).

The first eight natural frequencies obtained from the modal test are compared to analytical predictions from a NASTRAN frequency analysis in Table IX. The mode number and shape are listed in the first two columns. The third column shows the natural frequencies for the stationary rotor measured by the modal test during wind excitation. Column four lists the analytical values. There is excellent agreement between the measured and predicted frequencies for these eight modes. All predicted modal frequencies are within 2.6% of the measurements except for the first blade edgewise mode (5.2%). Additional information about these comparisons is provided in Ashwill 1990.

Amplitude spectra were obtained from the strain gauge data collected during the resonance surveys. Modal frequencies and harmonic excitations (per revs) appear as peaks in the amplitude spectra. By plotting these measured natural frequencies at several rotation rates on the predicted fan-plot, as shown in Fig. 4.5, one can estimate the accuracy of predictive techniques. For example, the measured frequencies of the two first flatwise modes plotted in Fig. 4.5 are the antisymmetric and symmetric modes, which are predicted to vibrate at nearly the same frequency. The first blade edgewise mode (1BE) was under-predicted by 5% at zero rpm, but above 25 rpm the observed and predicted frequencies nearly coincide. The predicted natural frequencies below 3 Hz closely approximate the measured values over almost the entire range of operating speeds (Ashwill 1990).

4.4 Vibratory Stresses

Vibratory stresses are caused by wind loading and are often described

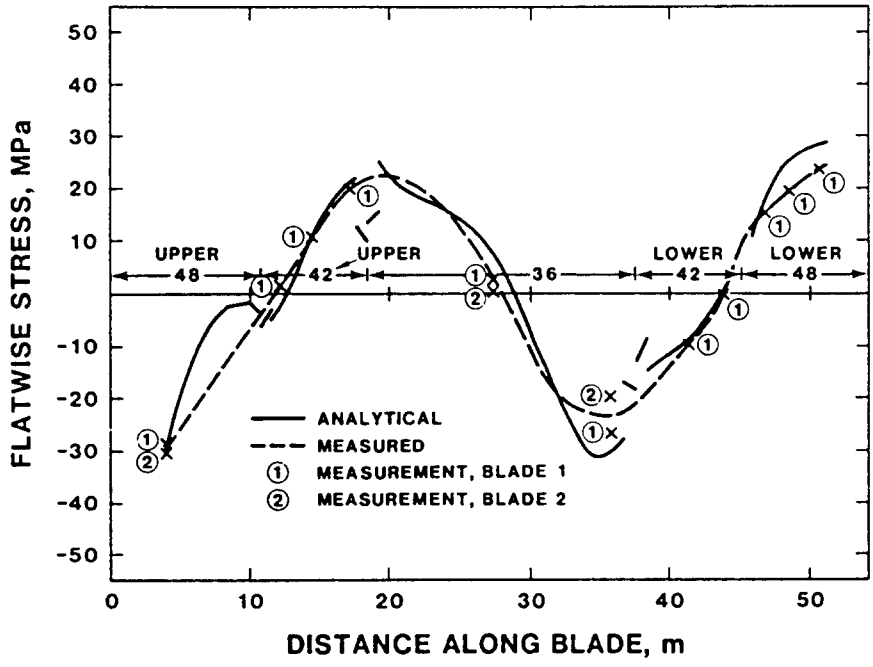

Figure 4.3. Centrifugal Stress Distribution at 28 RPM

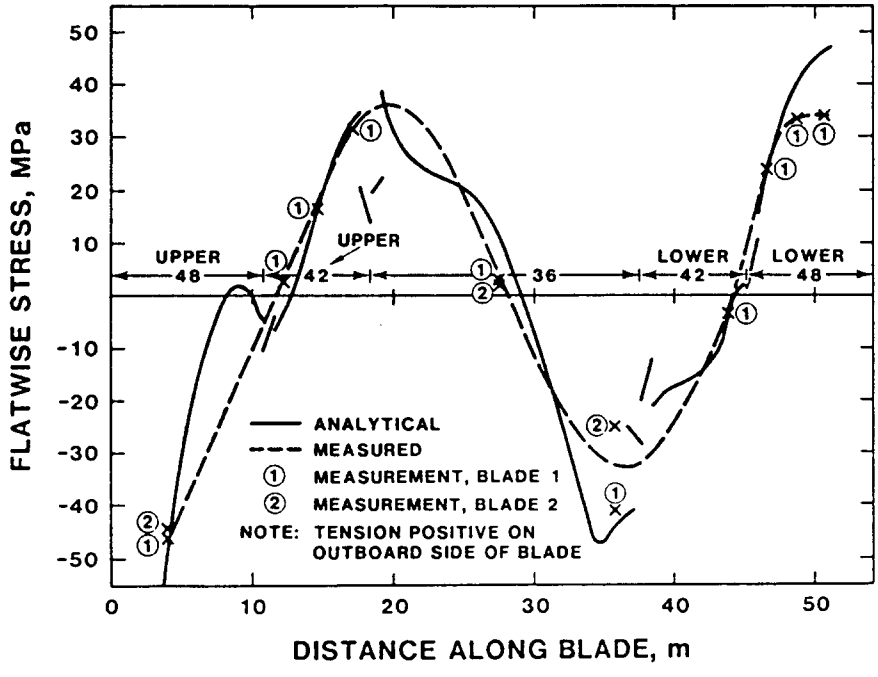

Figure 4.4. Centifugal Stress Distribution at 40 RPM

MODE NUMBER	MODE SHAPE*	MODAL TEST	ANALYT-ICAL	DEVIA-TION
1,2	1FA/1FS	1.06	1.05	1.0%
3	1Pr	1.52	1.56	2.6%
4	1BE	1.81	1.72	5.2%
5	2FA	2.06	2.07	0.5%
6	2FS	2.16	2.14	1.0%
7	1TI	2.50	2.46	1.6%
8	1TO	2.61	2.58	1.2%

* Mode Shape Abbreviation Key:
1FA = First Flatwise Antisymmetric
1FS = First Flatwise Symmetric
1Pr = First Propeller
1BE = First Blade Edgewise
2FA = Second Flatwise Antisymmetric
2FS = Second Flatwise Symmetric
1TI = First Tower In-Plane
1TO = First Tower Out-of-Plane

Table IX. Parked Modal Frequencies (Hz) - Test and Analysis

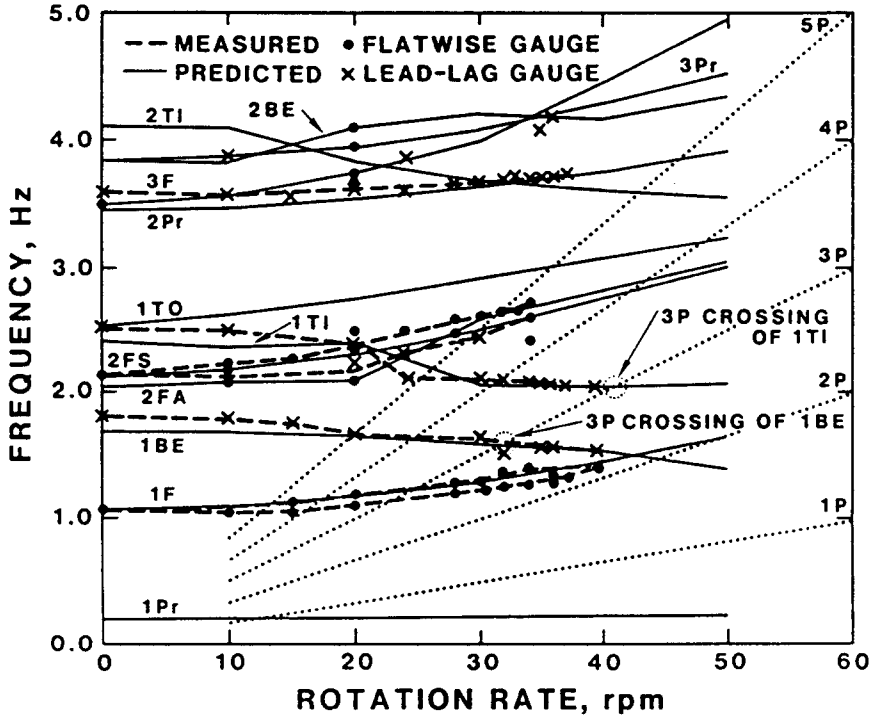

Figure 4.5. Rotating Modal Frequencies - Measured and Predicted

analytically by the root mean square (RMS) of the stress signal. For the measured data we use the root mean variances (RMV) of each stress bin which is identical to the RMS for these measurements.

Included in this report are binsed strain data for the 28, 34 and 38 rpm data sets. As previously mentioned, the data have been adjusted by calibration factors, which convert the strain signals to stress values in MPa. Each strain gauge has a four-digit identifier code that provides information about the gauge location and type of strain measurement. The first two digits of the identification code indicate the gauge location. For example,

> 1Q indicates that the gauge is located on blade one at the Q location. The schematic of Fig. 4.6 shows the locations of strain gauges.
>
> 1A through 1Q and 2A through 2X are strain gauges on blades one and two, respectively.
>
> TS indicates gauges located at the column (or tower) center and TT, the lower column.
>
> TU is a location on the lower shaft above the brakes and stand.

The last two digits of the code indicate the type of strain measurement. For example, gauge 1AML is a lead-lag (L) bending moment (M) gauge located on blade one at section A. The current set of active strain gauges, which are listed in Table X, measure mostly flatwise or lead-lag bending, however, a few measure average axial strain across the blade section or direct strain at a particular location. The lead-lag bending gauges are calibrated to provide the maximum bending stress, which occurs at the trailing edge. There are some 70 strain gauges available, but only 30 are active at a time. As of this writing four gauges have failed and been replaced in the data acquisition system by working gauges.

Table X. Test Bed Strain Gauges

Channel Number	Code	Measurement Type (Units)
01	1AML	Lead-lag Bending (MPa)
02	1AMF	Flatwise Bending (MPa)
03	1DMF	Flatwise Bending (MPa)

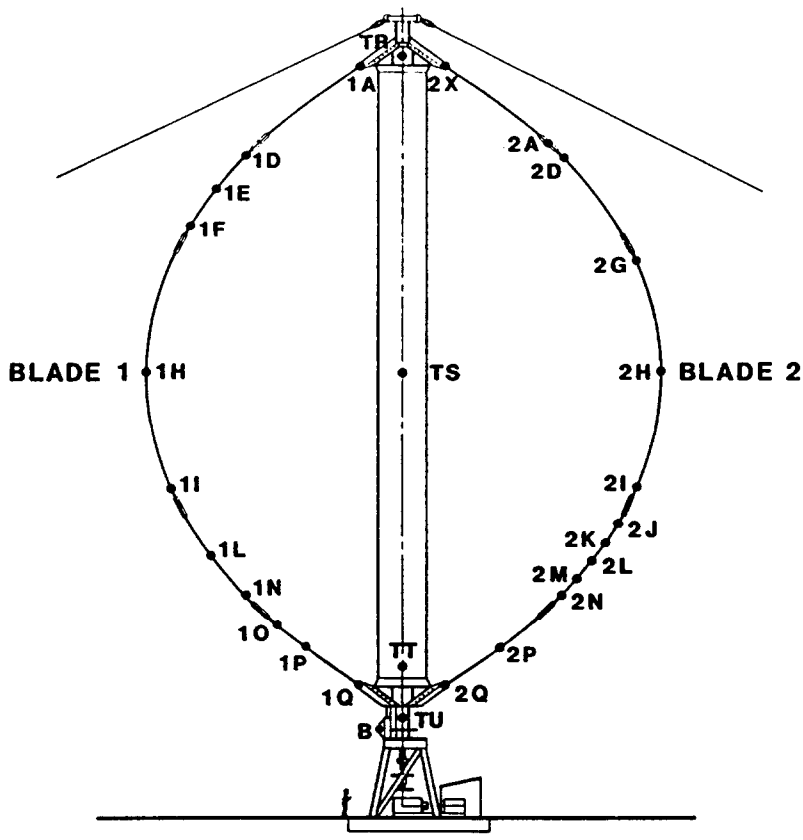

Figure 4.6. Strain Gauge Locations

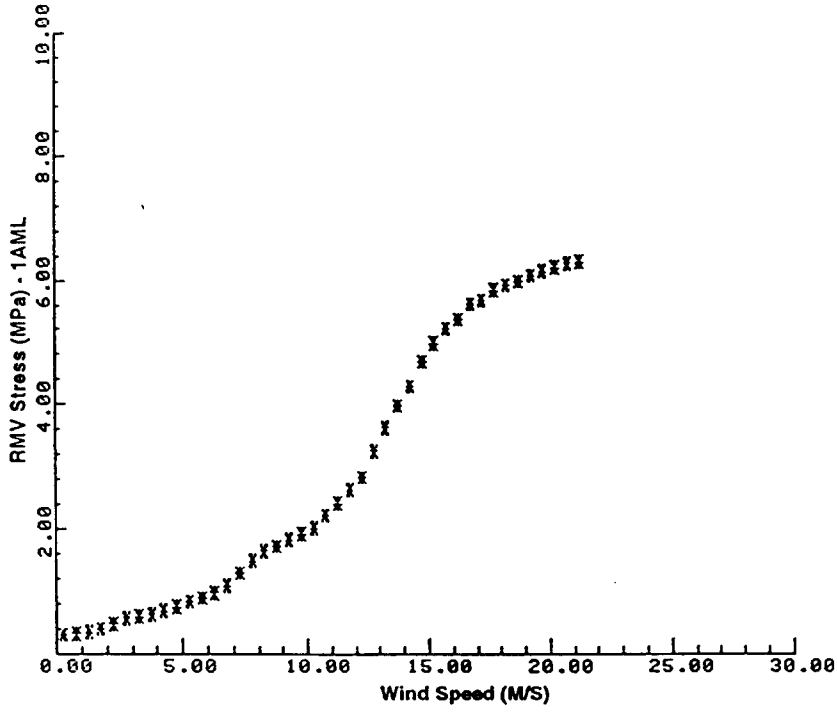

Figure 4.7. Upper Root, Flatwise RMV Stress vs. Wind Speed at 28 RPM

Table X. (continued)

04	1EML	Lead-lag Bending (MPa)
05	1EMF	Flatwise Bending (MPa)
06	1FMF	Flatwise Bending (MPa)
07	2HML	Lead-lag Bending (MPa)
08	2HF1	Flatwise Bending (MPa)
09	1HAF	Average Axial (MPa)
10	1IMF	Flatwise Bending (MPa)
11	1LML	Lead-lag Bending (MPa)
12	1LMF	Flatwise Bending (MPa)
13	TSMI	Tower In-plane Bending (MPa)
14	TSMO	Tower Out-of-plane Bending(MPa)
15	1NMF	Flatwise Bending (MPa)
16	1OMF	Flatwise Bending (MPa)
17	1PMF	Flatwise Bending (MPa)
18	1PAL	Average Lead-lag Axial (MPa)
19	1PAF	Average Flatwise Axial (MPa)
20	1QML	Lead-lag Bending (MPa)
21	1QMF	Flatwise Bending (MPa)
22	2XML	Lead-lag Bending (MPa)
23	2XMF	Flatwise Bending (MPa)
24	2HMF	Flatwise Bending (MPa)
25	TURT	Torsional Stress (MPa)
26	2IDF	Direct Strain (Stress,MPa)
27	2NDF	Direct Strain (Stress,MPa)
28	2QDF1	Direct Strain (Stress,MPa)
29	2QDF2	Direct Strain (Stress,MPa)
30	2QDF3	Direct Strain (Stress,MPa)

Figure 4.7 is a bins plot of the root mean variance (RMV) of stress versus wind speed at 28 rpm for gauge 1AMF. This gauge is located on blade one at the upper root and measures flatwise bending. As can be seen in Fig. 4.7, the flatwise stress at this location increases with increasing wind speed. The units of stress are megapascals (MPa). (1 MPa is 145 psi.)

Appendices A, B, and C contain sets of RMV stress vs. wind speed plots for the active strain gauges of the 28, 34 and 38 rpm data sets, respectively. The data sets are composed of the same bin records used for the plots described in the aerodynamic performance section (3.0). Tables XI, XII, and XIII summarize the RMV stress data at wind speeds of 6.75 m/s (15 mph), 11.25 m/s (25 mph), 15.75 m/s (35 mph) and 20.25 m/s (45 mph).

Table XI. Summary of RMV Stresses (MPa) at 28 RPM

	Wind Speed (m/s)					Wind Speed (m/s)			
	6.75	11.25	15.75	20.25		6.75	11.25	15.75	20.25
Gauge Code					Gauge Code				
1AMF	2.22	3.91	7.18	9.93	1AML	1.09	2.42	5.21	6.22
1DMF	1.05	2.17	5.32	8.14					
1EMF	1.31	2.53	5.79	8.74	1EML	0.78	1.34	2.74	3.41
1FMF	1.51	2.78	5.60	8.13	2HML	0.56	1.26	2.62	3.33
1IMF	2.76	4.50	6.84	8.71					
1LMF	1.16	2.01	4.57	7.13	1LML	0.85	1.49	3.08	3.72
1NMF	0.86	1.67	3.76	5.81					
1OMF	1.10	1.75	2.60	3.20					
1PMF	1.71	2.73	4.14	5.28					
1QMF	2.69	4.30	7.09	9.55	1QML	0.98	1.85	4.52	5.52
2XMF	2.86	4.76	6.76	8.70	2XML	0.80	1.53	2.22	2.54
2HMF	1.27	2.45	4.09	6.37					
TSMI	0.87	1.69	3.79	5.86	TSMO	0.31	0.68	1.15	1.39
1PAF	0.36	0.59	1.11	1.34	1PAL	0.17	0.27	0.43	0.51
TURT	0.16	0.20	0.17	0.14					
2IDF	2.89	4.87	7.30	9.76	2NF1	0.93	1.87	3.51	5.32
2HF1	1.71	3.17	4.73	7.02					
QDF1	2.35	4.30	6.72	9.11					
QDF3	2.67	4.46	6.97	9.35					

Table XII. Summary of RMV Stresses (MPa) at 34 RPM

	Wind Speed (m/s)					Wind Speed (m/s)			
	6.75	11.25	15.75	20.25		6.75	11.25	15.75	20.25
Gauge Code					Gauge Code				
1AMF	2.47	4.34	7.09	10.10	1AML	1.16	2.55	5.12	7.21
1DMF	1.26	2.33	4.40	6.62					
1EMF	1.50	2.70	4.92	7.55	1EML	0.88	1.74	2.80	3.81
1FMF	1.63	2.94	5.11	7.58	2HML	0.56	1.36	2.94	3.98
1IMF	3.04	5.01	7.19	9.18					
1LMF	1.43	2.35	3.82	5.54	1LML	0.94	1.88	3.12	4.24
1NMF	0.99	1.80	3.24	4.70					
1OMF	1.18	1.93	2.81	3.64					
1PMF	1.93	3.16	4.47	5.69					
1QMF	3.19	5.17	7.47	9.66	1QML	1.05	2.19	4.46	6.35
2XMF	3.07	5.26	7.67	9.62	2XML	0.95	1.86	2.80	3.44
2HMF	1.49	2.67	4.49	6.26					
TSMI	0.98	1.81	3.27	4.75	TSMO	0.41	0.78	1.25	1.56
1PAF	0.42	0.77	1.17	1.53	1PAL	0.18	0.31	0.52	0.67
TURT	0.14	0.16	0.17	0.16					
2IDF	3.19	5.46	8.17	10.40	2NF1	1.01	1.88	3.58	5.34
2HF1	1.97	3.58	5.51	7.10					
QDF1	2.68	3.49	4.03	4.45					
QDF3	3.08	5.25	8.13	10.40					

Table XIII. Summary of RMV Stresses (MPa) at 38 RPM

	Wind Speed (m/s)				Wind Speed (m/s)		
	6.75	11.25	15.75		6.75	11.25	15.75
Gauge Code				Gauge Code			
1AMF	2.85	4.25		1AML	2.13	3.98	
1DMF	1.66	2.58					
1EMF	1.85	2.77		1EML	1.43	2.60	
1FMF	1.90	2.99		2HML	1.16	2.12	
1IMF	3.28	4.87					
1LMF	1.77	2.58		1LML	1.59	2.87	
1NMF	1.23	2.00					
1OMF	1.33	1.83					
1PMF	2.14	3.13					
1QMF	3.67	5.31		1QML	2.08	3.77	
2XMF	3.27	5.17		2XML	1.08	2.03	
2HMF	1.84	2.83					
TSMI	1.23	2.02		TSMO	0.41	0.84	
1PAF	0.61	1.07		1PAL	0.25	0.39	
TURT	0.13	0.14					
2IDF	3.51	5.49		2NF1	1.22	1.98	
2HF1	2.34	3.78					
QDF1	2.14	3.52					
QDF3	3.52	5.60					

Several trends are evident:

1. The blade roots have the highest lead-lag and flatwise vibratory stresses at a given wind speed--for all three rotation rates.

2. Stresses increase (not necessarily linearly) with increased wind speed for all gauges at the three rotation rates.

3. Lead-lag stresses increase as rpm increases from 28 to 34 to 38 rpm for a given windspeed.

4. Flatwise stresses do not necessarily increase with increased rpm for a given windspeed.

5. Tower in-plane bending stresses are significantly higher than tower out-of-plane bending stresses at a given rpm and windspeed.

6. Torsional stresses in the lower shaft above the brakes are very low.

7. Vibratory stresses at the upper root of blade one are similar in value to those at the lower root of blade one (for both the flatwise and lead-lag directions). As one would expect, upper root flatwise stresses at a given location on blade one and two are very comparable in magnitude. However, the upper root *lead-lag* stresses of blade two are significantly lower than those of blade one. This difference is puzzling as the blades are identical to each other, and each should provide the same amount of torque to the tower.

Measured vibratory stresses (both flatwise and lead-lag) have recently been compared to steady wind and turbulent wind predictions (Ashwill and Veers 1990). The steady wind predictions are reasonably close to measured values in low winds (up to 11.25 m/s), but diverge from measured values in high winds (Figs. 4.8 and 4.9). The turbulent wind predictions were determined with TRES4 (Malcolm 1988), and the few data points available show good agreement to measured values at most wind speeds and rotation rates. More work is required to determine analytical aeroelastic damping values (Figs. 4.10 and 4.11), and questions still exist about the aerodynamic loading models in the stall regime. (The labels "+Aero" and "No Aero" in Figs. 4.10 and 4.11 indicate analytical results that include or exclude aeroelastic damping.)

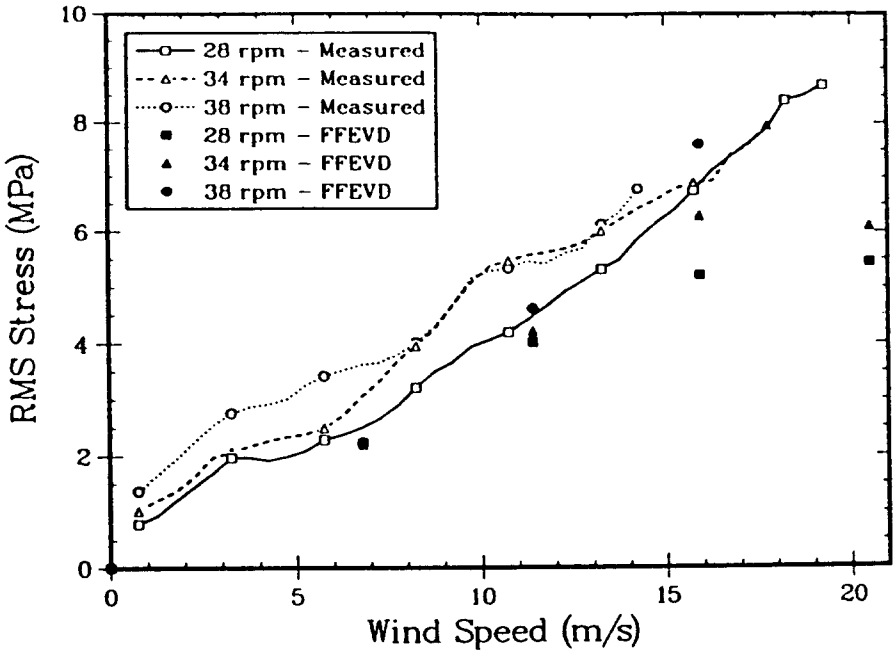

Figure 4.8. Lower Root, Flatwise RMS Stress vs. Wind Speed - Measured and Analytical (FFEVD) Without Turbulence

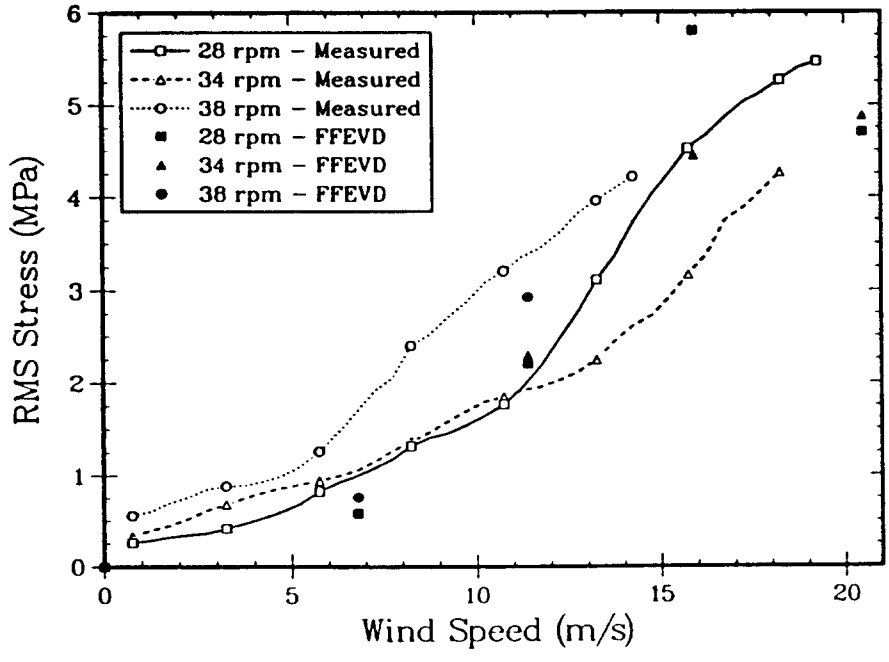

Figure 4.9. Lower Root, Trailing Edge RMS Stress vs. Wind Speed - Measured and Analytical (FFEVD) Without Turbulence

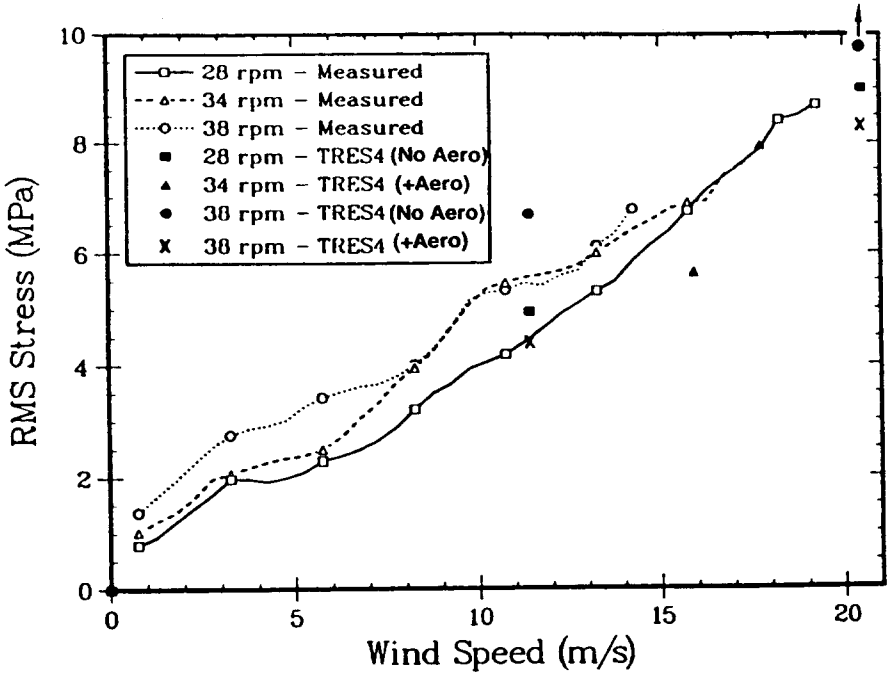

Figure 4.10. Lower Root, Flatwise RMS Stress vs. Wind Speed - Measured and Analytical (TRES4) With Turbulence

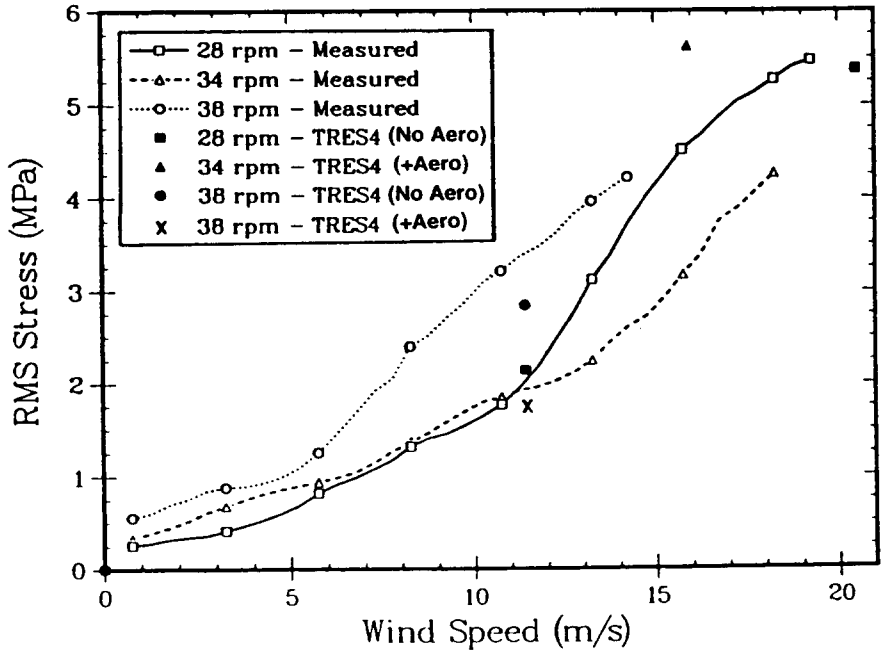

Figure 4.11. Lower Root, Trailing Edge RMS Stress vs. Wind Speed - Measured and Analytical (TRES4) With Turbulence

5.0 SELECTED TIME HISTORIES AND STRESS AMPLITUDE SPECTRA

5.1 Start-up Torque

The time history of Fig. 5.1 shows a turbine start-up followed by a ramping to 28 rpm in winds that average 16.0 m/s. Wind speed, rpm, and rotor torque are displayed on the plot. Torque transients with a range as high as 230 kNm occur when the turbine first begins turning. This is observed more clearly in Fig. 5.2, a smaller time segment of the data shown in Fig. 5.1.

5.2 Normal Operation

Figure 5.3 is a 200-second time history plot of wind speed, rpm, and rotor torque while the Test Bed operates at 34 rpm in winds averaging 10.8 m/s. The rpm signal contains an oscillation with a period of 30 to 40 seconds, which is due to the variable speed controller. The torque signal contains both the normal two per revolution oscillation and a 30- to 40-second oscillation similar to but lagging the rpm oscillation.

During the same time series we can examine flatwise and lead-lag (trailing edge) bending gauges at the upper root on blade one. These 100-second traces are shown in Fig. 5.4. Both gauges exhibit oscillation, the lead-lag gauge around a mean of -1.47 MPa and the flatwise gauge around a mean of -39.3 MPa. The larger mean value for the flatwise gauge is due to centrifugal loading.

A spectral analysis performed on these two gauges results in the plots shown in Figs. 5.5 and 5.6. Spectra from four data blocks each 25 seconds long are averaged together for each channel. In Fig. 5.5, the amplitude spectrum for the lead-lag gauge, we observe large spikes due to the one and three per-rev rotor harmonics at 0.567 and 1.7 Hz and stochastic wind excitations of natural frequencies between two and three per-rev and above three per-rev. Similarly, in Fig. 5.6, the amplitude spectrum for the flatwise gauge, we note harmonic spikes at one, two, and three per-rev in addition to responses due to stochastic excitation. The large spike just above 2P is the first flatwise mode of the blades.

5.3 Braking Data

An important feature of the Test Bed with its variable speed generator

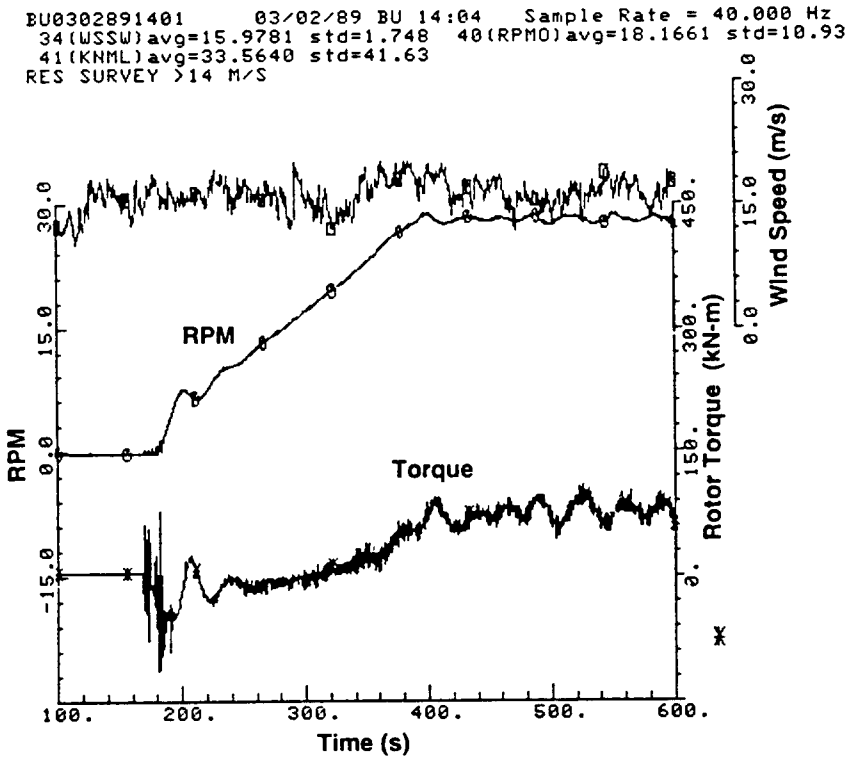

Figure 5.1. Turbine Start and Ramp-up to 28 RPM

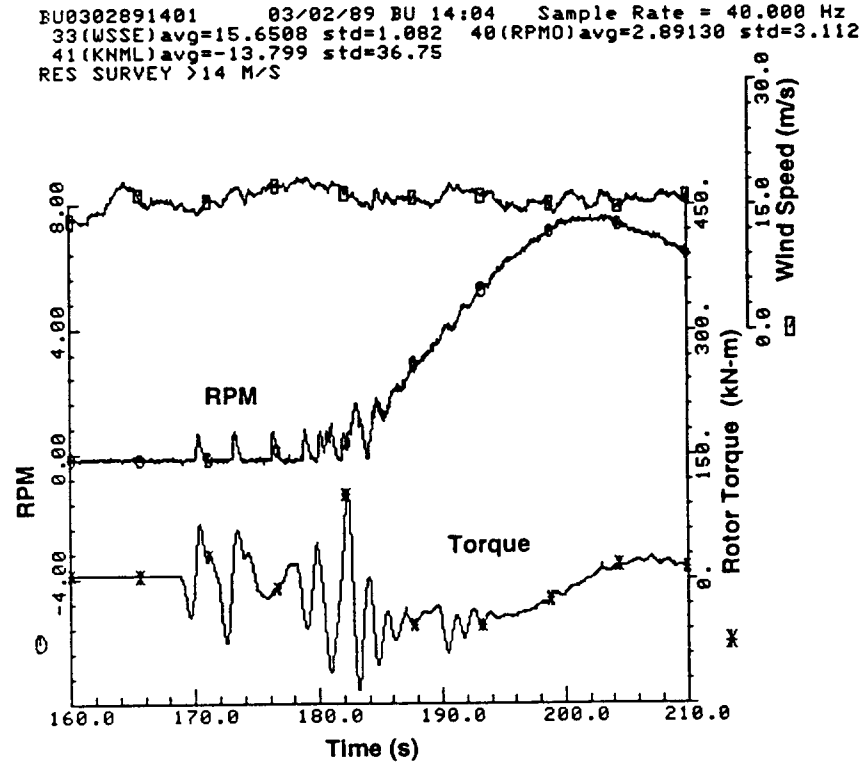

Figure 5.2. Torque during Start-up

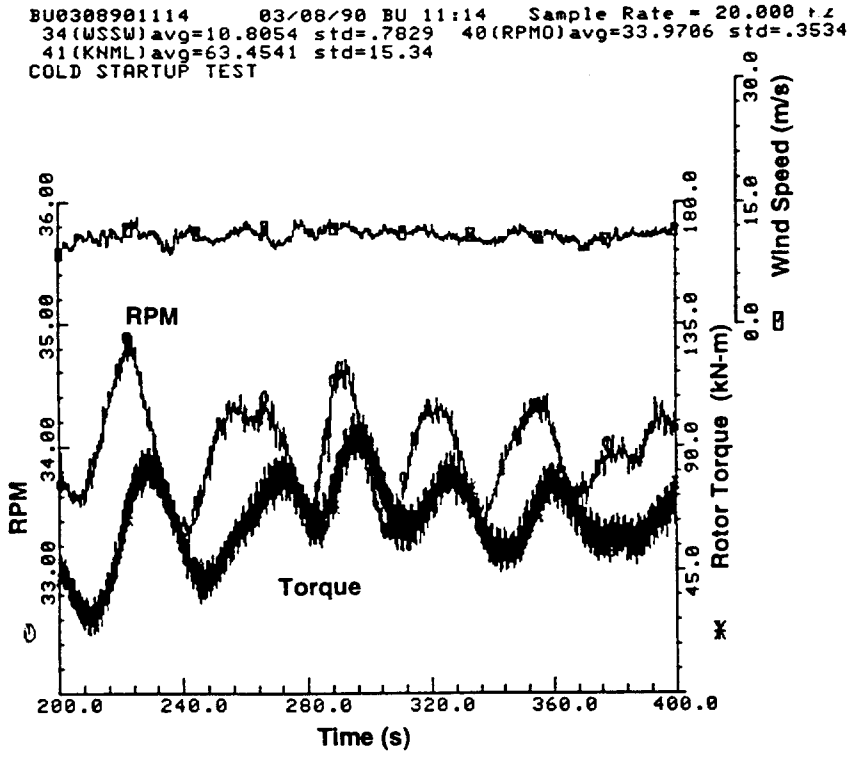

Figure 5.3. Normal Operation at 34 RPM - 200 Second Interval

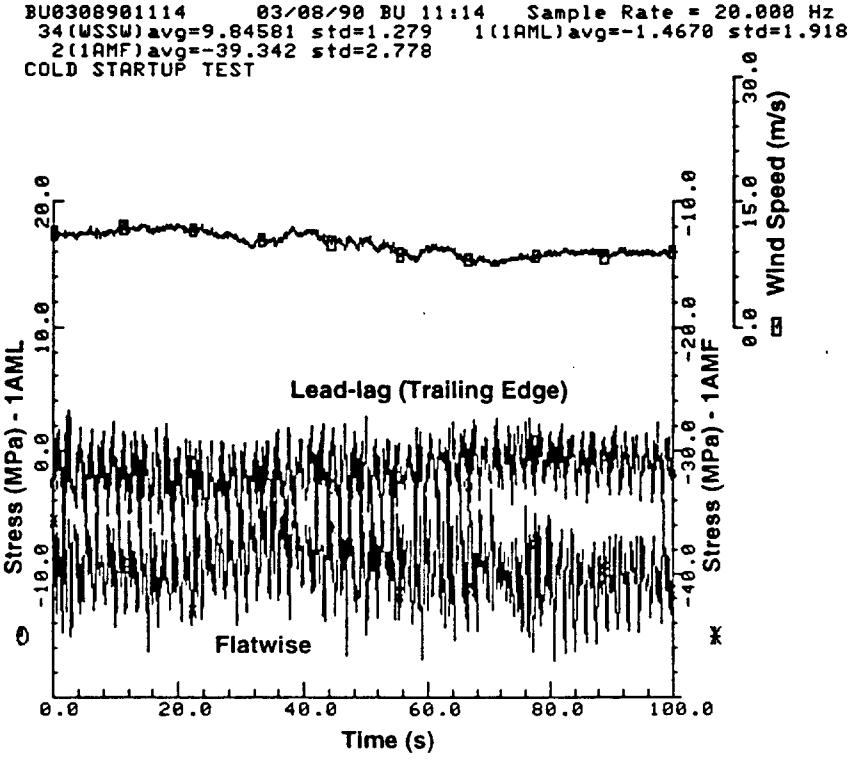

Figure 5.4. Normal Operation at 34 RPM - Flatwise and Trailing Edge Gauges

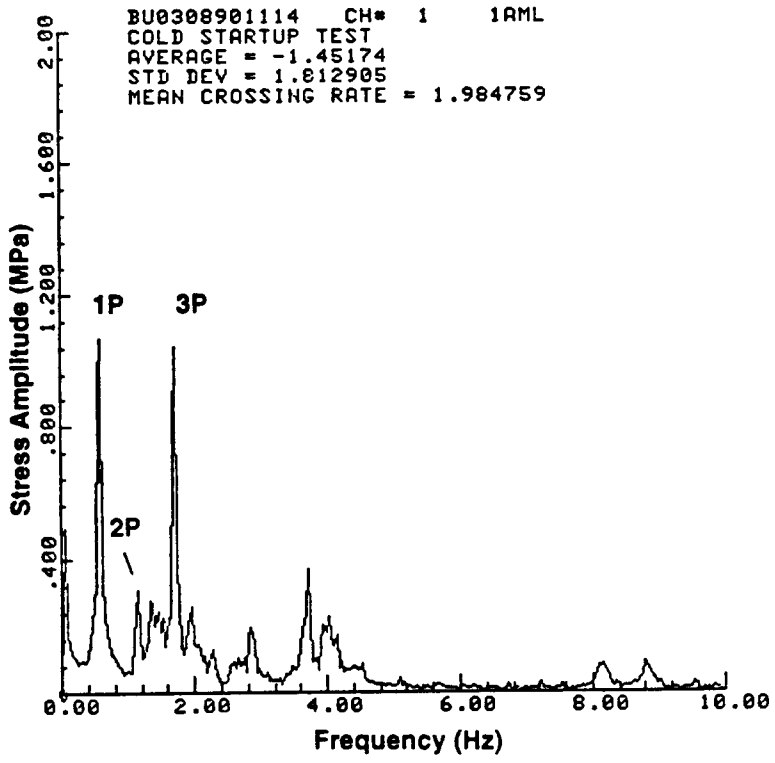

Figure 5.5. Stress Amplitude Spectra (4 Blocks) for an Upper Root, Trailing Edge Gauge at 34 RPM

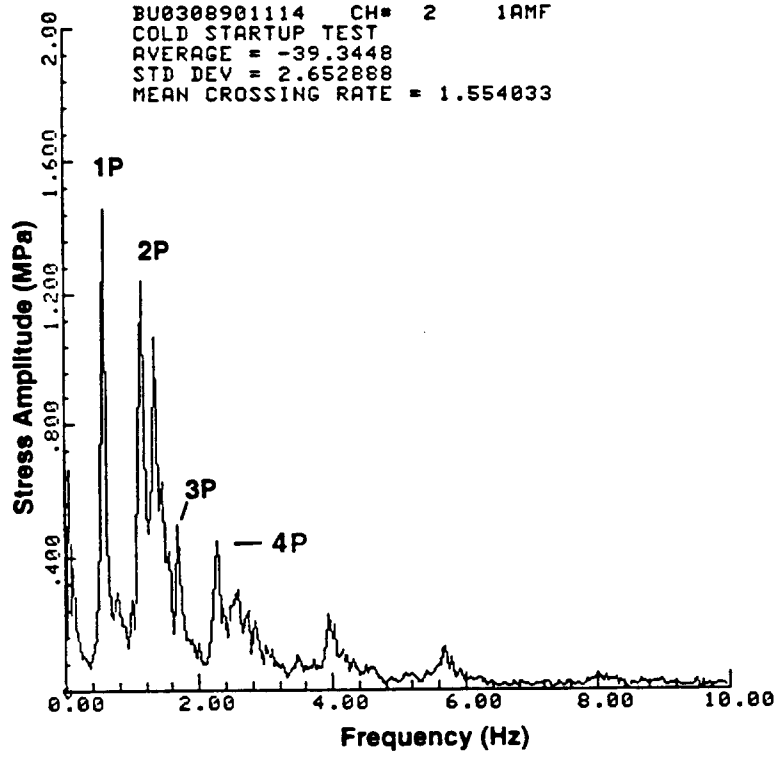

Figure 5.6. Stress Amplitude Spectra (4 Blocks) for an Upper Root, Flatwise Gauge at 34 RPM

is the capability to brake the turbine in different ways. There are three types of stopping:

1. Normal
2. Alarm
3. Emergency

For a normal stop the generator slowly ramps the turbine down from its operating rpm, and when 6 rpm is reached, two of the four brake calipers are applied to the brake disc to complete the stop. Figure 5.7 shows the rotor torque, rpm and wind speed during a typical normal stop. The torque plot shows oscillations larger than normal when the brakes are applied and for a few seconds after the turbine has stopped. Lead-lag stresses at the root (Fig. 5.8) increase during the braking and then oscillate around zero in a decaying fashion after the rotor stops. The largest stress range is approximately 10 MPa. Root flatwise stresses are only slightly impacted by this stop (Fig. 5.8).

In an alarm stop the turbine is quickly ramped down to 6 rpm at rate of 1 rpm per second and then two calipers are applied after a normal delay of 20 seconds at 6 rpm. An example of an alarm stop is shown in Fig. 5.9. In this particular stop there was a delay at 6 rpm of only a couple of seconds. During the ramp-down period the torque remains above 120 kNm (positive torque). When the turbine reaches 6 rpm and the brakes are applied, large torque oscillations with ranges as high as 150 kNm occur (Fig. 5.9). The largest lead-lag stress range during the stop is less than 15 MPa (Fig. 5.10), and the flatwise stresses are not affected by the stop, which occurred in winds of 6.5 m/s (Fig. 5.10).

An emergency stop takes place at any rpm when an emergency fault is detected. At that point all four brake calipers are immediately applied, and the turbine comes to a quick stop. Figure 5.11 is an example of an emergency stop. In this case the turbine is operating at 28 rpm in winds of 11.8 m/s when an emergency stop is initiated, and the turbine stops in about 7 seconds. Torque oscillations as high as 150 kNm occur during braking and immediately after the turbine stops. Figure 5.12 shows root lead-lag and flatwise stresses during the stop. The largest lead-lag stress range is 30 MPa, and again, flatwise stresses are only slightly affected.

As expected, the level of lead-lag stress oscillation is higher for an emergency stop than for an alarm stop, which is higher than for a normal stop. The level of

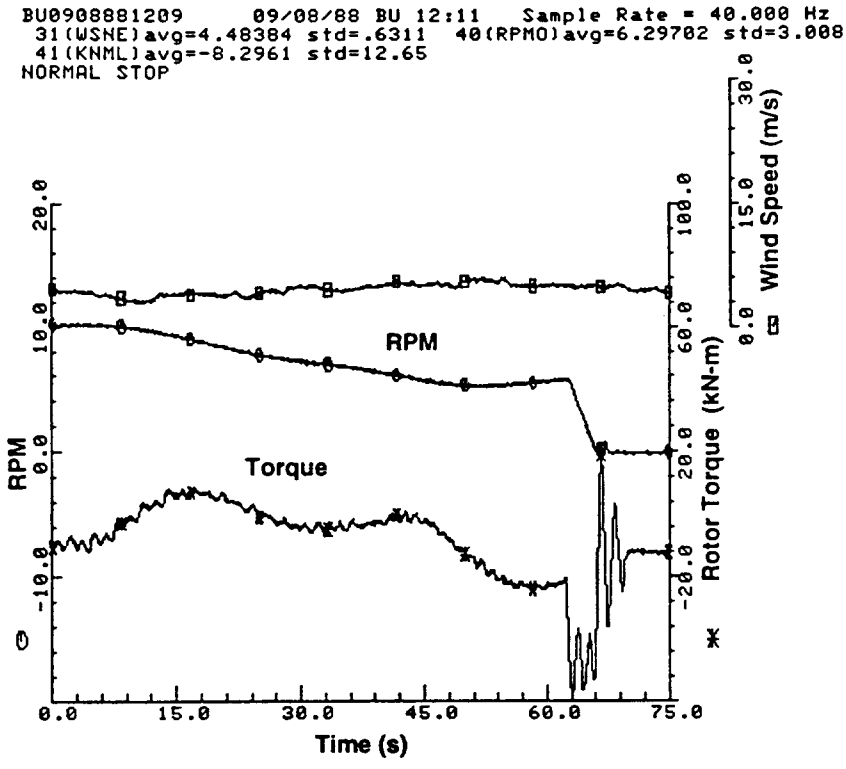

Figure 5.7. Torque during Normal Stop

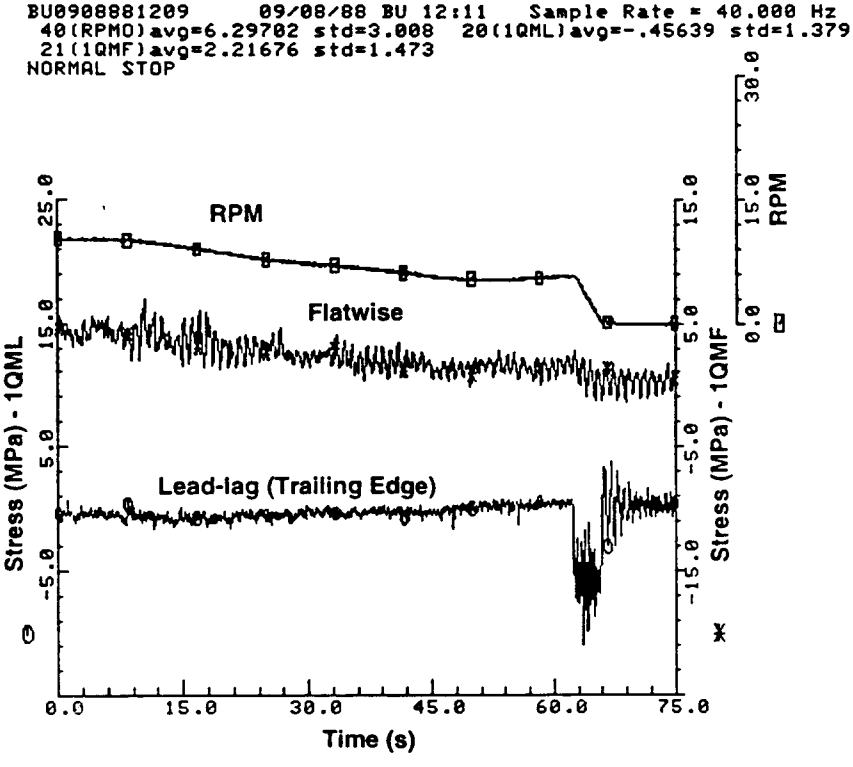

Figure 5.8. Blade Stresses during Normal Stop

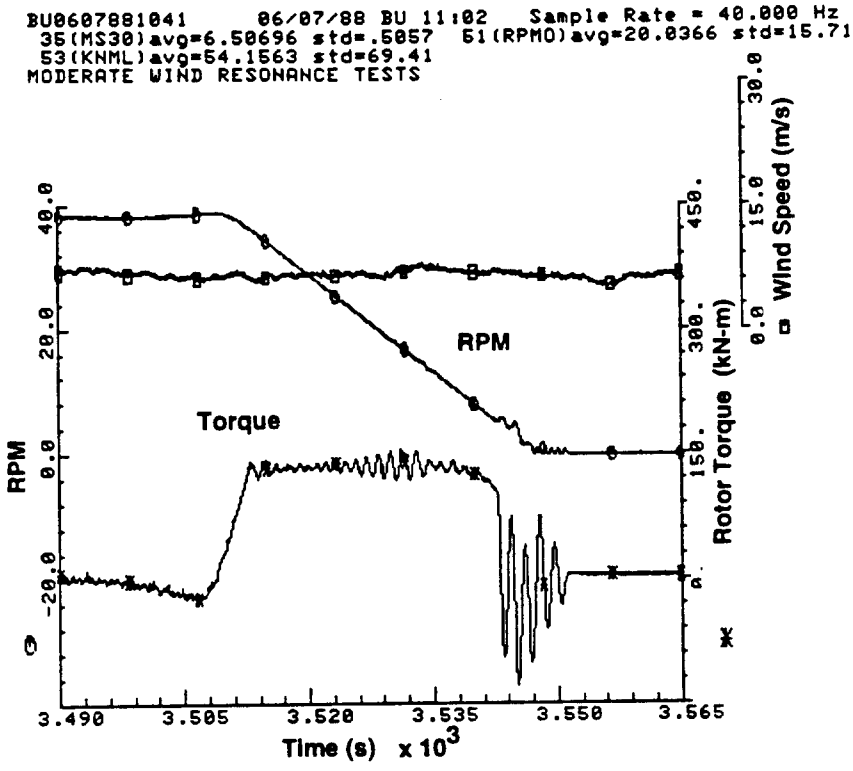

Figure 5.9. Torque during Alarm Stop from 40 RPM

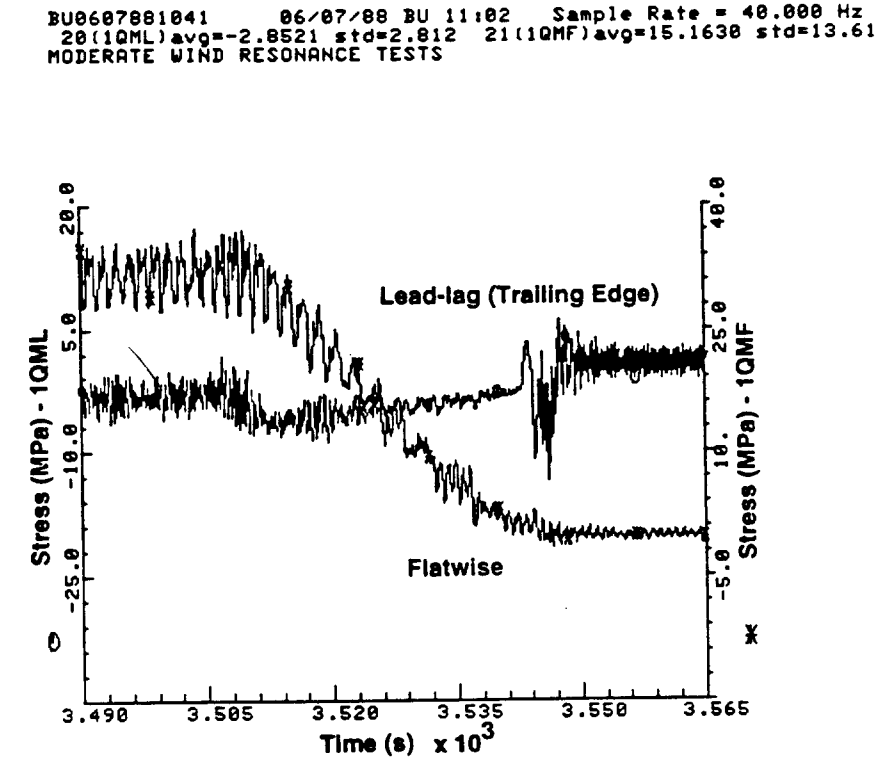

Figure 5.10. Blade Stresses during Alarm Stop

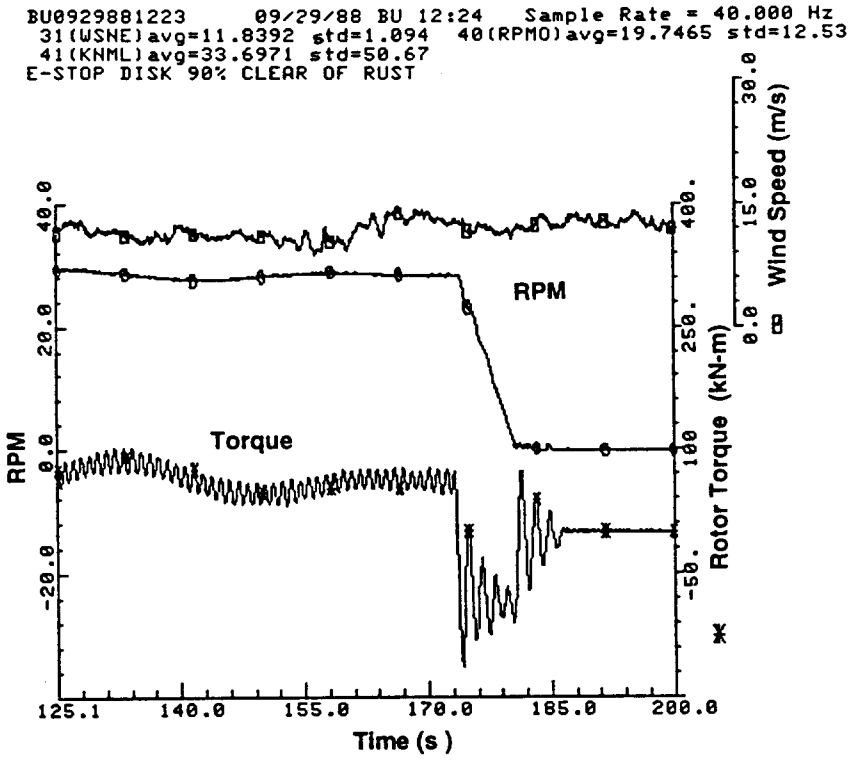

Figure 5.11. Torque during Emergency Stop from 28 RPM

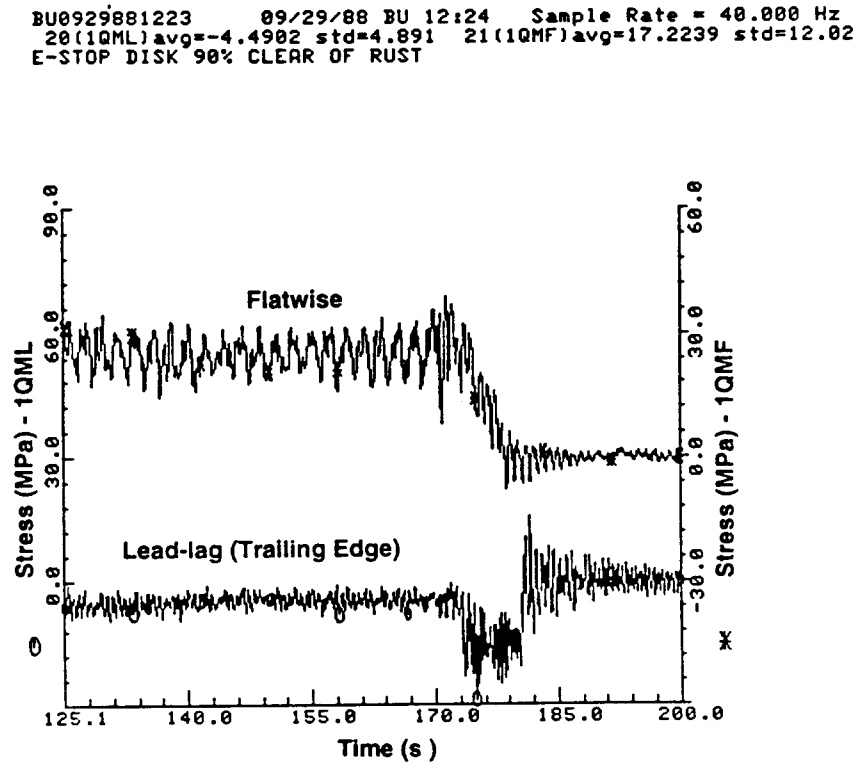

Figure 5.12. Blade Stresses during Emergency Stop

braking torque applied to the turbine has been adjusted to provide a quick stopping time but with acceptable stress levels.

5.4 Torque Ripple

Torque ripple is defined as a harmonic oscillation of torque about some mean value, and its magnitude is given by the following (Reuter and Worstell 1978):

$$\text{Torque Ripple} = (T_{max} - T_{mean}) / T_{mean}$$

Aerodynamic torque at the base of the rotor will approach 100%. The drive train must be designed to withstand this ripple and also attenuate it for the input to the generator. The Test Bed low-speed drive shaft consists of a steel shaft, the low-speed torque sensor, and two pairs of steel plates each connected by many rubber isolators. (See Fig. 5.13, an assembly drawing of the turbine stand and drive train.) The number of rubber isolators can be adjusted to change the shaft stiffness and affect the level of torque ripple and the torsional frequencies of the drive train. Figure 5.14 is a short time history of torque at 28 rpm in winds of 10 m/s. The torque ripple at the torque sensor is approximately 25%; however, the torque sensor sits between the two pairs of rubber isolators indicating the ripple seen at the generator should be even more attenuated. Figure 5.15 plots system power measured at the generator over the same time period. (Positive power to the grid is plotted as negative values.) Here we observe the average power ripple to be reduced significantly to approximately 5%. The low-speed shaft was designed to reduce the torque ripple to 17%.

Figures 5.16 and 5.17 show similar plots of torque and power ripple for the turbine operating at 34 rpm in winds of 11 m/s. The average torque ripple is approximately 11% and the power ripple about 2%. Similar plots are shown in Figs. 5.18 and 5.19 for 38 rpm in winds of 11 m/s. The torque ripple is approximately 13% and the power ripple about 2-3%.

5.5 Stress Amplitude Spectra

During Phase I and Phase II testing a significant effort was expended on understanding the structural dynamic behavior of the Test Bed. The turbine natural frequencies were determined by performing spectral analyses in conjunction with modal tests. Recently, we developed the capability to perform a spectral analysis of data over a longer operating period by averaging several

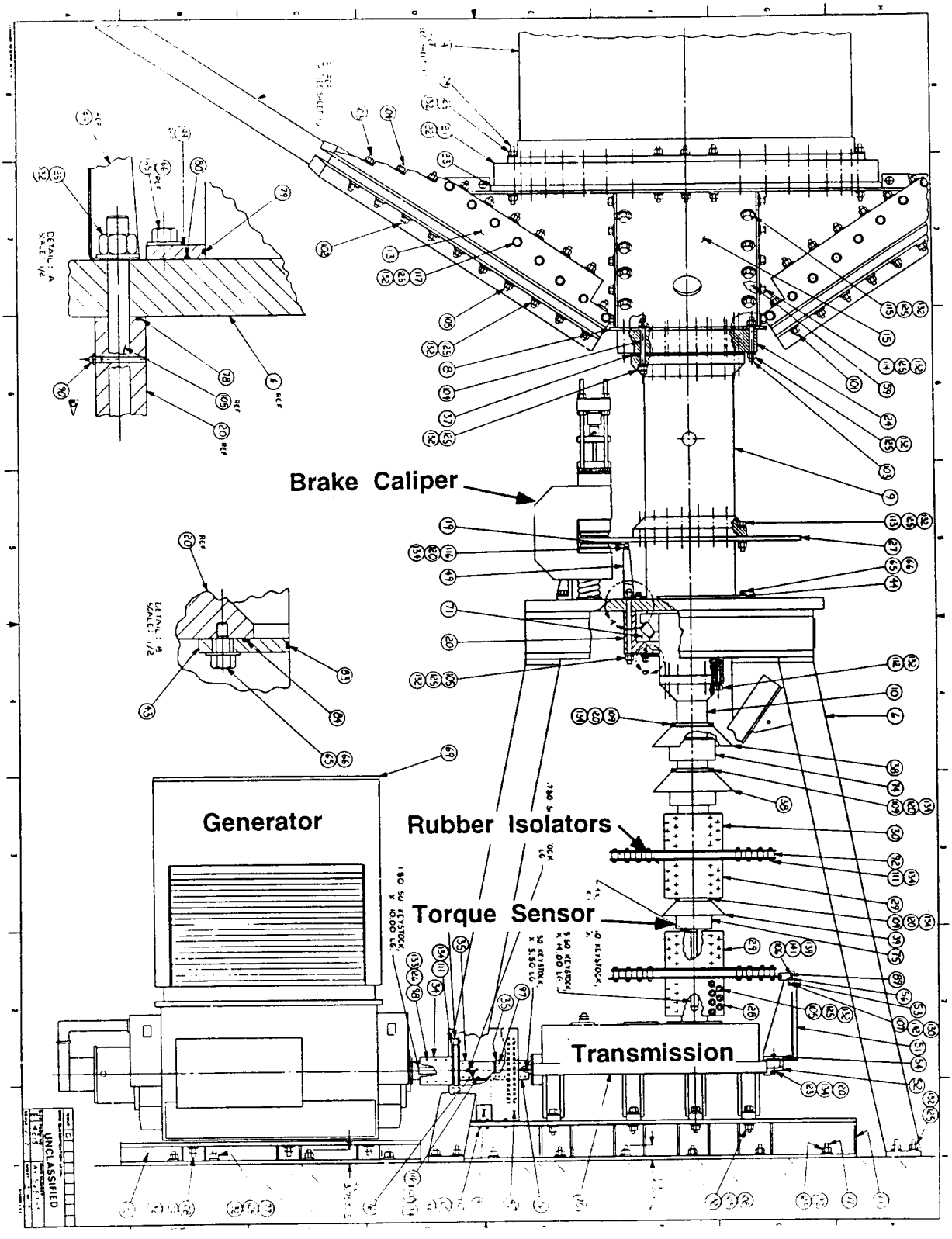

Figure 5.13. Turbine Stand and Drive Train

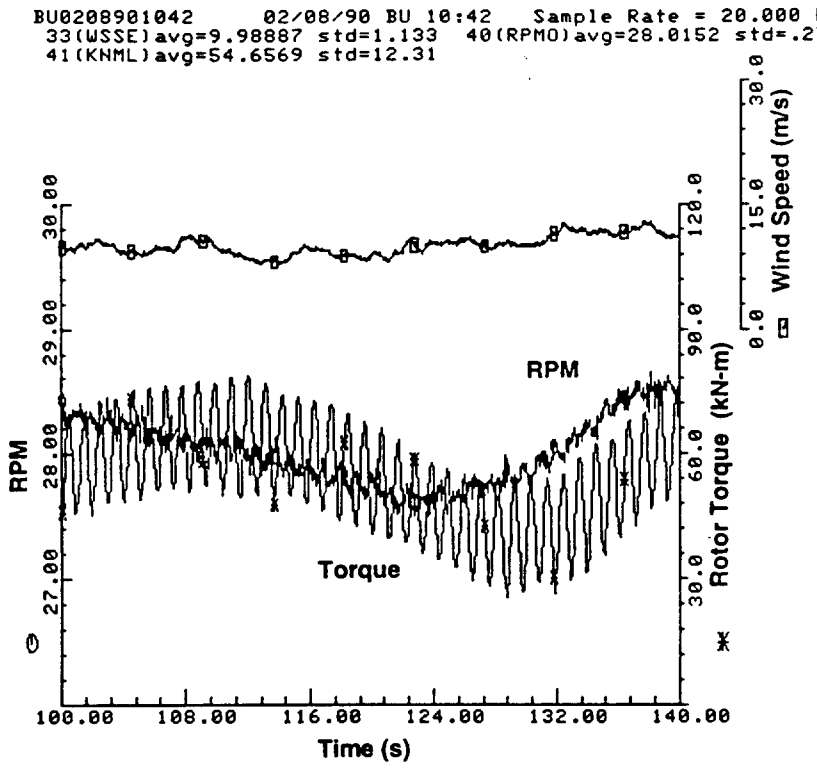

Figure 5.14. Torque Time History at 28 RPM

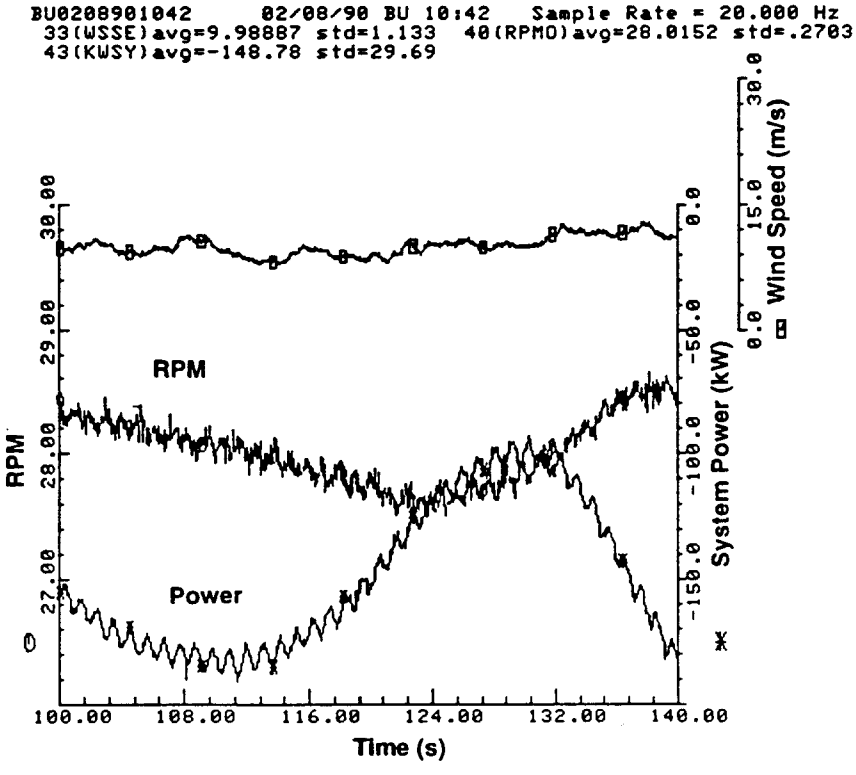

Figure 5.15. System Power Time History at 28 RPM

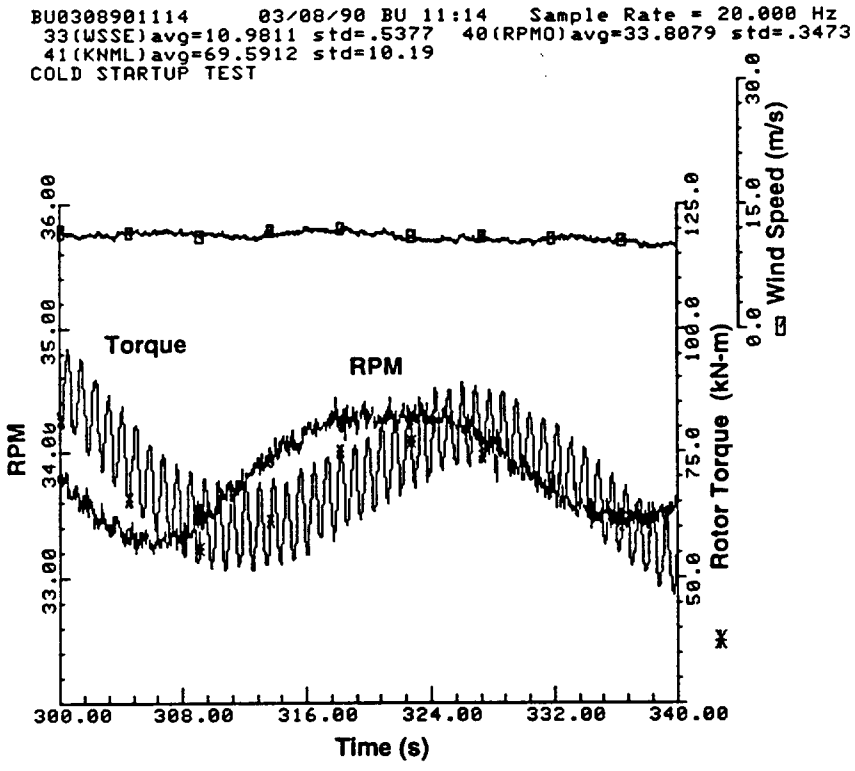

Figure 5.16. Torque Time History at 34 RPM

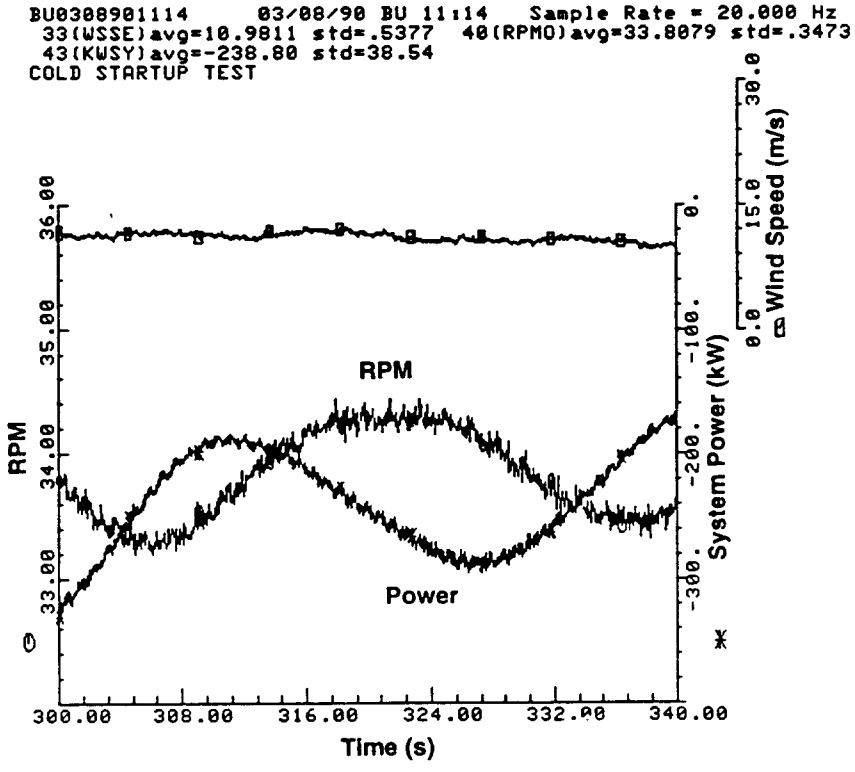

Figure 5.17. System Power Time History at 34 RPM

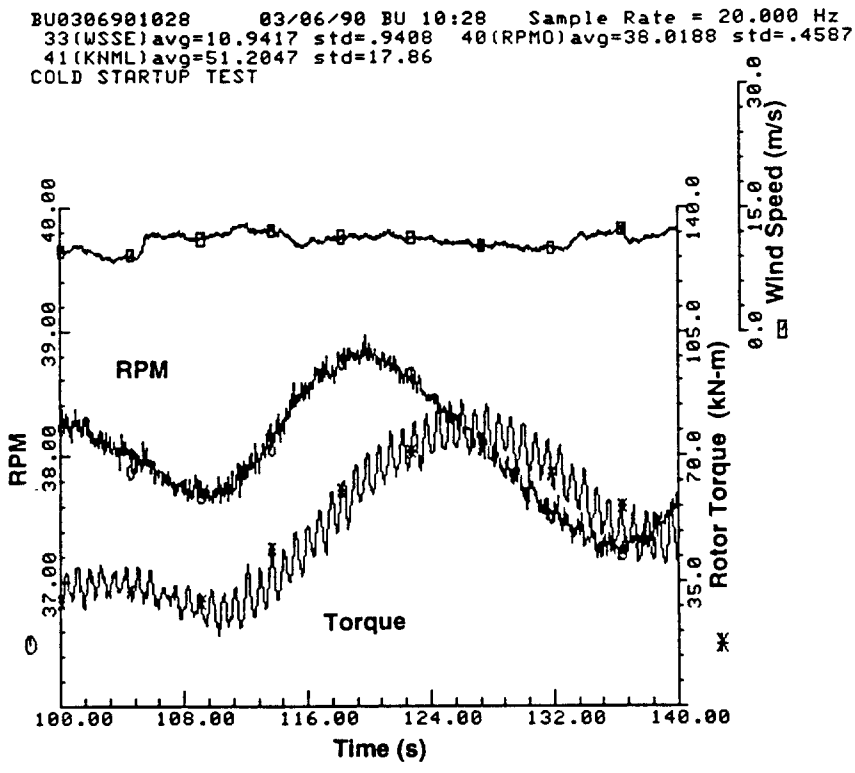

Figure 5.18. Torque Time History at 38 RPM

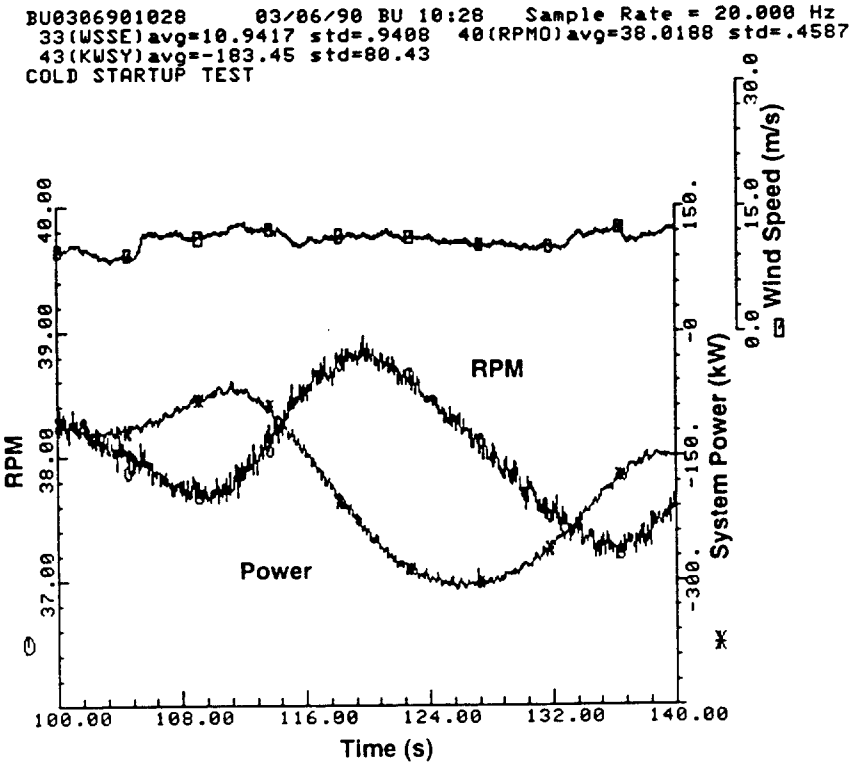

Figure 5.19. System Power Time History at 38 RPM

spectral plots together. This averaging process smooths out the plot by reducing the effects of statistical uncertainty.

Figures 5.20 and 5.21 are averaged spectral plots (10 blocks of data, each 25 seconds long) for an upper root lead-lag and flatwise gauge at 28 rpm in winds that average 10 m/s. RPM variations, which always occur during the Test Bed operation, tend to cause the harmonic responses to be somewhat wider than otherwise would be the case. Both per-rev and natural frequency peaks are observed in these figures. Natural frequency peaks and their magnitude are of interest in understanding the frequency content of the operating stress data, in evaluating the contribution of stochastic effects, and in efforts to improve prediction tools. Figures 5.22 and 5.23 show similar plots for 34 rpm in 9.76 m/s winds and Figs. 5.24 and 5.25 for 38 rpm in 9.4 m/s winds. The lead-lag spectra tend to be dominated by 1 and 3 per-rev and the flatwise by 1 and 2 per-rev responses. However, spikes at several natural frequencies can also be observed.

SUMMARY

Sandia National Laboratories designed and built the 34-meter Test Bed to support our research in structural dynamics, aerodynamics, fatigue, and controls. This data report contains results from testing of the 34-meter Test Bed during the period from initial turbine operation in late 1987 up through mid-1991. A section on aerodynamic performance shows binsed power data at three rotation rates and includes measurements of tare and zero-wind drag, and transmission and generator losses. Comparisons of measured power data to predictions show excellent agreement. Data collected with aerodynamic fairings on the blade-to-blade joints and with bug contamination on the blades show their effects.

Structural response measurements include binsed stresses at three rotation rates, gravity and centrifugal stresses and selected time histories during start-up, braking and normal operation. Measurements of natural frequencies and sample stress spectra are also shown. Again excellent agreement between measured and predicted data is observed.

Based on the data collected up to this time, the Test Bed machine is responding to the wind much as expected. Measured data have been used to perform fatigue analyses of the 34-m Test Bed at different rotation rates (Ashwill, et al. 1990). Future testing will support efforts in understanding aeroelastic effects, studying control algorithms and optimizing the placement of vortex generators.

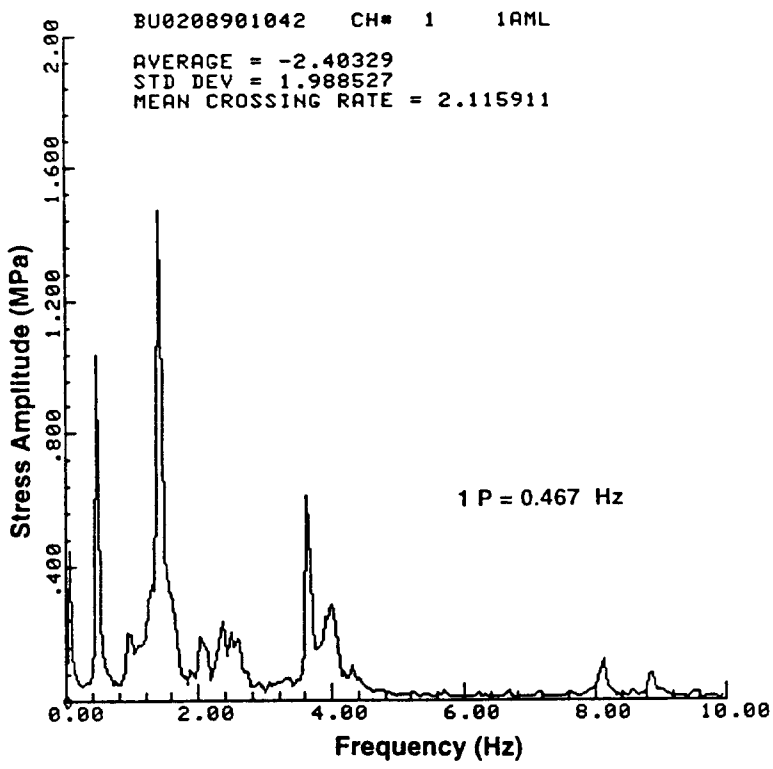

Figure 5.20. Stress Amplitude Spectra for an Upper Root, Trailing Edge Gauge at 28 RPM

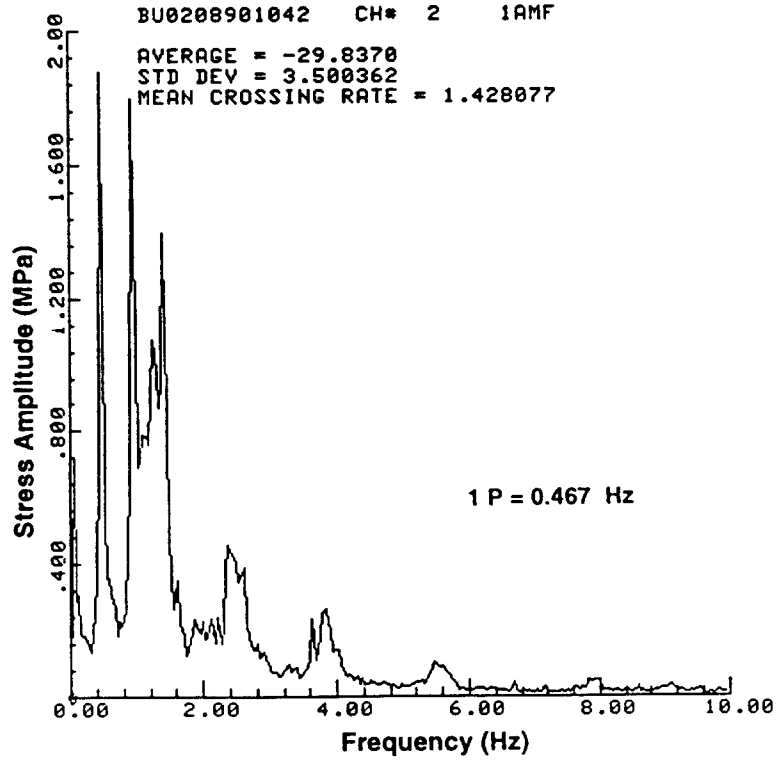

Figure 5.21. Stress Amplitude Spectra for an Upper Root, Flatwise Gauge at 28 RPM

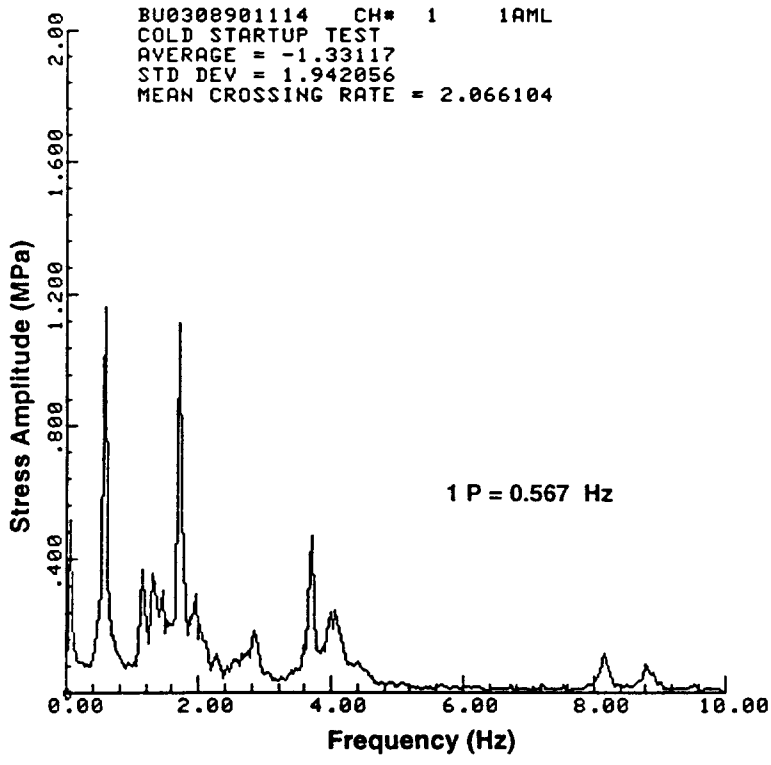

Figure 5.22. Stress Amplitude Spectra for an Upper Root, Trailing Edge Gauge at 34 RPM

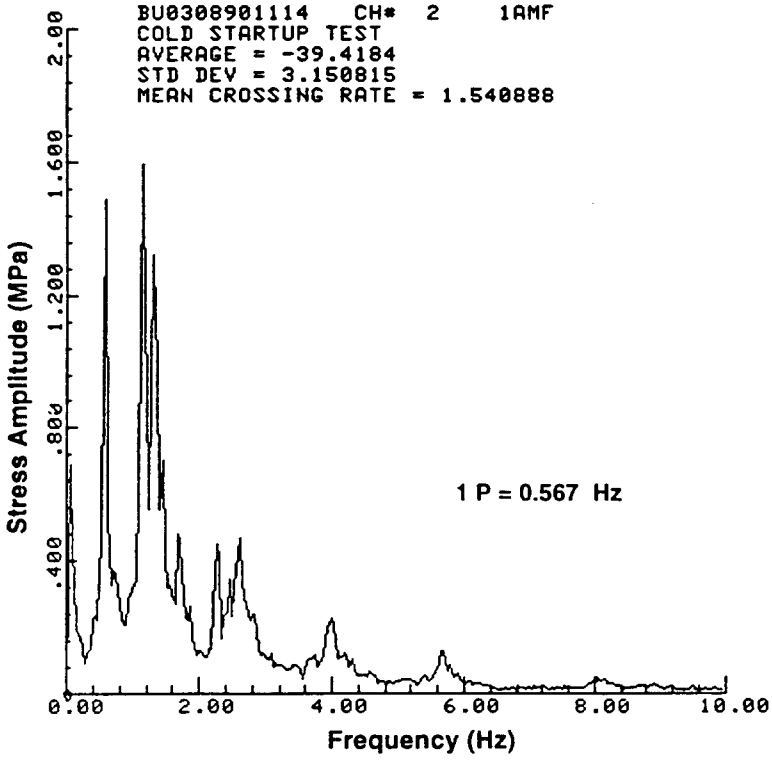

Figure 5.23. Stress Amplitude Spectra for an Upper Root, Flatwise Gauge at 34 RPM

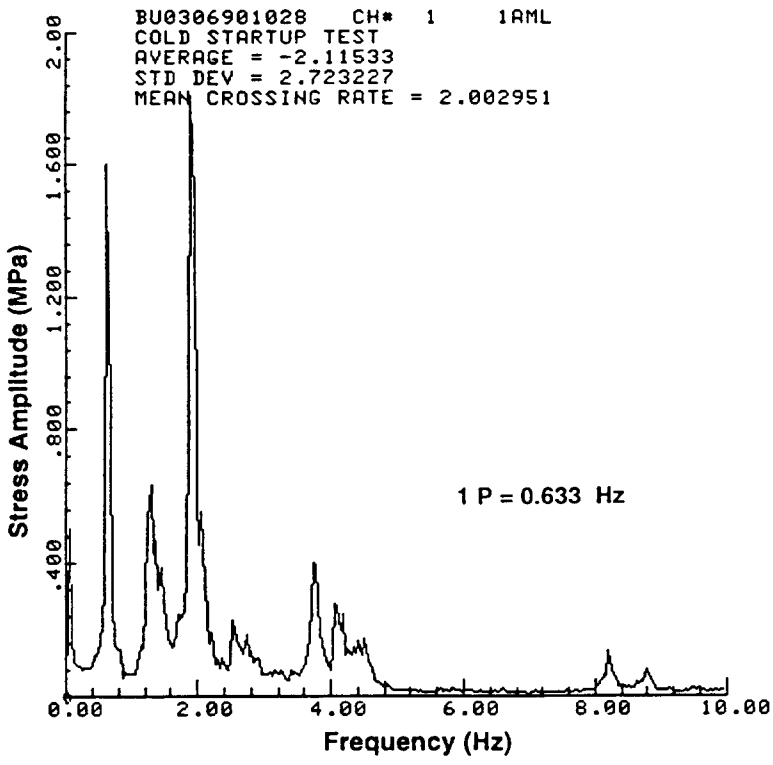

Figure 5.24. Stress Amplitude Spectra for an Upper Root, Trailing Edge Gauge at 38 RPM

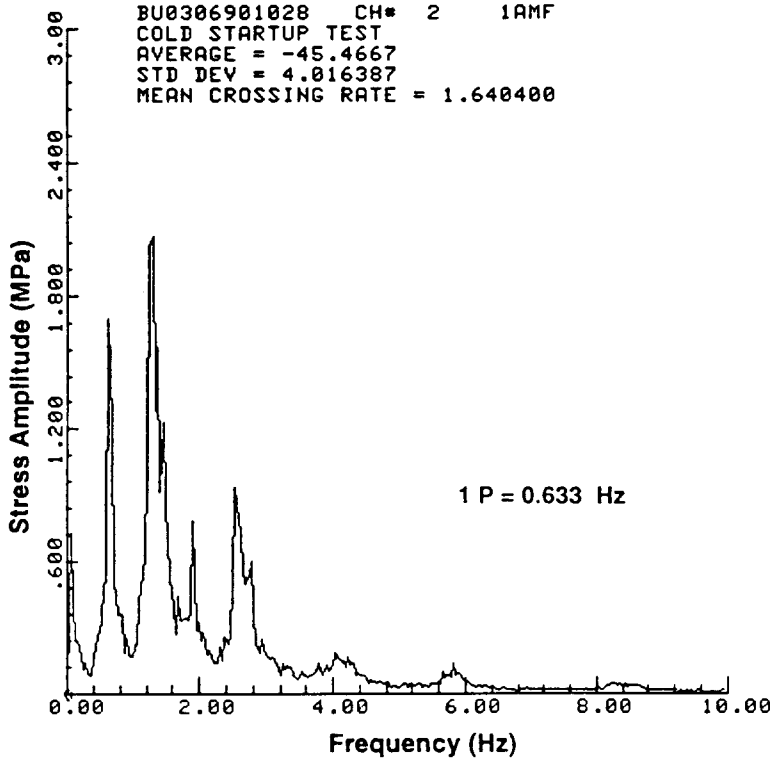

Figure 5.25. Stress Amplitude Spectra for an Upper Root, Flatwise Gauge at 38 RPM

ACKNOWLEDGEMENTS

The author would like to acknowledge the contributions of several members of the Test Bed team. Any new machine has difficulties in the start-up process, but our problems were minimized due to the efforts and foresight of the Test Bed operators, Bill Stephenson and Ron Davis, USDA. Mark Rumsey and Dan Burwinkle, NMERI, have supplied valuable support in the data acquisition and analysis software and hardware. Mark Ralph designed and tested the control and variable-speed power systems. Herb Sutherland performed fatigue analyses and implemented the rotor instrumentation, which has provided consistent data with few losses of gauges. Dale Berg leads the efforts in aerodynamic testing, design and analysis. Paul Veers has contributed a significant amount of analysis in the structural dynamics and fatigue areas. Tom Carne directed the operations in modal testing and supports the work in structural analysis. And finally, Henry Dodd and R. Nolan Clark, USDA, continue to provide strong leadership in the Test Bed program.

REFERENCES

Akins, R.E., 1978, *Performance Evaluation of Wind Energy Conversion Systems Using the Method of Bins - Current Status*, SAND77-1375, Sandia National Laboratories, Albuquerque, NM.

Ashwill, T.D., 1990, *Initial Structural Response Measurements and Model Validation for the Sandia 34-Meter VAWT Test Bed*, SAND88-0633, Sandia National Laboratories, Albuquerque, NM.

Ashwill, T.D. and T.M. Leonard, 1986, *Developments in Blade Shape Design for a Darrieus Vertical Axis Wind Turbine*, SAND86-1085, Sandia National Laboratories, Albuquerque, NM.

Ashwill, T.D., 1987, "Structural Design and Fabrication of the Sandia 34-Meter Vertical Axis Wind Turbine," *Proceedings of the 1987 ASME-JSME Solar Energy Conference*, Honolulu, HI.

Ashwill, T.D. and P.S. Veers, 1990, "Structural Response Measurements and Predictions for the Sandia 34-Meter Test Bed," *Proceedings of the Ninth ASME Wind Energy Symposium*, New Orleans, Louisiana.

Ashwill, T.D., H.J. Sutherland, and P.S. Veers, 1990, "Fatigue Analysis of the Sandia 34-Meter Vertical Axis Wind Turbine," *Proceedings of the Ninth ASME Wind Energy Symposium*, New Orleans, Louisiana.

Berg, D.E., M. Rumsey, L. Gallo, and D. Burwinkle, 1988, "Data Acquisition and Analysis System for the Sandia 34-Meter Vertical Axis Wind Turbine," *Proceedings of the Seventh ASME Wind Energy Symposium*, New Orleans, La.

Berg, D.E., P.C. Klimas, and W.A. Stephenson, 1990, "Aerodynamic Design and Initial Performance Measurements for the Sandia 34-m Diameter Vertical Axis Wind Turbine," *Proceedings of the Ninth ASME Wind Energy Symposium*, New Orleans, LA.

Carne, T.G., J.P. Lauffer, A.J. Gomez, and T.D. Ashwill, 1989, "Model Validation of the Sandia 34-Meter Test Bed Turbine Using Substructure Modal-Testing," *Proceedings of the Eighth ASME Wind Energy Symposium*, Houston, Texas.

Dodd, H.M., T.D. Ashwill, D.E. Berg, M.E. Ralph, W.A. Stephenson, and P.S. Veers, 1989, "Test Results and Status of the DOE/Sandia 34-M VAWT Test Bed," *Proceedings of the Canadian Wind Energy Conference '89*, Charlottetown, P.E.I.

Klimas, P.C., 1984, *Tailored Airfoils for Vertical Axis Wind Turbines*, SAND84-1062, Sandia National Laboratories, Albuquerque, NM.

Lobitz, D.W., and W.N Sullivan, 1984, *Comparison of Finite Element Predictions and Experimental Data for the Forced Response of the DOE 100 kW Vertical Axis Wind Turbine*, SAND82-2534, Sandia National Laboratories, Albuquerque, NM.

Malcolm, D.R., 1988, *A Model for the Response of Vertical Axis Wind Turbines to Turbulent Flow Parts 1 and 2*, SAND88-7021, Indal Technologies, Mississauga, Ontario, Canada.

Malcolm, D.R., 1990, *Vertical Axis Wind Turbine Turbulent Response Model*, SAND89-7042, Indal Technologies, Mississauga, Ontario, Canada.

Paraschivoiu, I., 1981, "Double-Multiple Streamtube Model for Darrieus Wind Turbine," *Proceedings of the Second DOE/NASA Wind Turbine Dynamics Workshop*, Cleveland, OH.

Ralph, M.E., 1990, *Data Logger for the 34-m Vertical Axis Wind Turbine Test Bed*, SAND90-0116, Sandia National Laboratories, Albuquerque, NM.

Reuter, R.C., and M.H. Worstell, 1978, *Torque Ripple in a Vertical Axis Wind Turbine*, SAND78-0577, Sandia National Laboratories, Albuquerque, NM.

Stephenson, W.A., 1990, Tare Tests Memorandum, Sandia National Laboratories, Albuquerque, NM.

Stephenson, W.A., 1986, *Test Plan for the 34 Meter Vertical Axis Wind Turbine Test Bed Located at Bushland, Texas*, SAND86-1623, Sandia National Laboratories, Albuquerque, NM.

Sutherland, H.J., 1988, *Strain Gauge Validation Experiments for the Sandia 34-Meter VAWT Test Bed*, SAND88-1807, Sandia National Laboratories, Albuquerque, NM.

Sutherland, H.J. and W.A. Stephenson, 1988, *Rotor Instrumentation Circuits for the Sandia 34-Meter Vertical Axis Wind Turbine*, SAND88-1144, Sandia National Laboratories, Albuquerque, NM.

APPENDIX A

RMV Stresses at 28 RPM

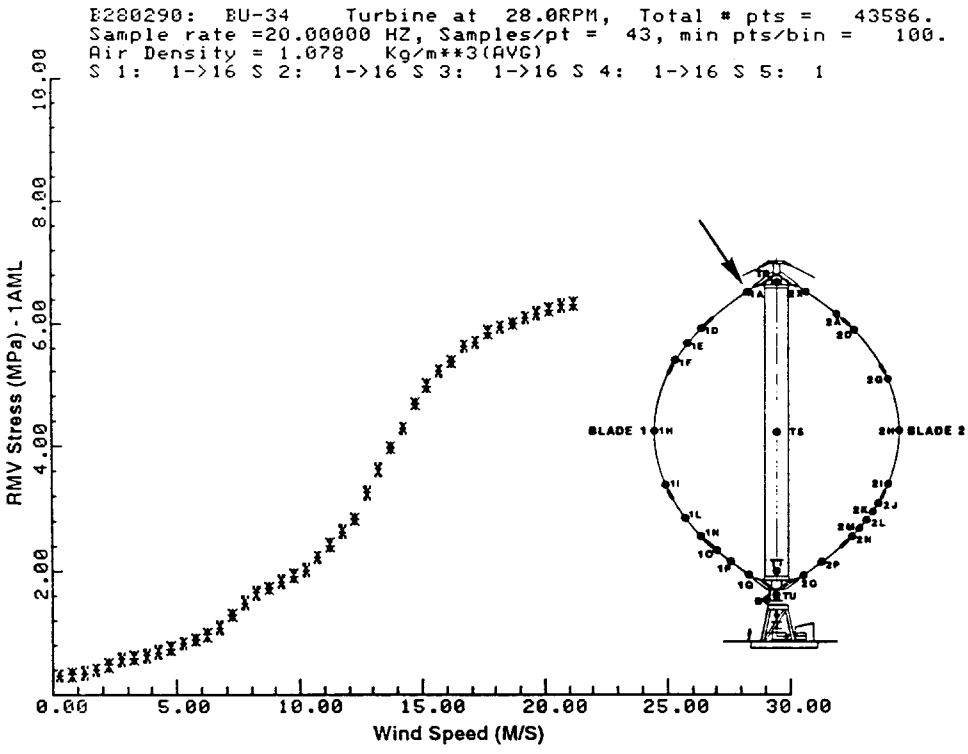

Figure A-1. RMV Stress vs. Wind Speed at 28 RPM - 1AML

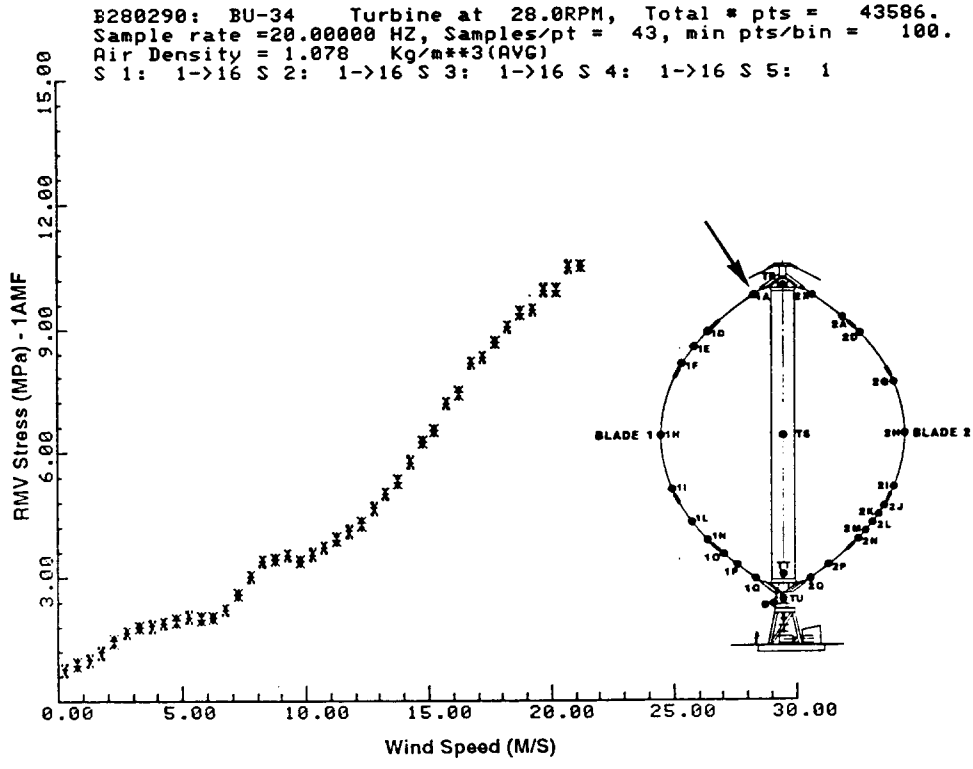

Figure A-2. RMV Stress vs. Wind Speed at 28 RPM - 1AMF

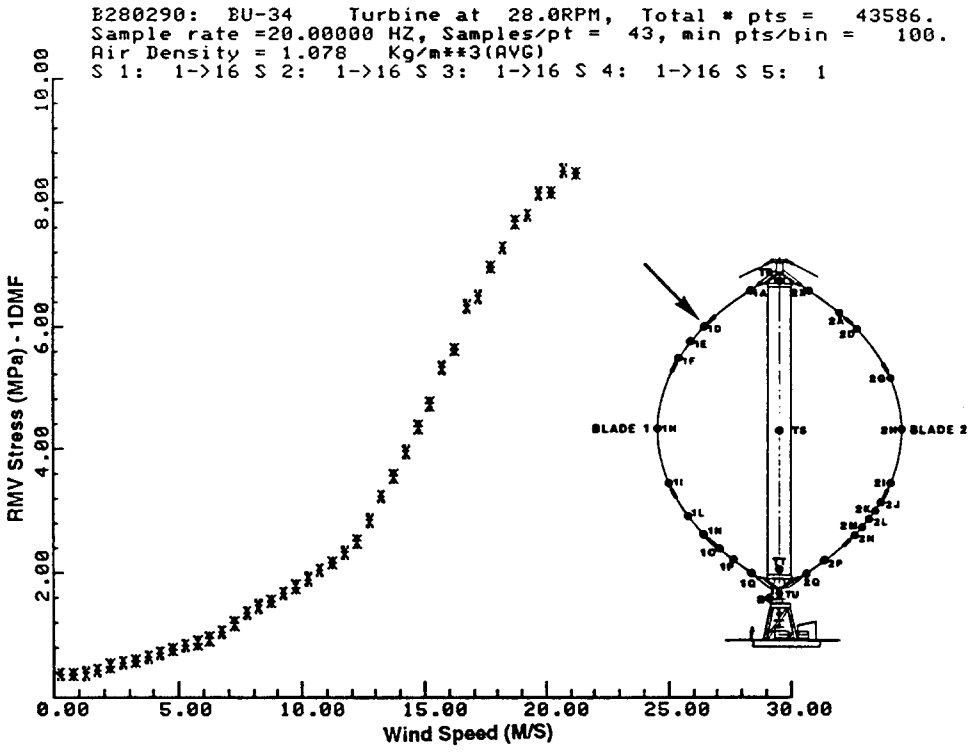

Figure A-3. RMV Stress vs. Wind Speed at 28 RPM - 1DMF

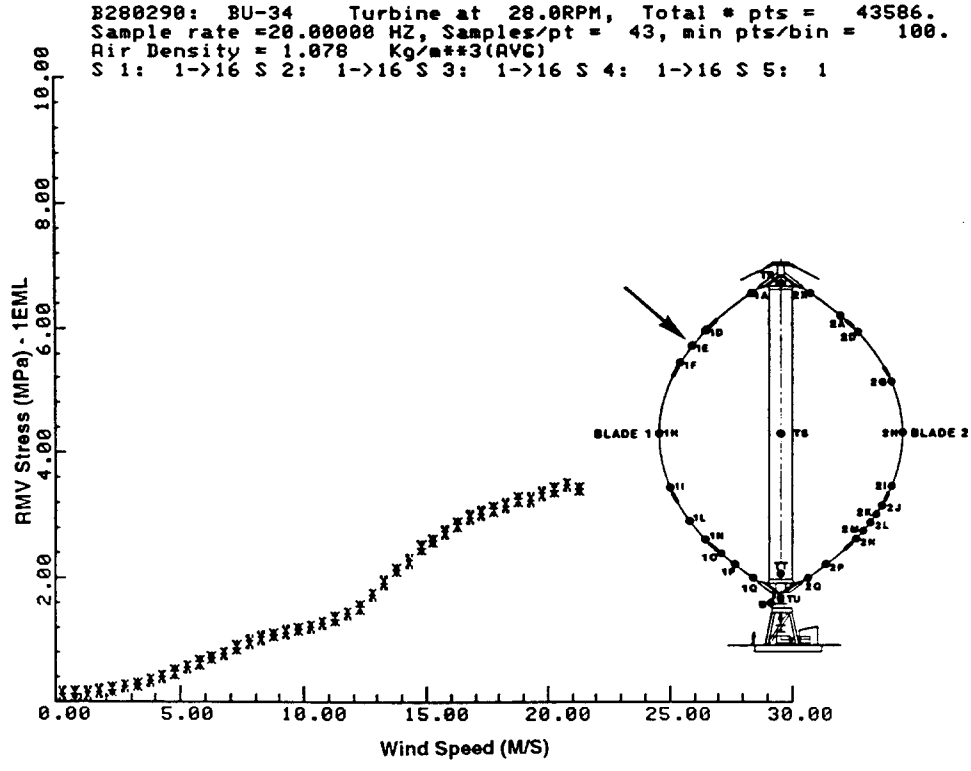

Figure A-4. RMV Stress vs. Wind Speed at 28 RPM - 1EML

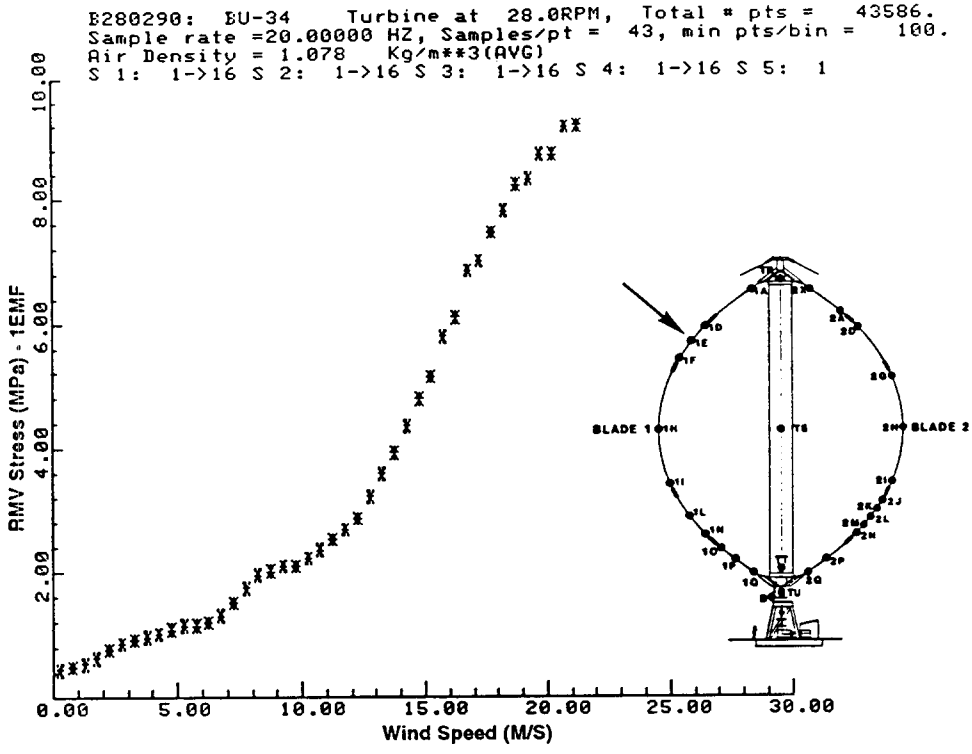

Figure A-5. RMV Stress vs. Wind Speed at 28 RPM - 1EMF

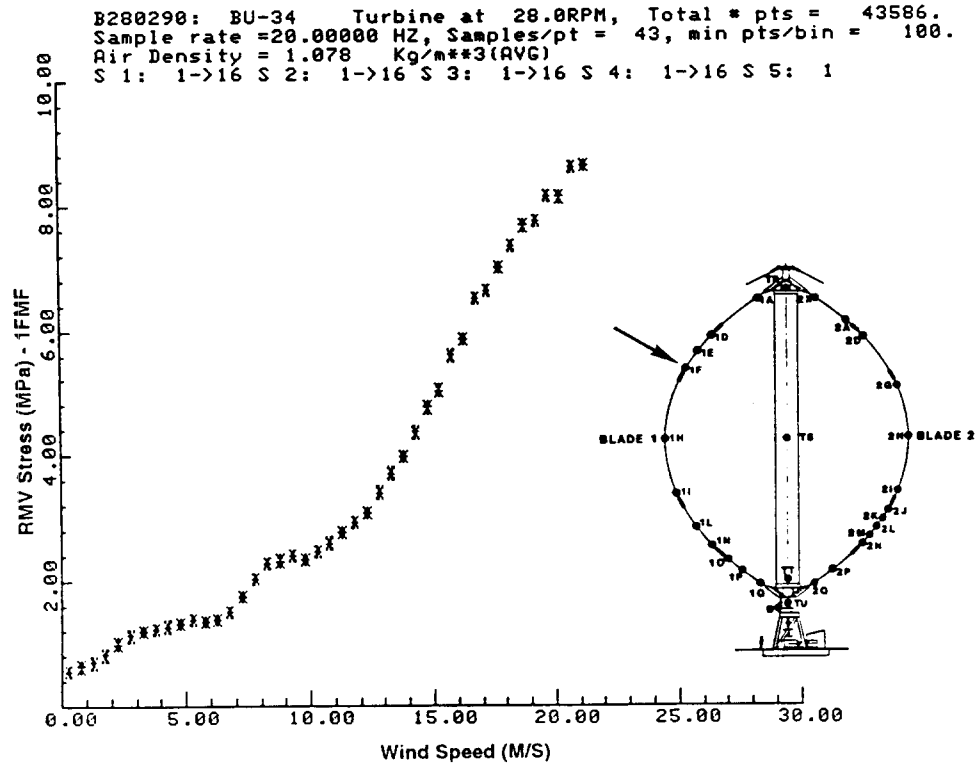

Figure A-6. RMV Stress vs. Wind Speed at 28 RPM - 1FMF

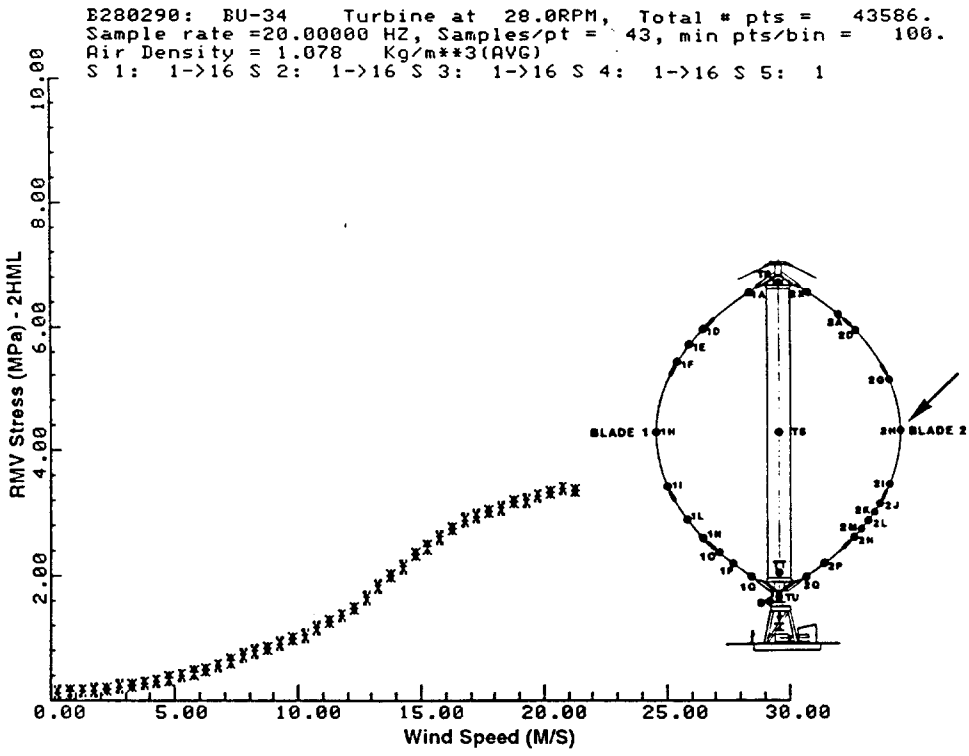

Figure A-7. RMV Stress vs. Wind Speed at 28 RPM - 2HML

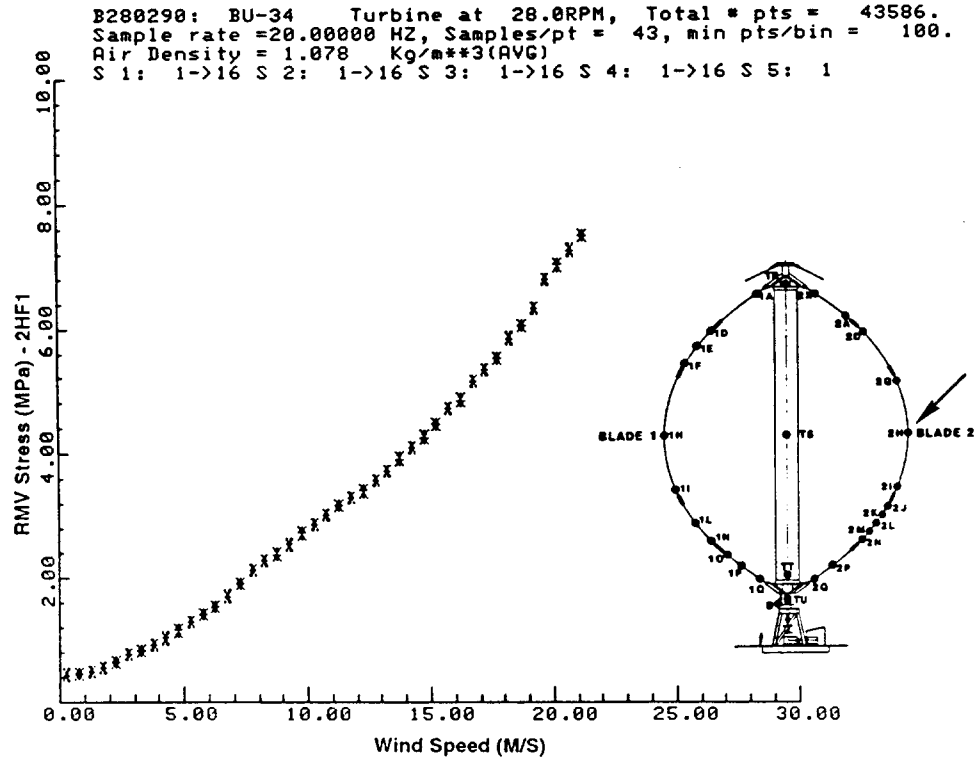

Figure A-8. RMV Stress vs. Wind Speed at 28 RPM - 2HF1

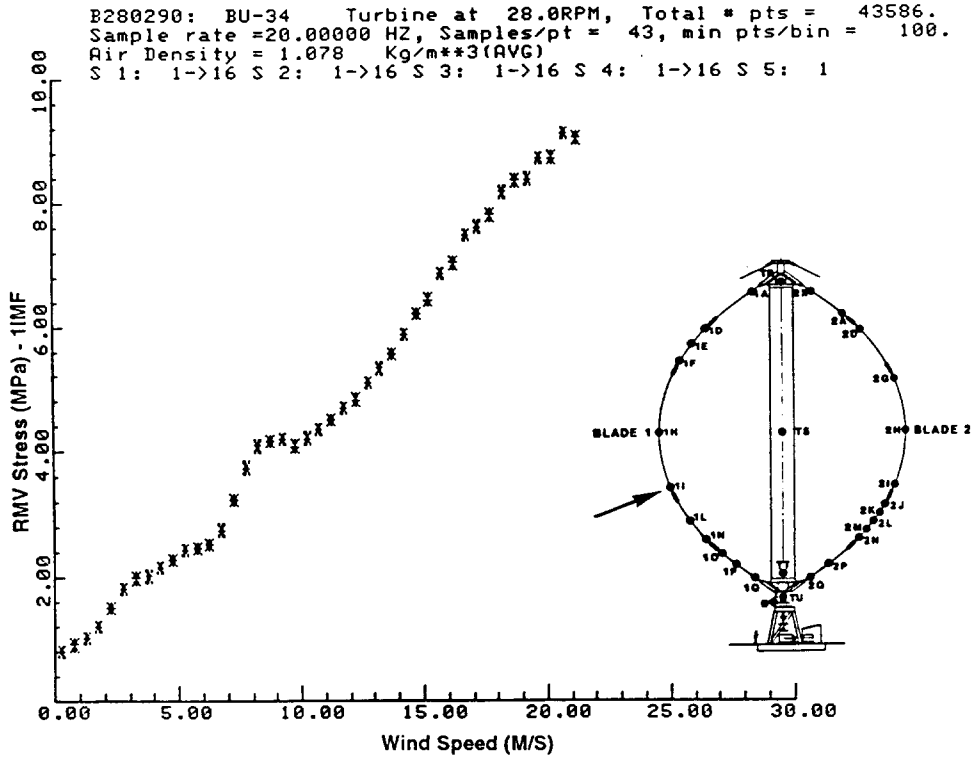

Figure A-9. RMV Stress vs. Wind Speed at 28 RPM - 1IMF

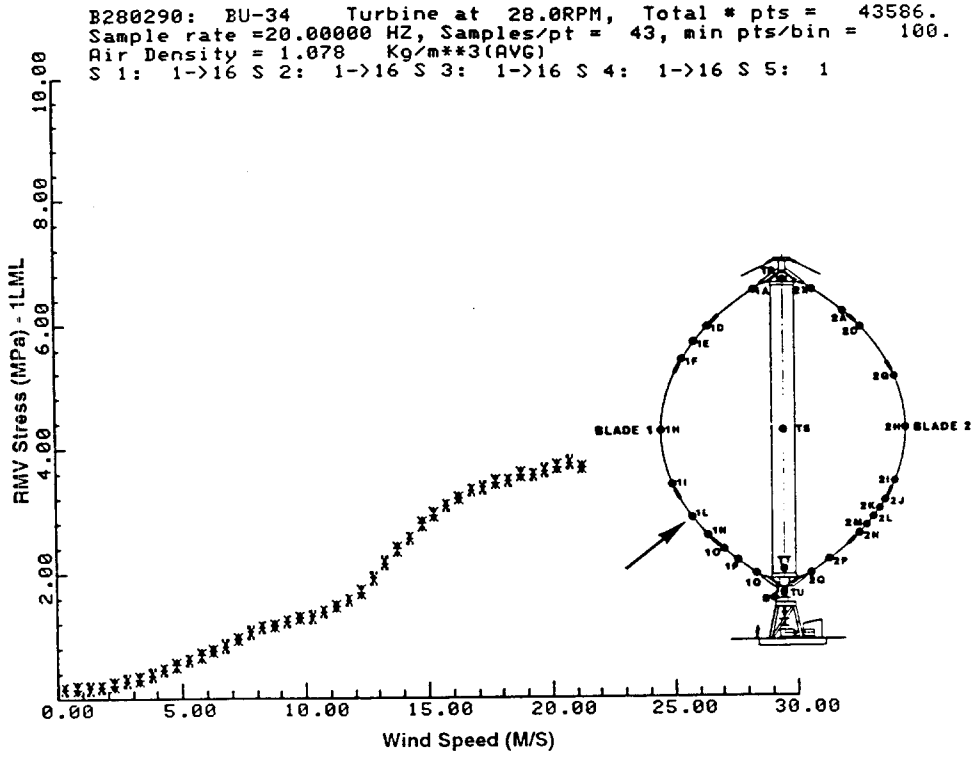

Figure A-10. RMV Stress vs. Wind Speed at 28 RPM - 1LML

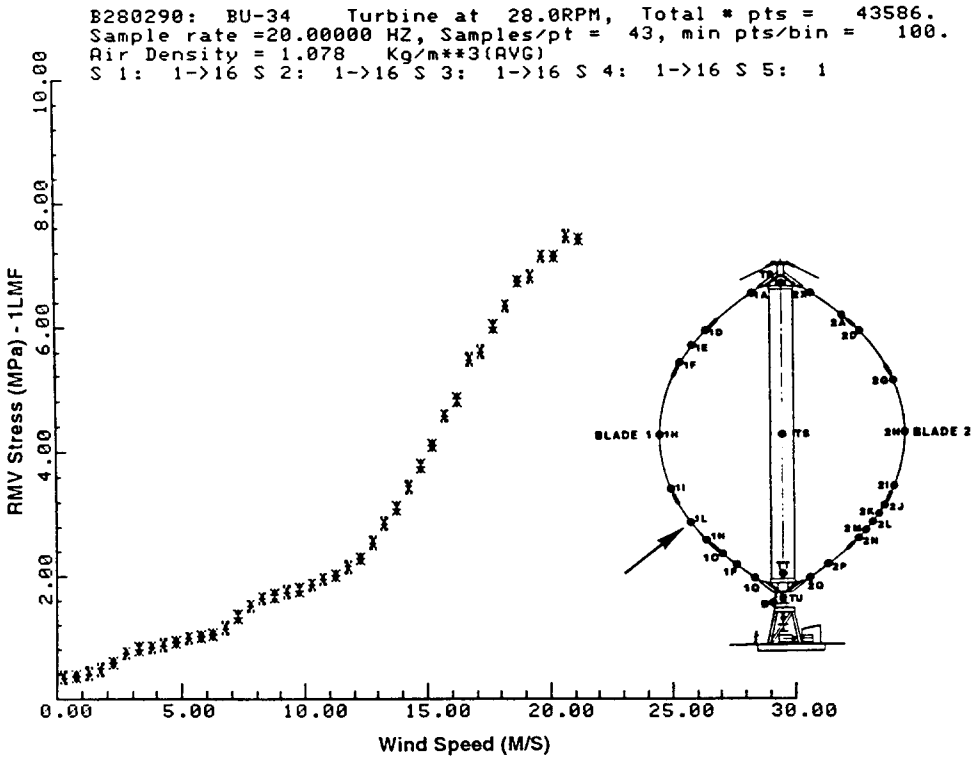

Figure A-11. RMV Stress vs. Wind Speed at 28 RPM - 1LMF

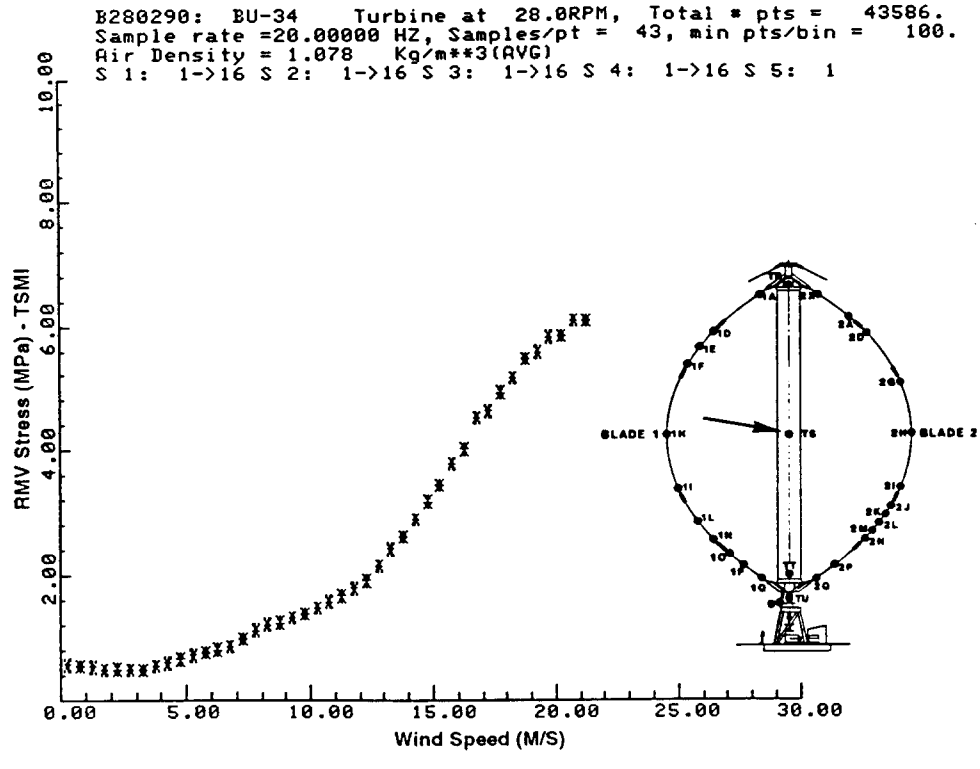

Figure A-12. RMV Stress vs. Wind Speed at 28 RPM - TSMI

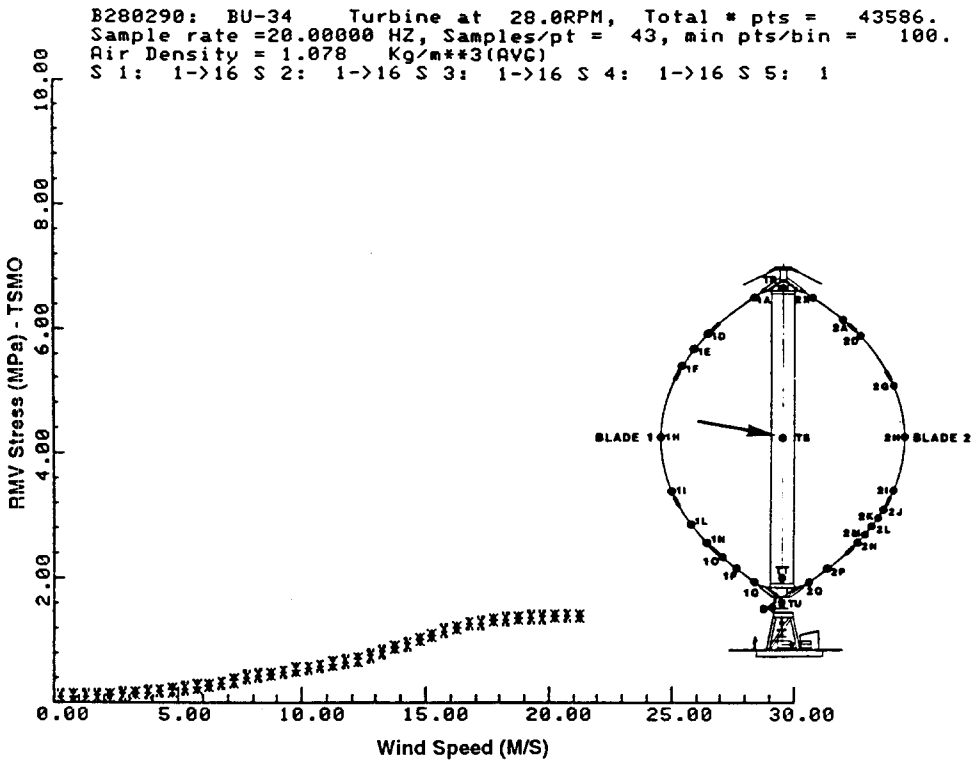

Figure A-13. RMV Stress vs. Wind Speed at 28 RPM - TSMO

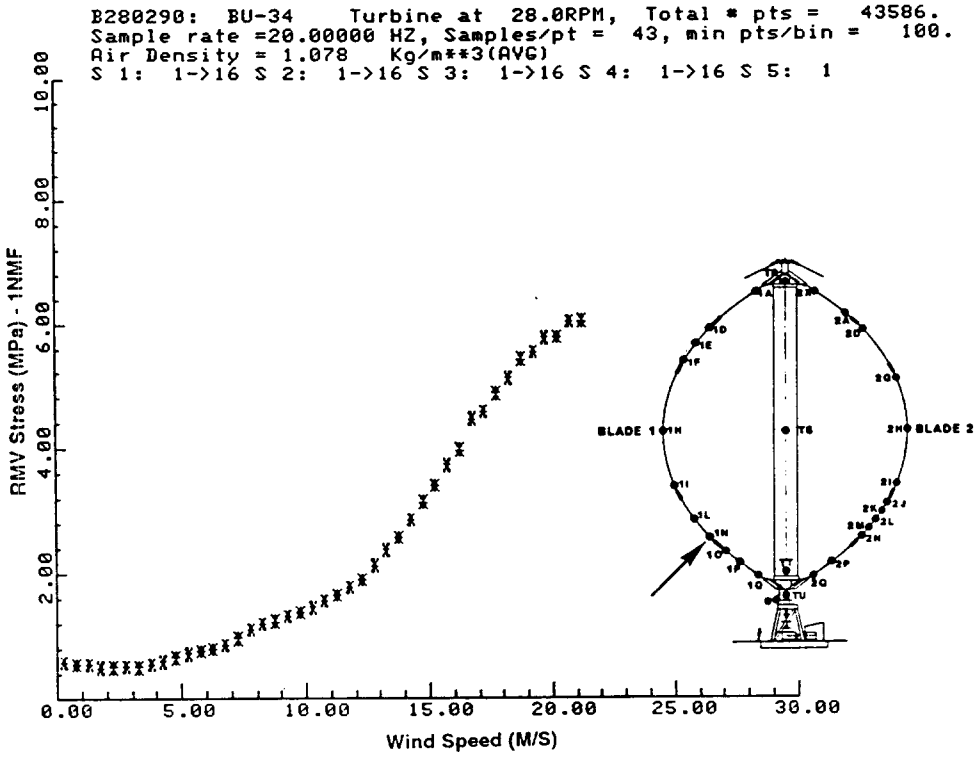

Figure A-14. RMV Stress vs. Wind Speed at 28 RPM - 1NMF

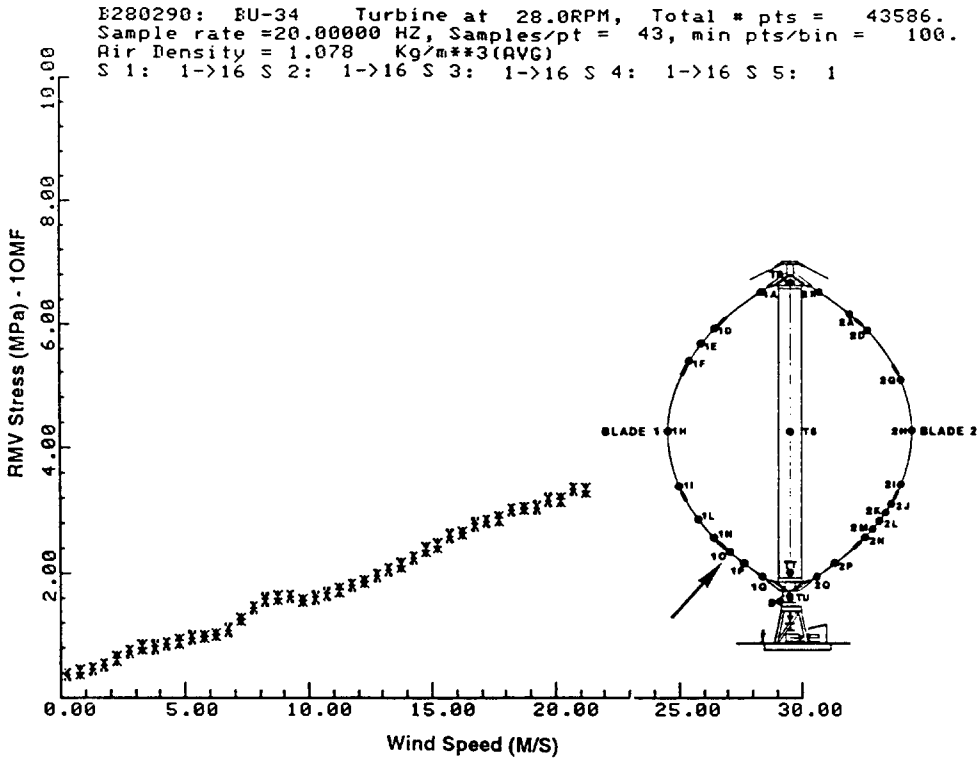

Figure A-15. RMV Stress vs. Wind Speed at 28 RPM - 1OMF

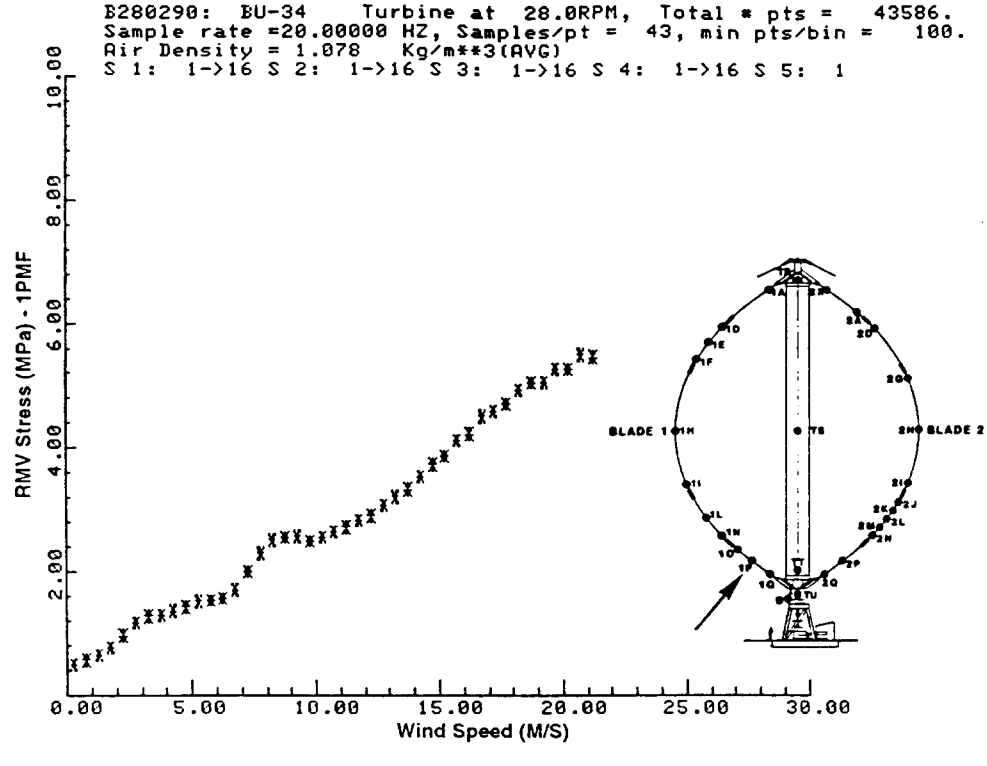

Figure A-16. RMV Stress vs. Wind Speed at 28 RPM - 1PMF

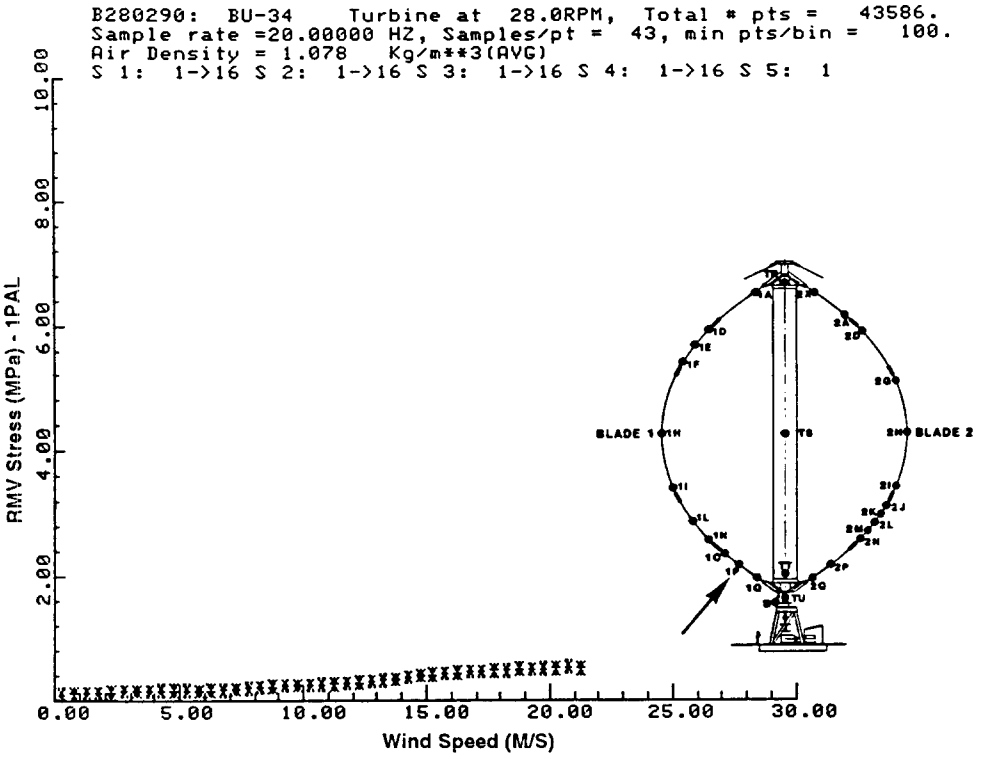

Figure A-17. RMV Stress vs. Wind Speed at 28 RPM - 1PAL

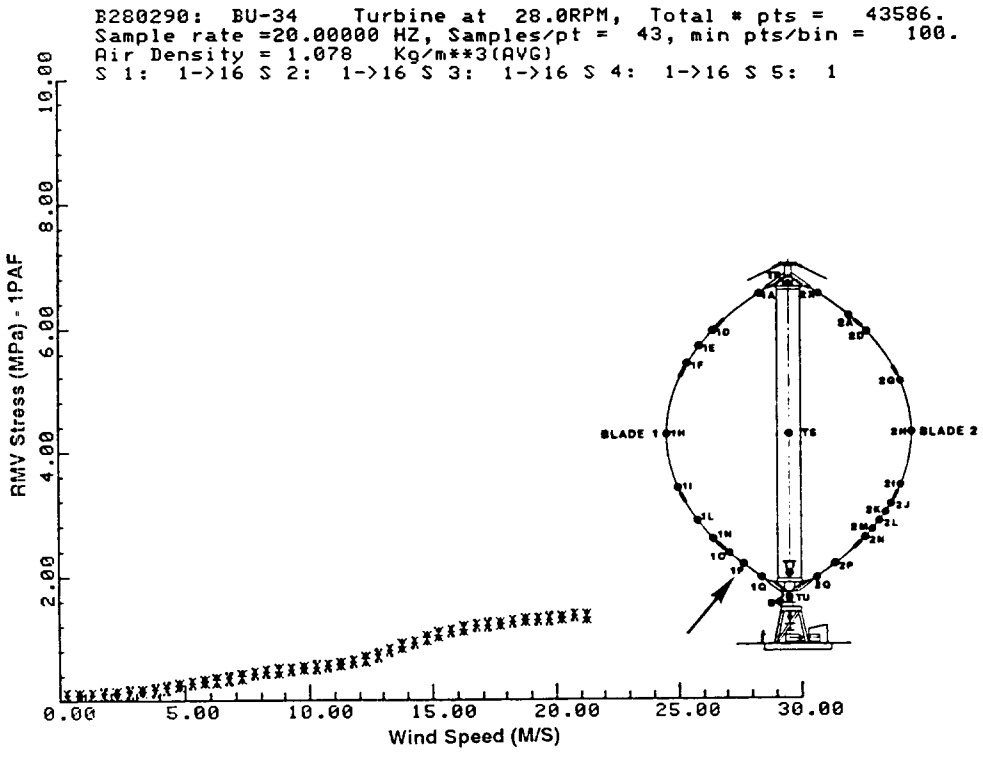

Figure A-18. RMV Stress vs. Wind Speed at 28 RPM - 1PAF

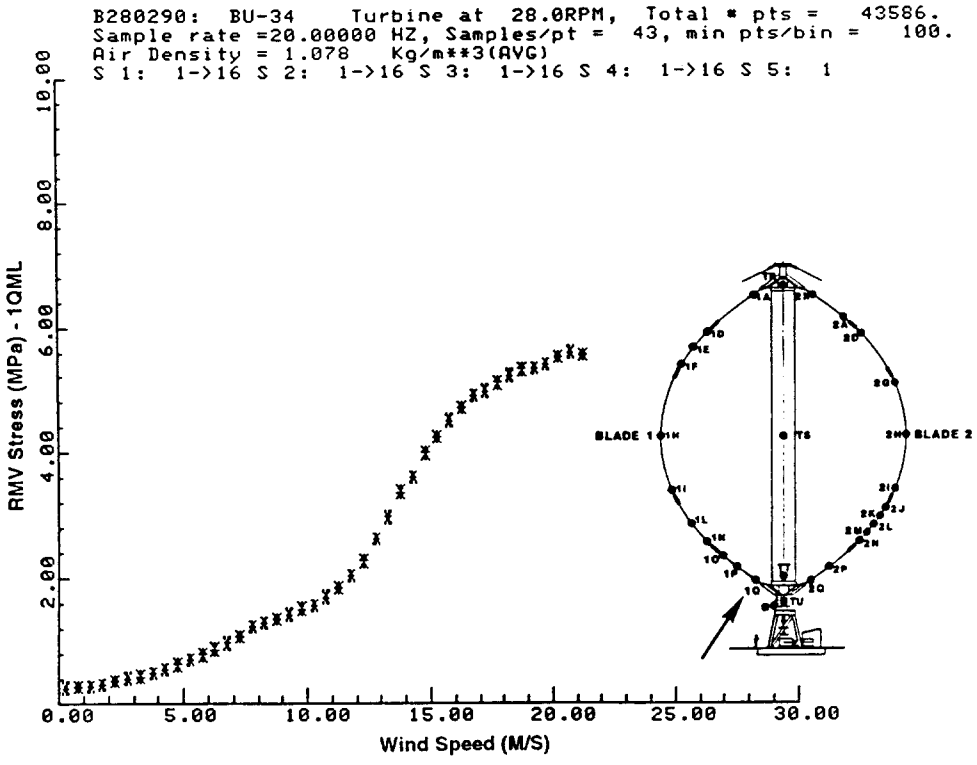

Figure A-19. RMV Stress vs. Wind Speed at 28 RPM - 1QML

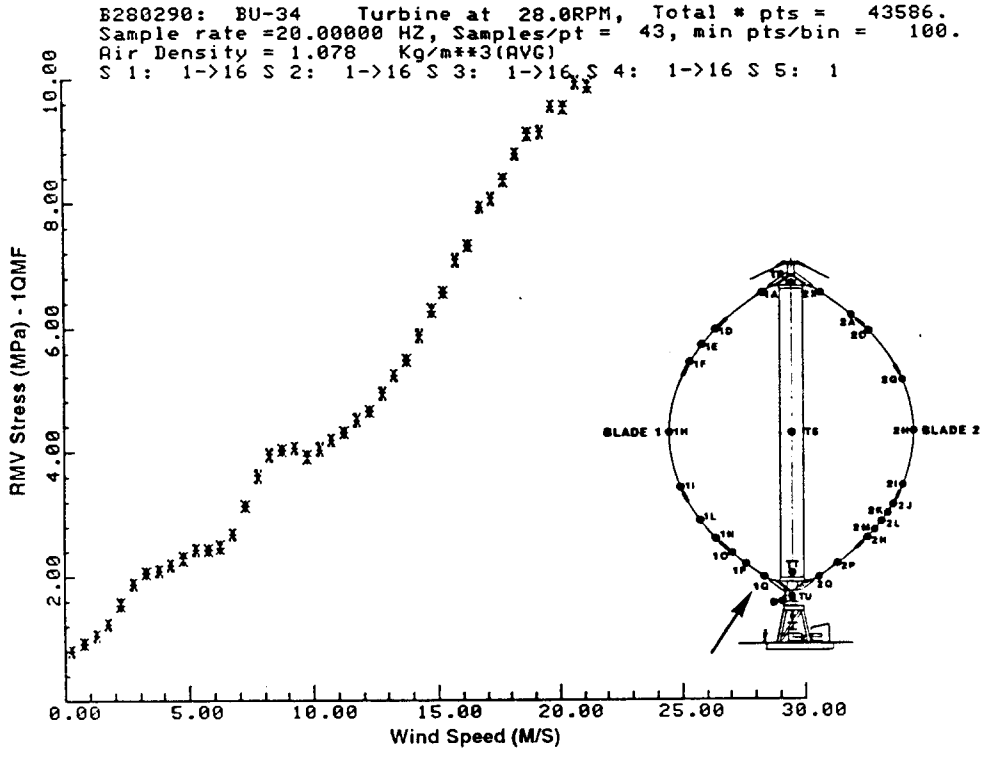

Figure A-20. RMV Stress vs. Wind Speed at 28 RPM - 1QMF

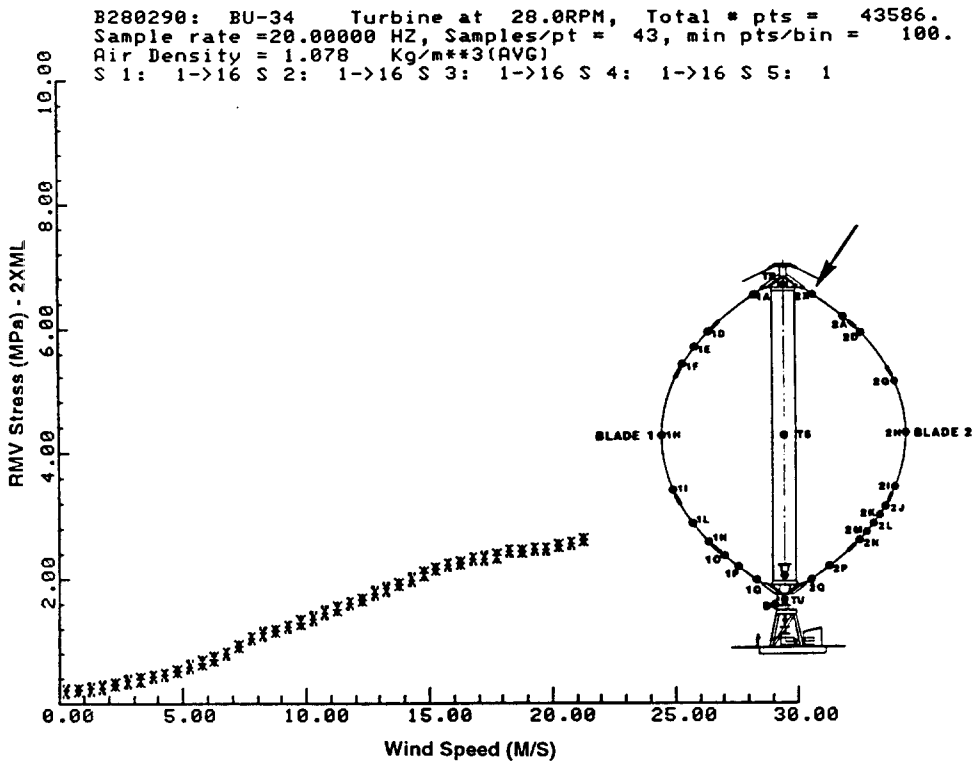

Figure A-21. RMV Stress vs. Wind Speed at 28 RPM - 2XML

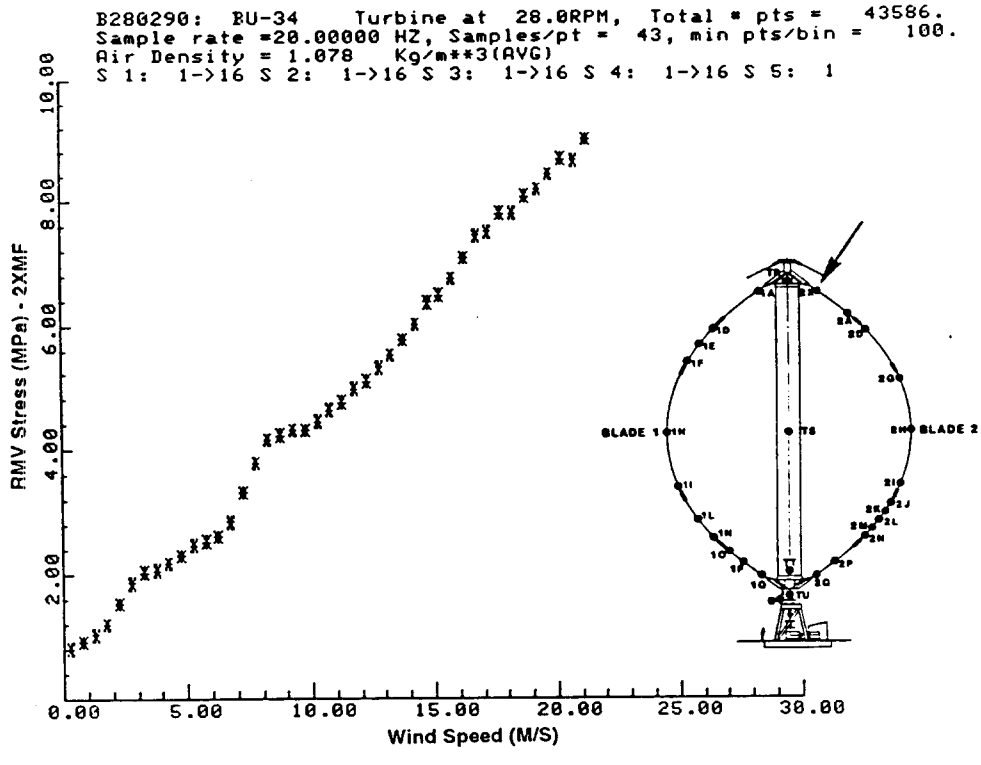

Figure A-22. RMV Stress vs. Wind Speed at 28 RPM - 2XMF

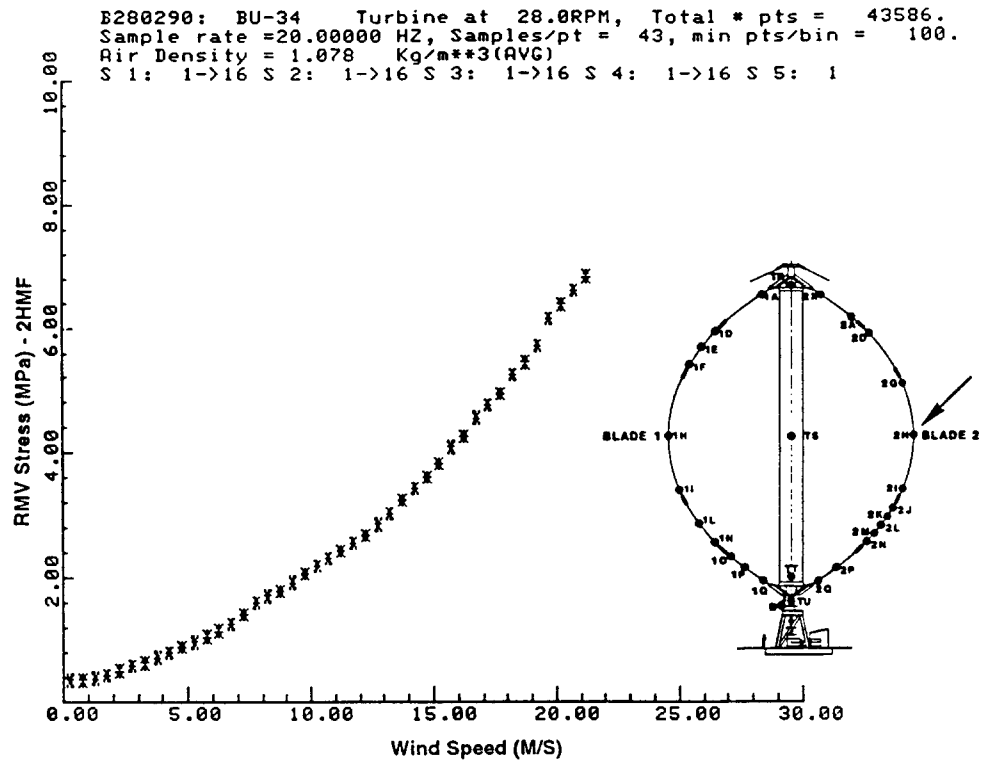

Figure A-23. RMV Stress vs. Wind Speed at 28 RPM - 2HMF

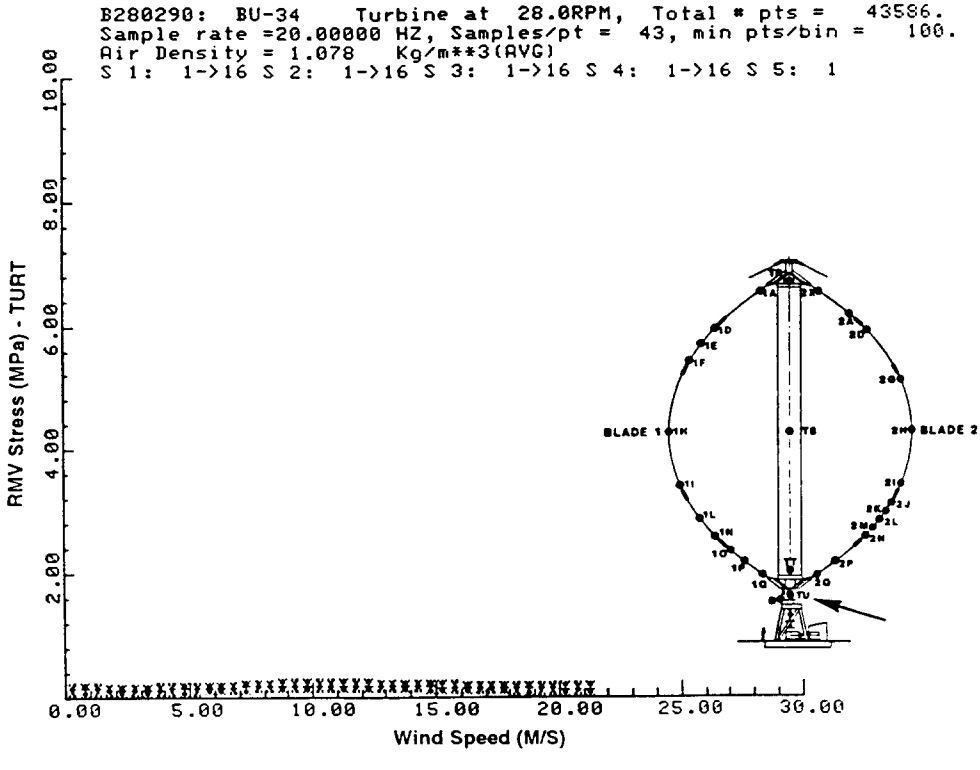

Figure A-24. RMV Stress vs. Wind Speed at 28 RPM - TURT

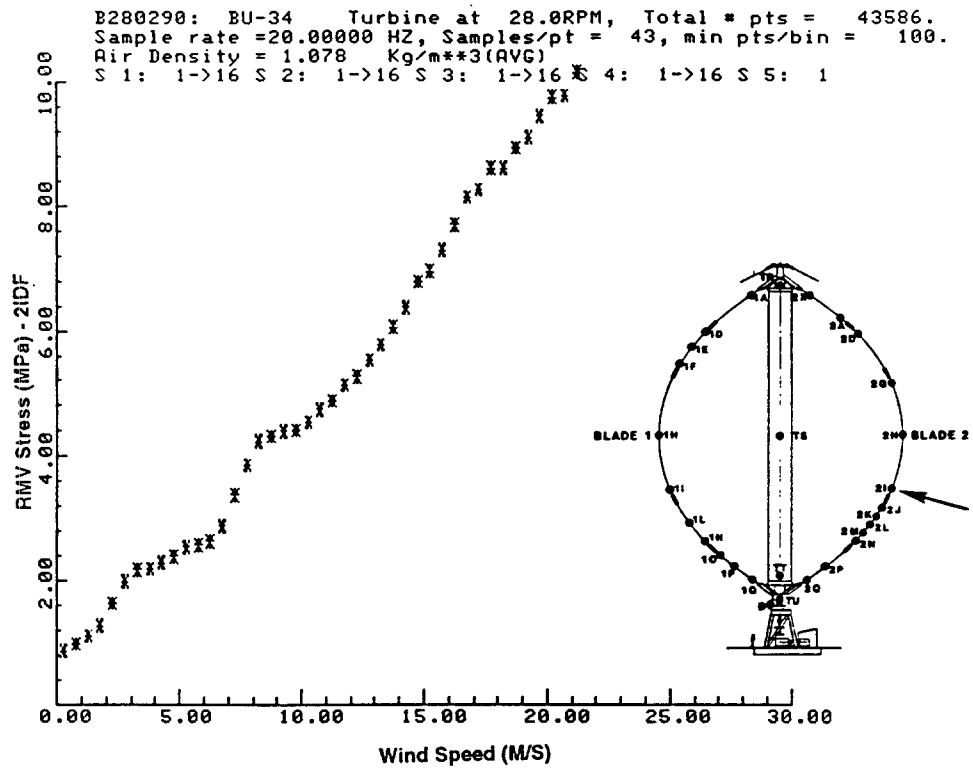

Figure A-25. RMV Stress vs. Wind Speed at 28 RPM - 2IDF

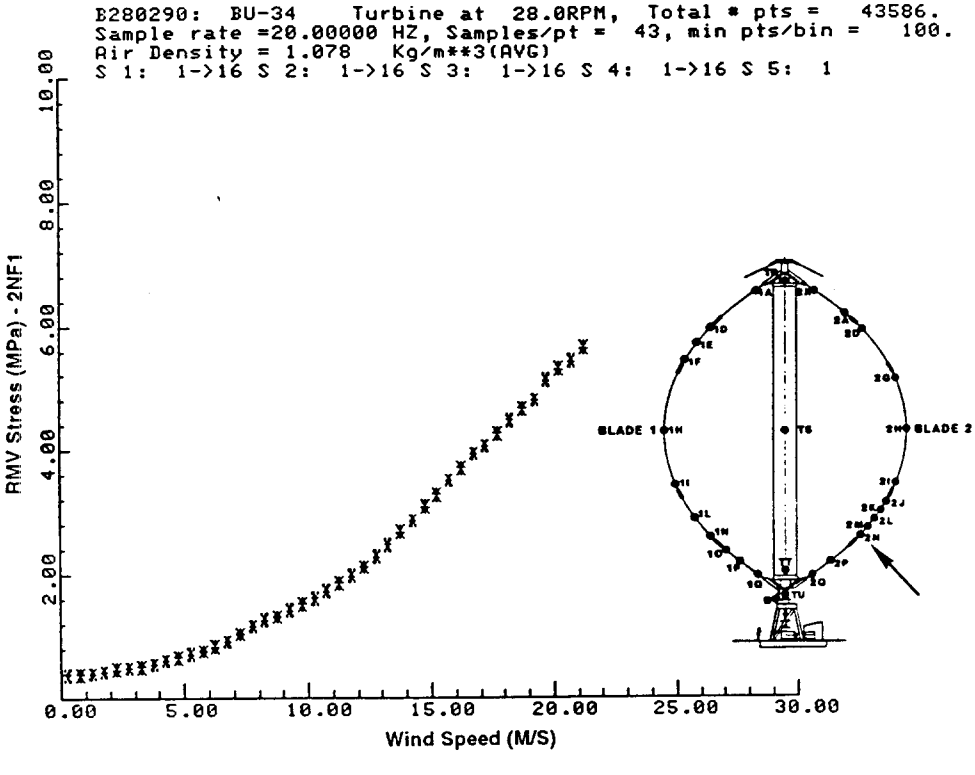

Figure A-26. RMV Stress vs. Wind Speed at 28 RPM - 2NF1

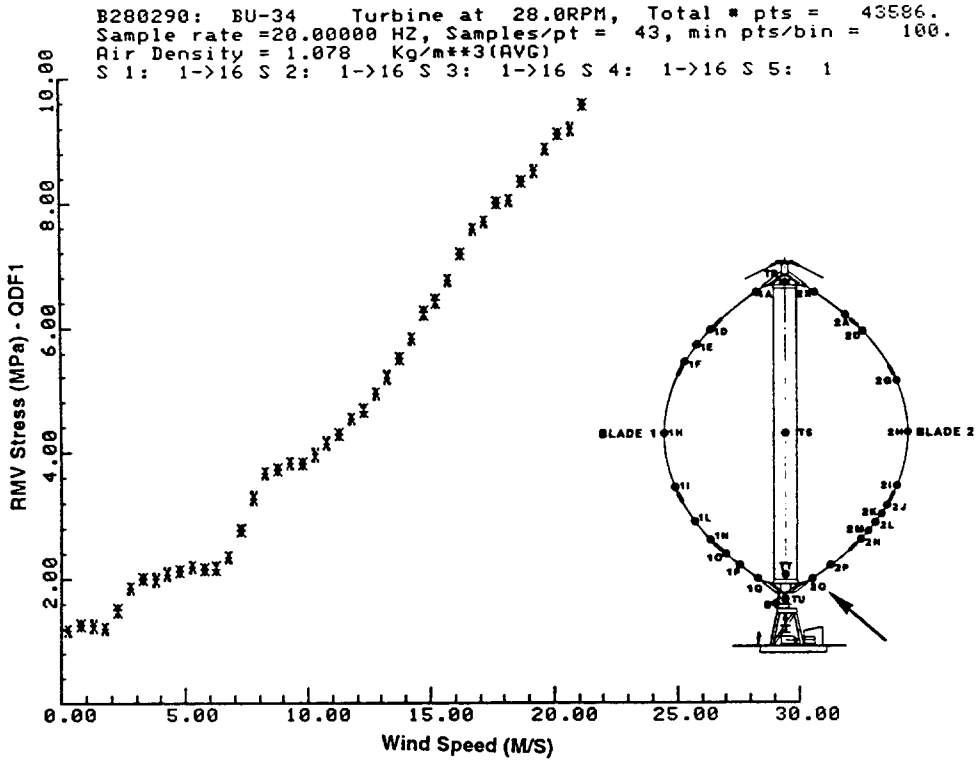

Figure A-27. RMV Stress vs. Wind Speed at 28 RPM - QDF1

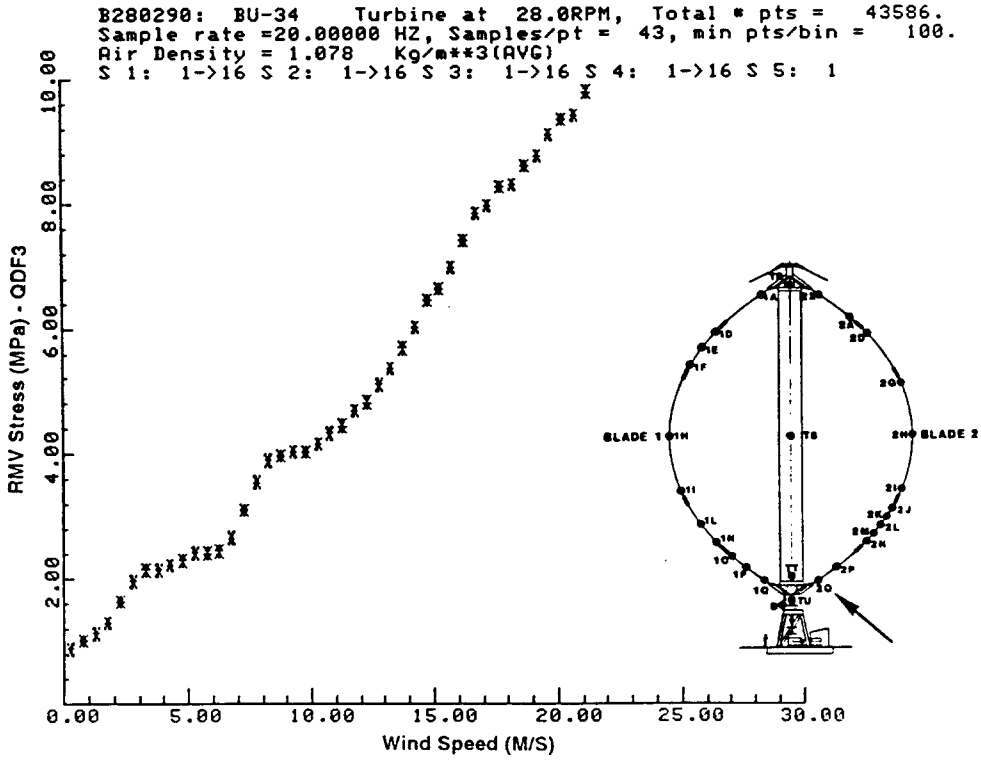

Figure A-28. RMV Stress vs. Wind Speed at 28 RPM - QDF3

APPENDIX B

RMV Stresses at 34 RPM

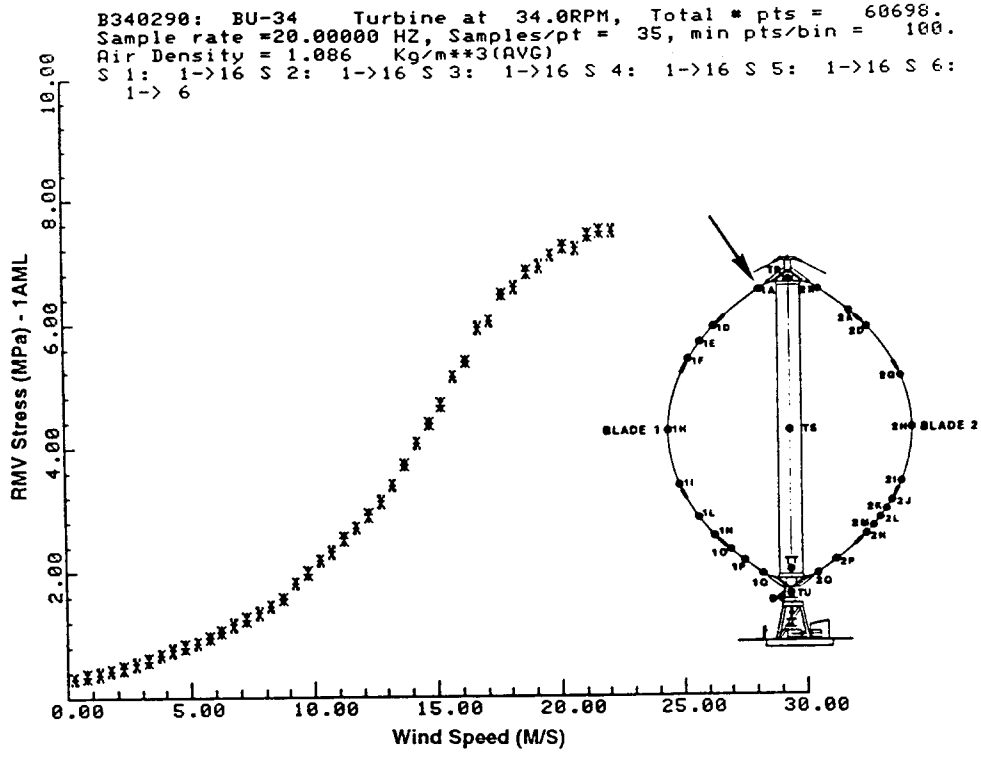

Figure B-1. RMV Stress vs. Wind Speed at 34 RPM - 1AML

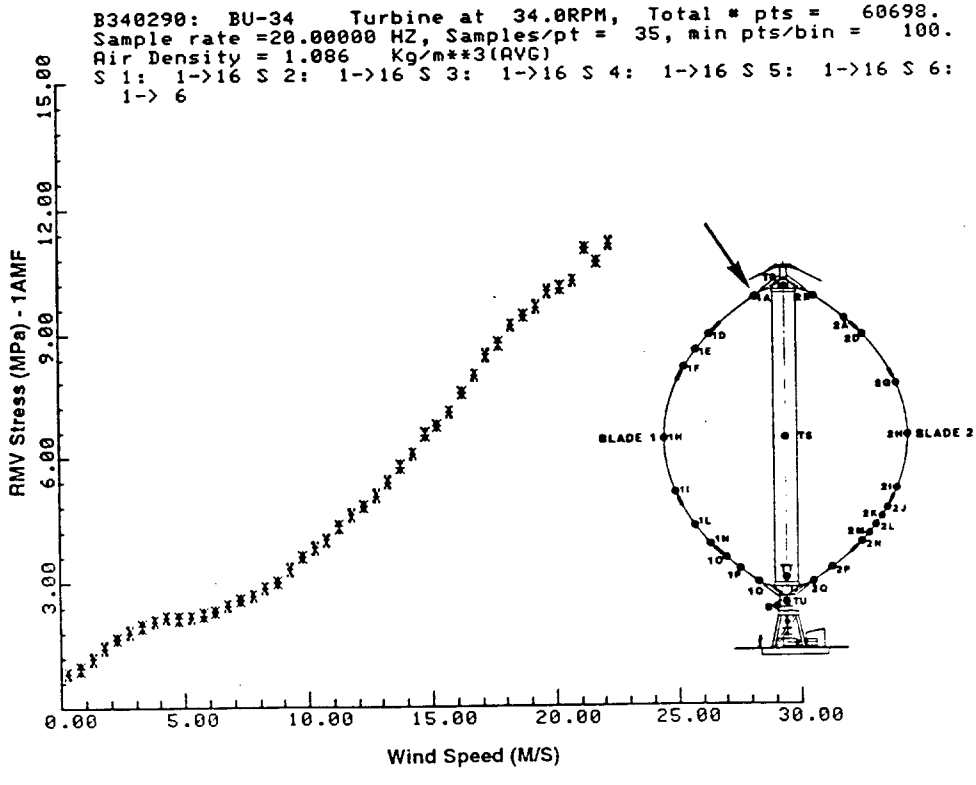

Figure B-2. RMV Stress vs. Wind Speed at 34 RPM - 1AMF

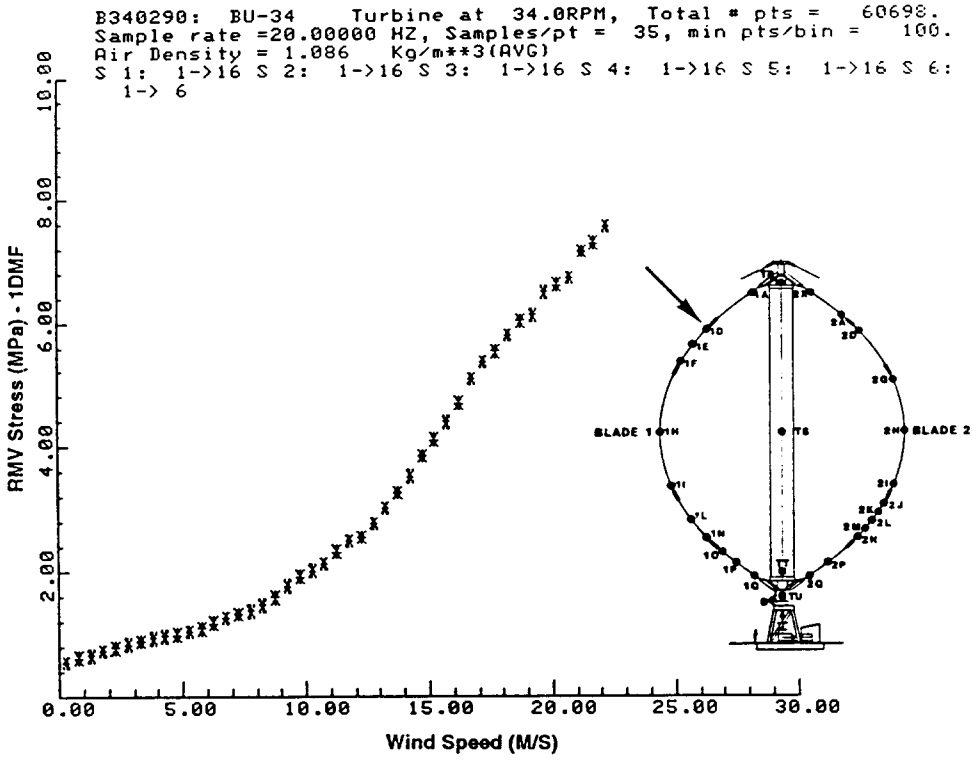

Figure B-3. RMV Stress vs. Wind Speed at 34 RPM - 1DMF

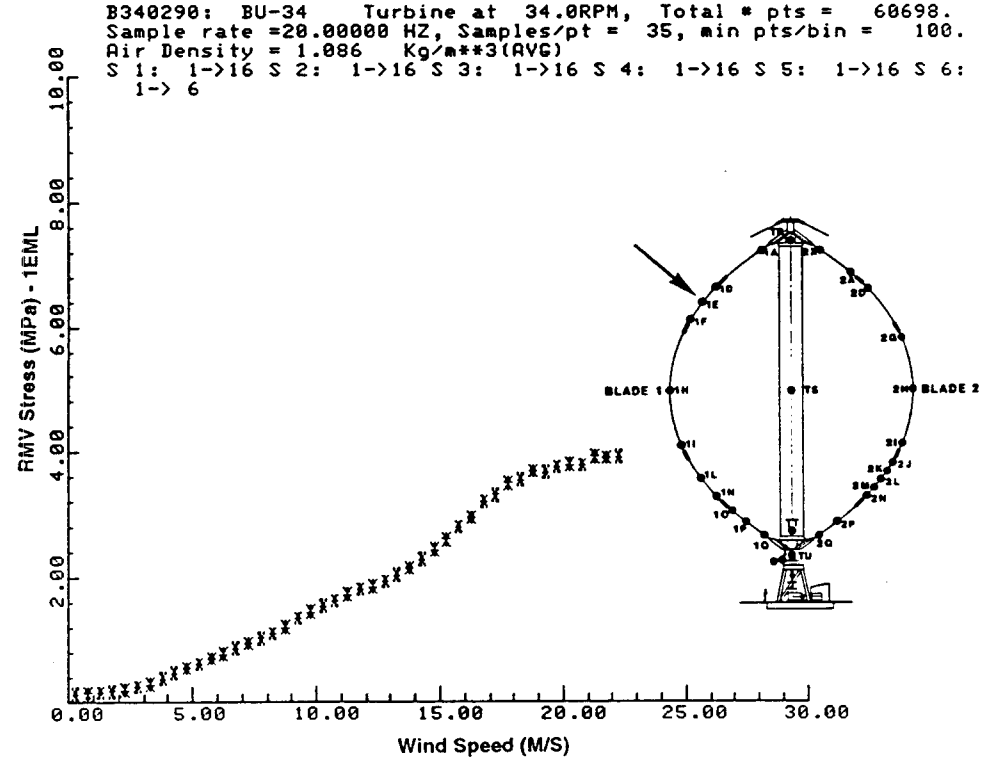

Figure B-4. RMV Stress vs. Wind Speed at 34 RPM - 1EML

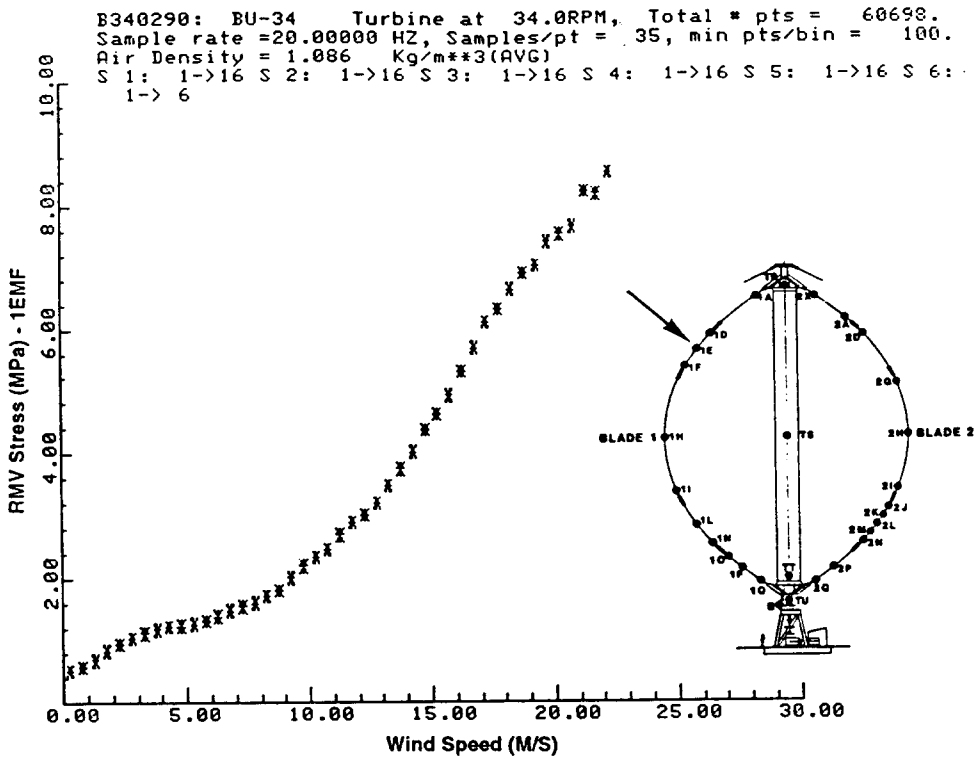

Figure B-5. RMV Stress vs. Wind Speed at 34 RPM - 1EMF

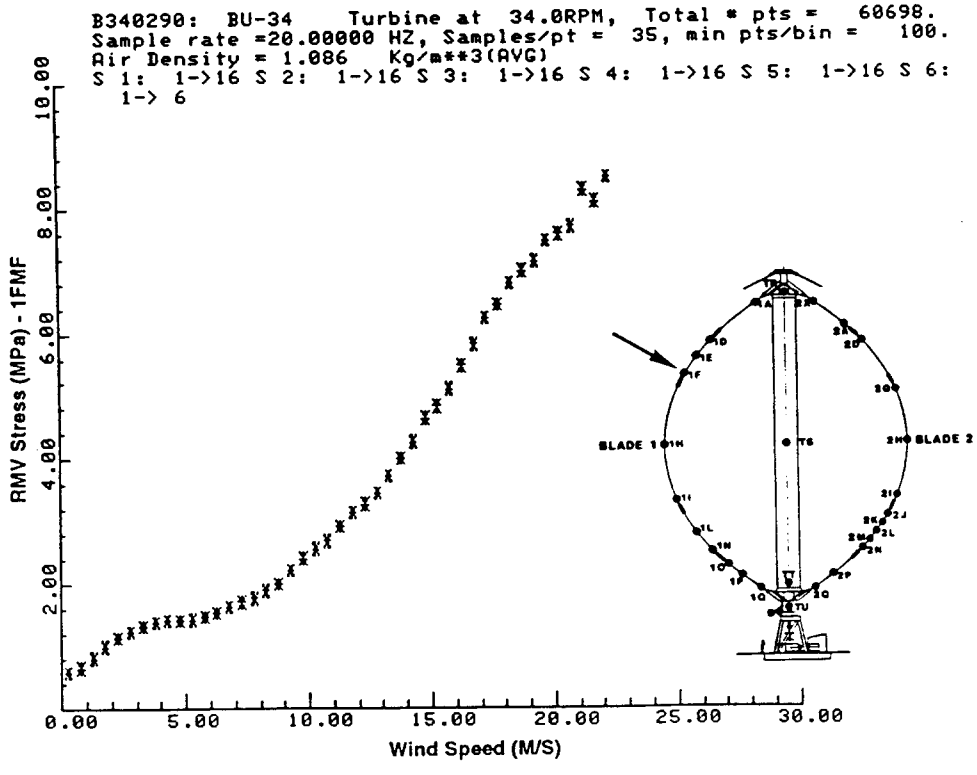

Figure B-6. RMV Stress vs. Wind Speed at 34 RPM - 1FMF

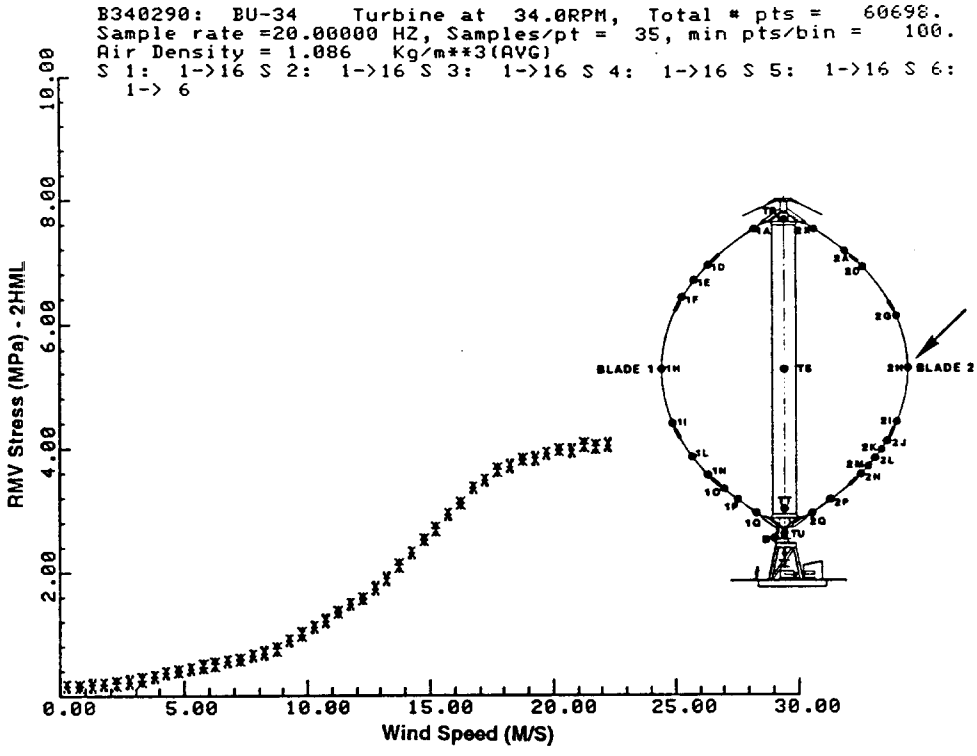

Figure B-7. RMV Stress vs. Wind Speed at 34 RPM - 2HML

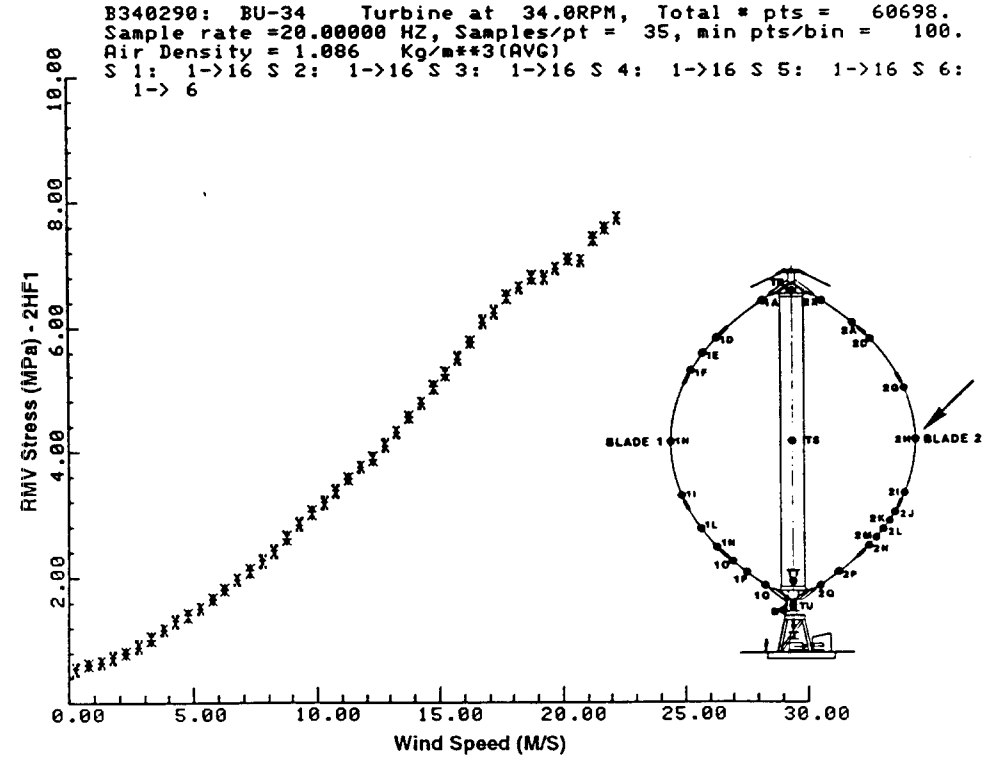

Figure B-8. RMV Stress vs. Wind Speed at 34 RPM - 2HF1

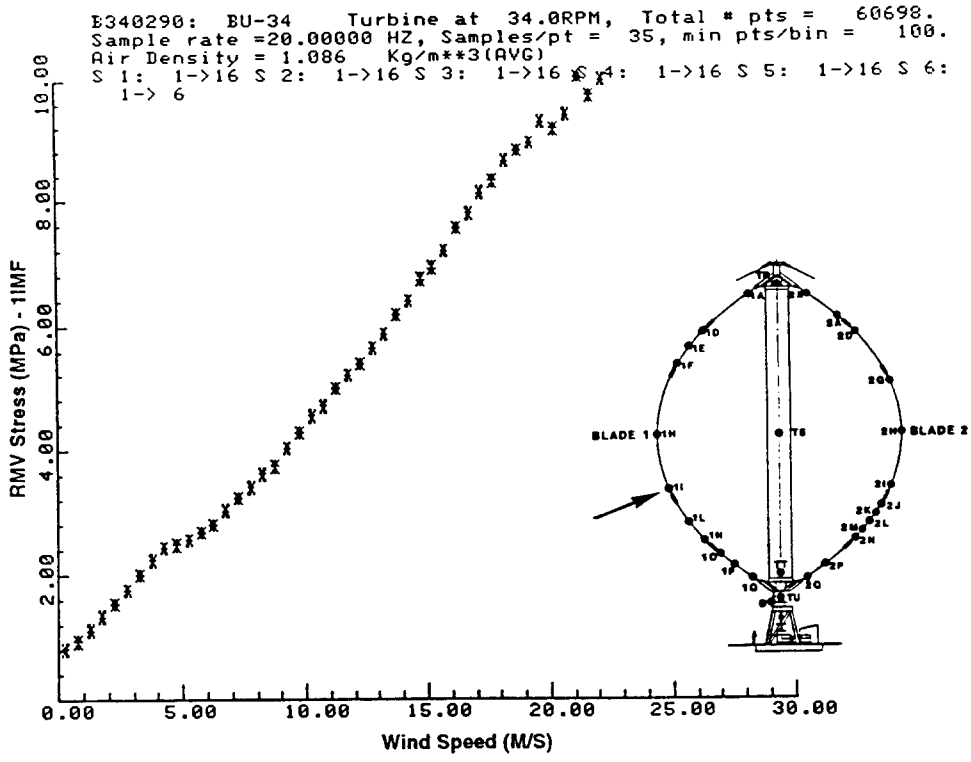

Figure B-9. RMV Stress vs. Wind Speed at 34 RPM - 1IMF

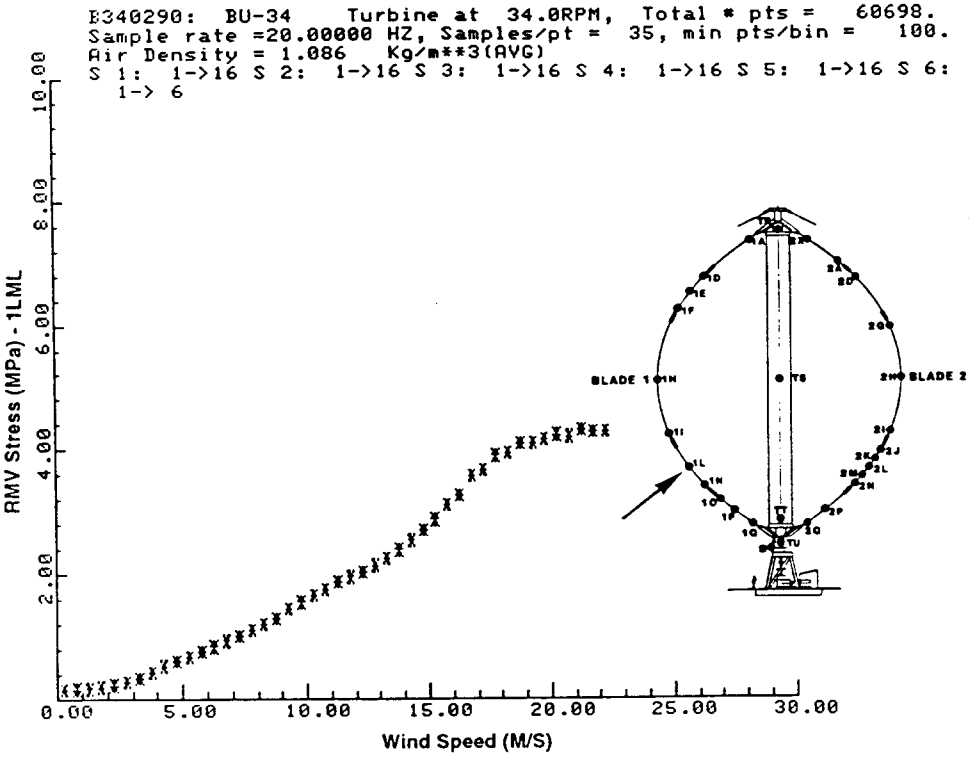

Figure B-10. RMV Stress vs. Wind Speed at 34 RPM - 1LML

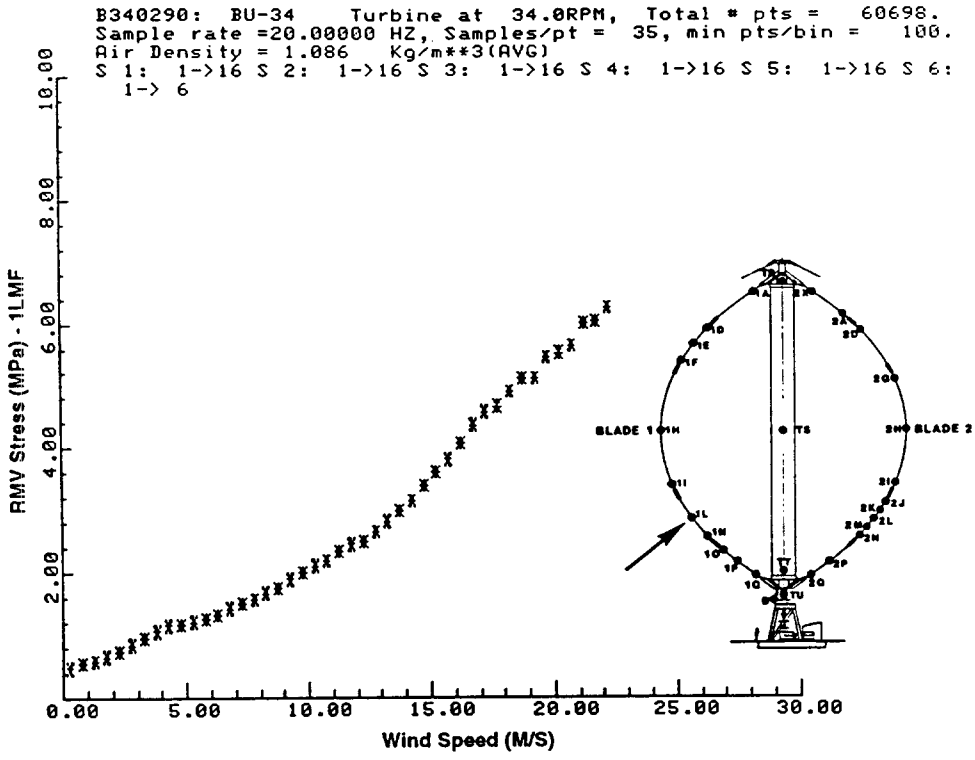

Figure B-11. RMV Stress vs. Wind Speed at 34 RPM - 1LMF

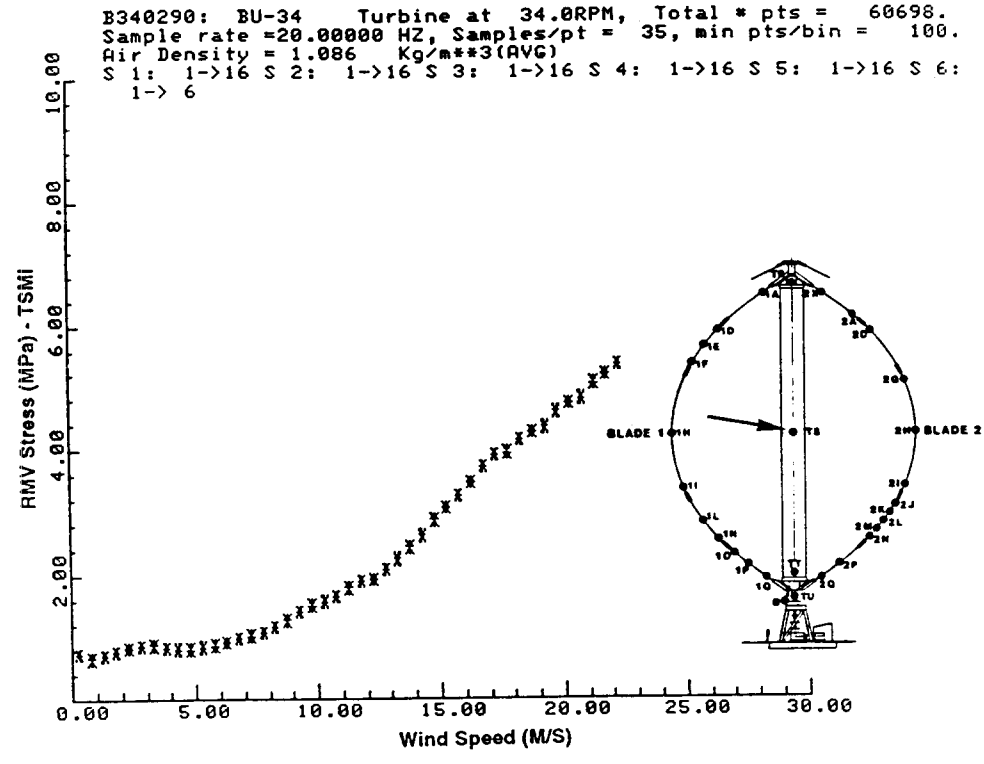

Figure B-12. RMV Stress vs. Wind Speed at 34 RPM - TSMI

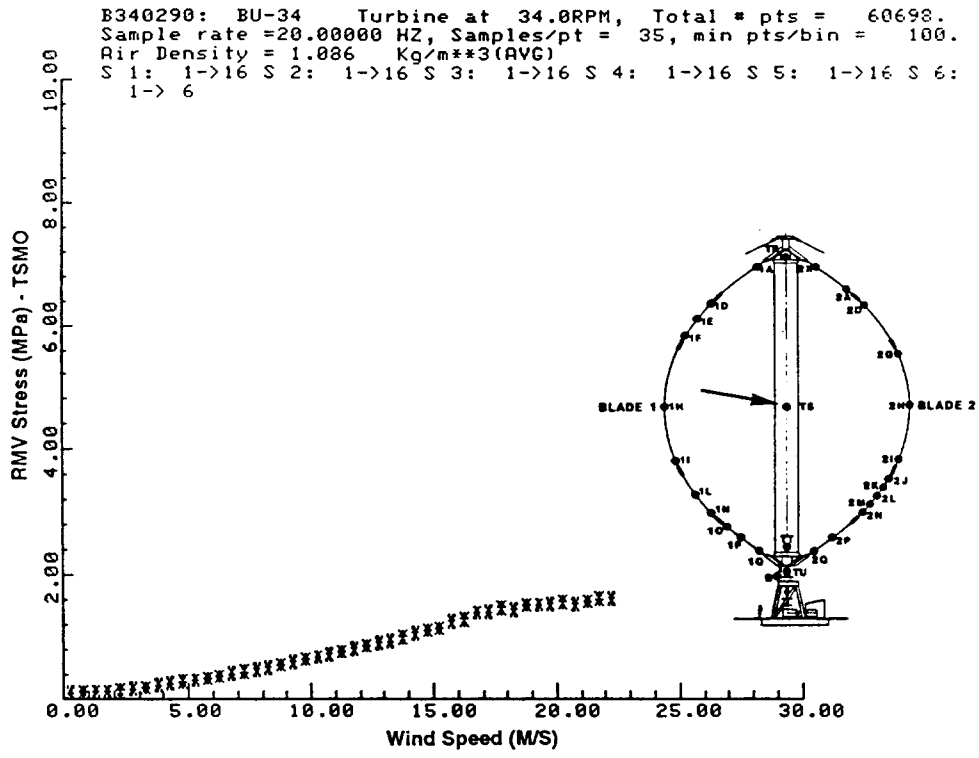

Figure B-13. RMV Stress vs. Wind Speed at 34 RPM - TSMO

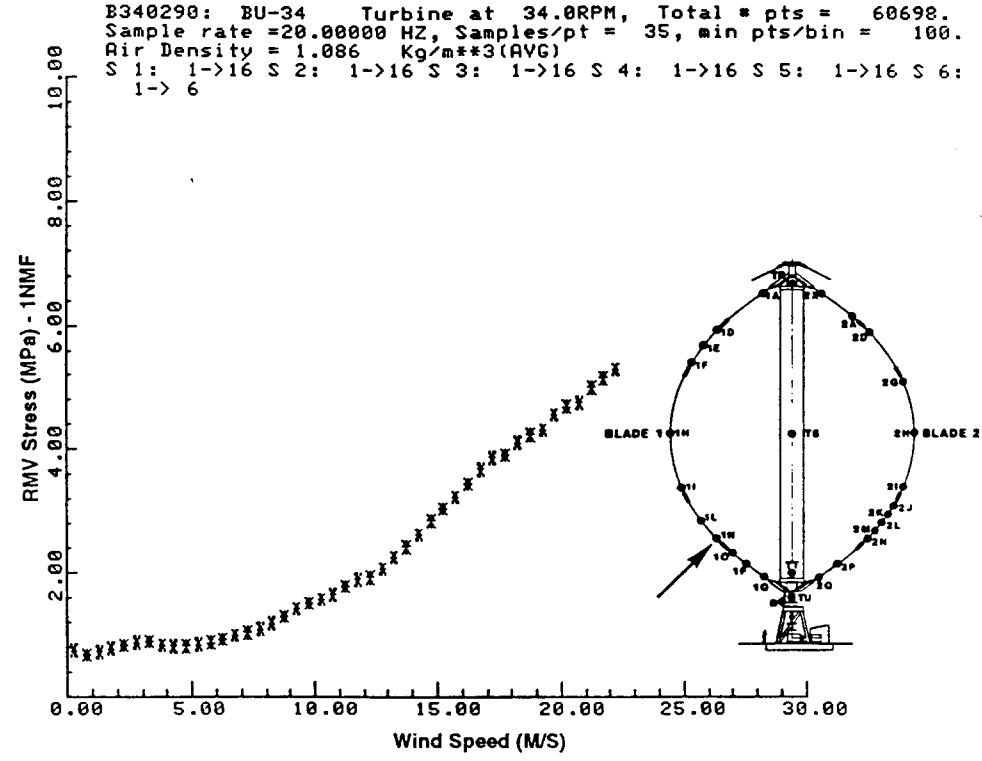

Figure B-14. RMV Stress vs. Wind Speed at 34 RPM - 1NMF

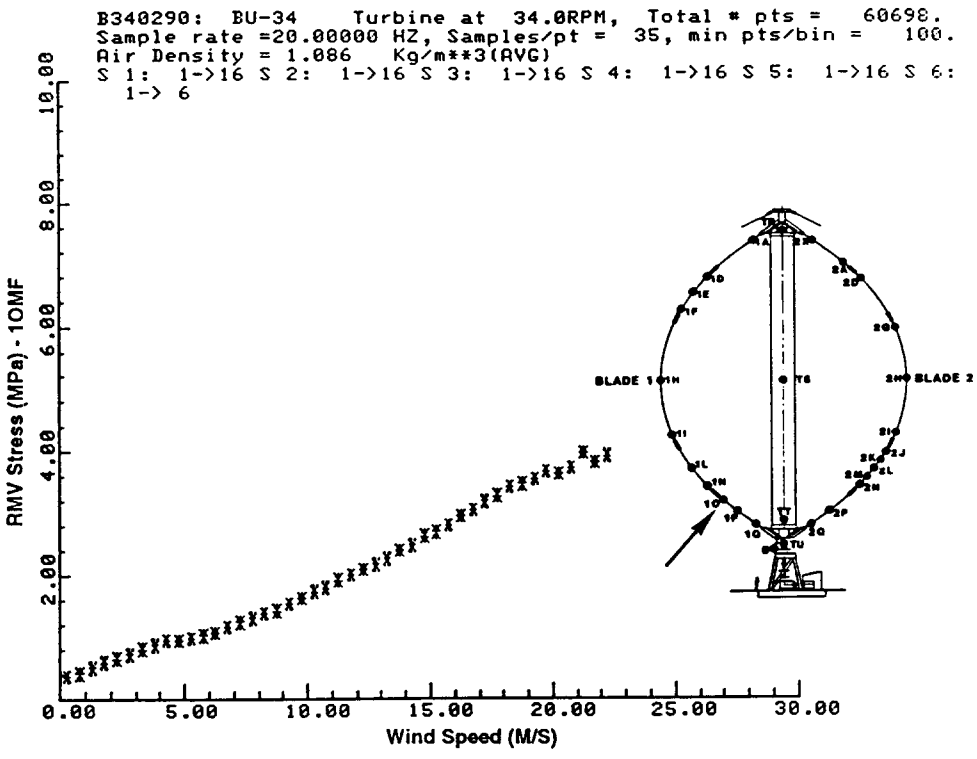

Figure B-15. RMV Stress vs. Wind Speed at 34 RPM - 1OMF

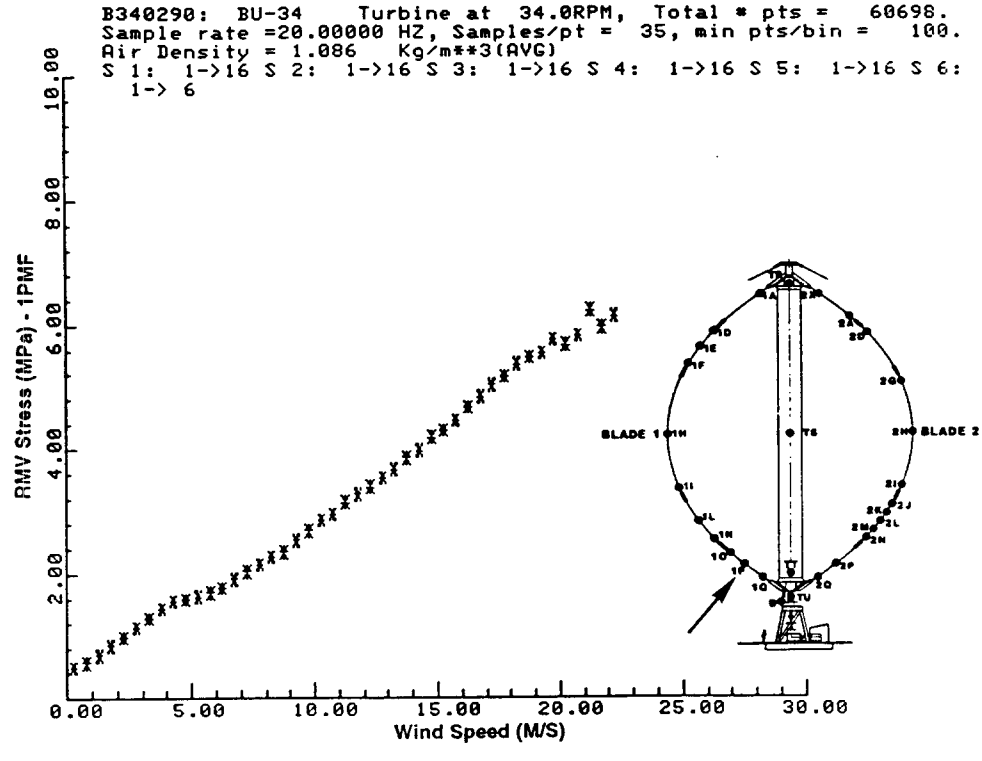

Figure B-16. RMV Stress vs. Wind Speed at 34 RPM - 1PMF

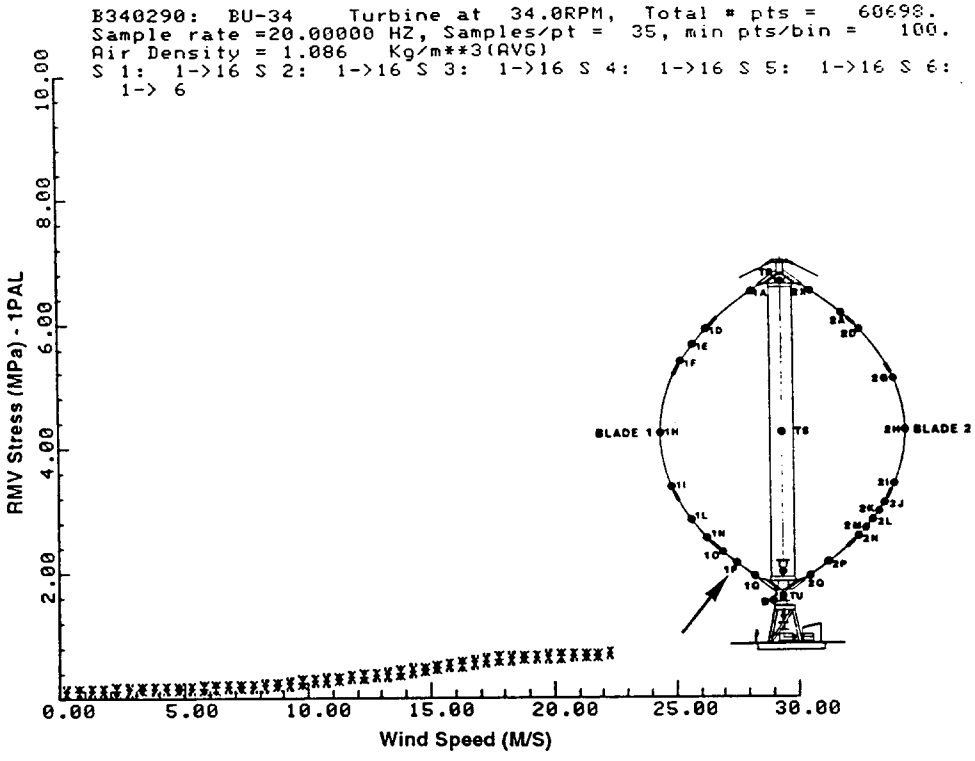

Figure B-17. RMV Stress vs. Wind Speed at 34 RPM - 1PAL

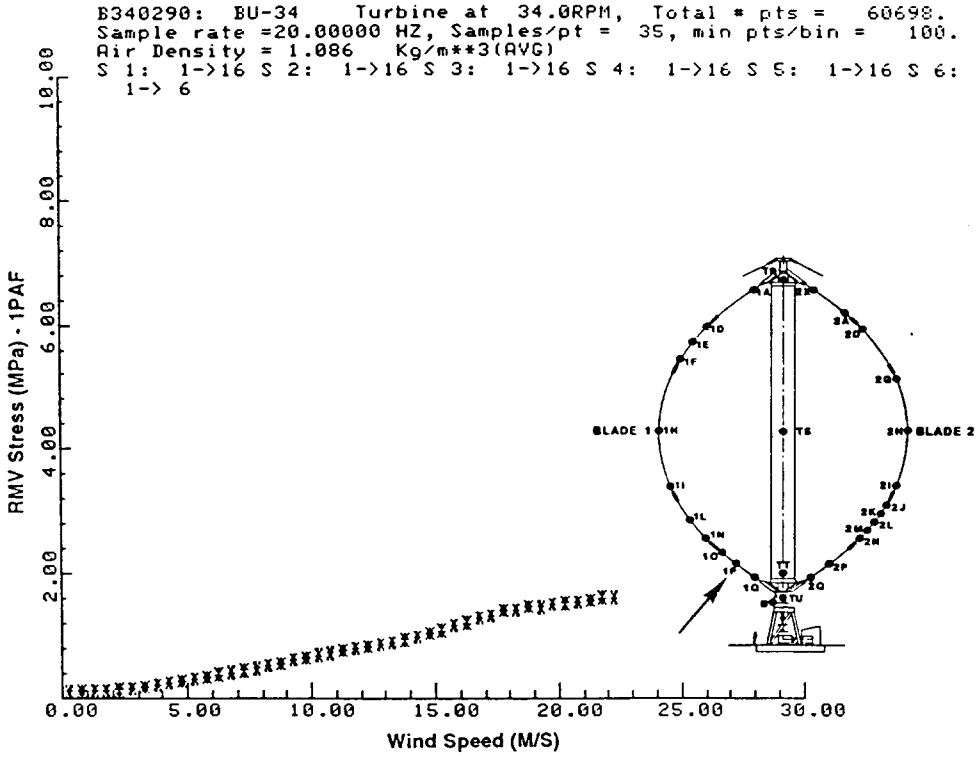

Figure B-18. RMV Stress vs. Wind Speed at 34 RPM - 1PAF

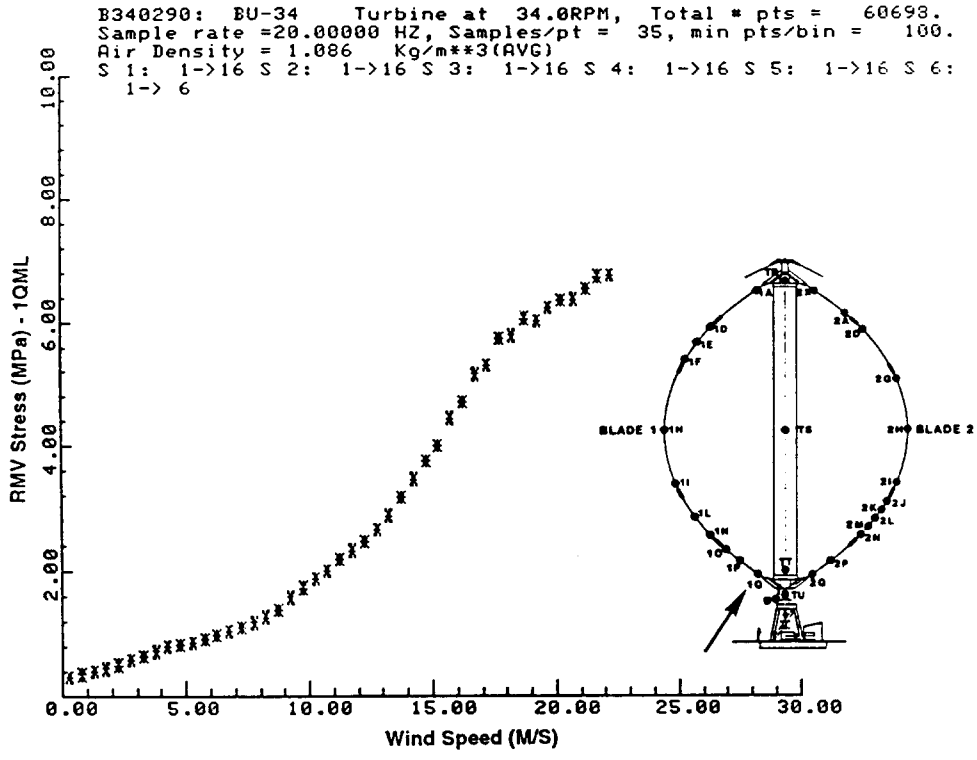

Figure B-19. RMV Stress vs. Wind Speed at 34 RPM - 1QML

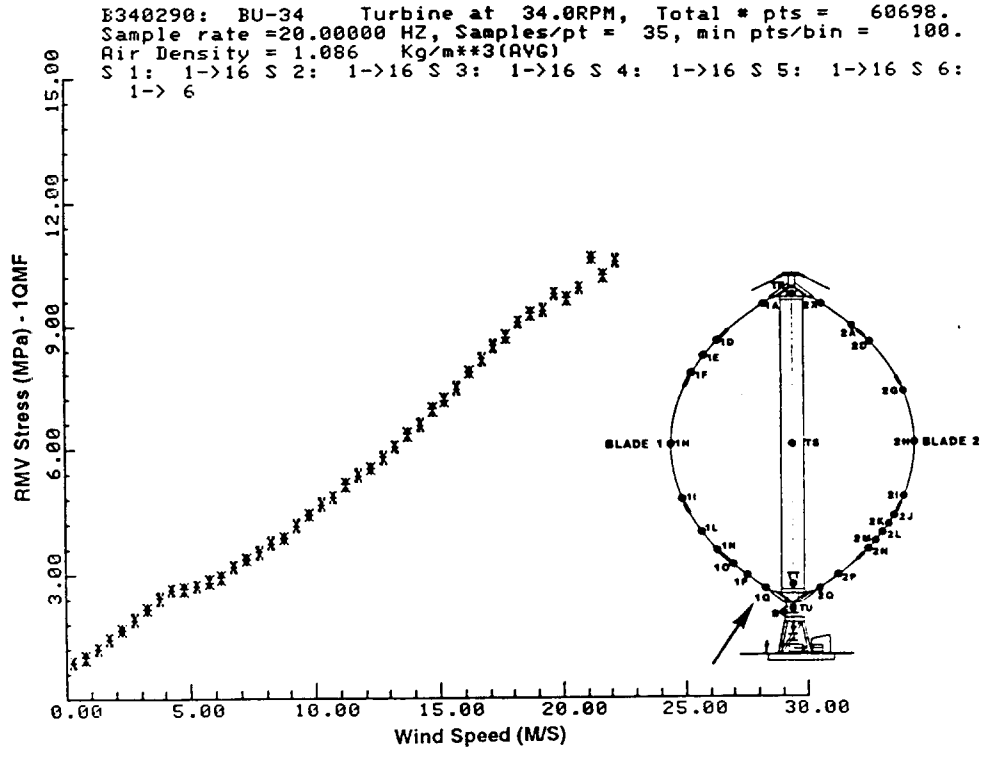

Figure B-20. RMV Stress vs. Wind Speed at 34 RPM - 1QMF

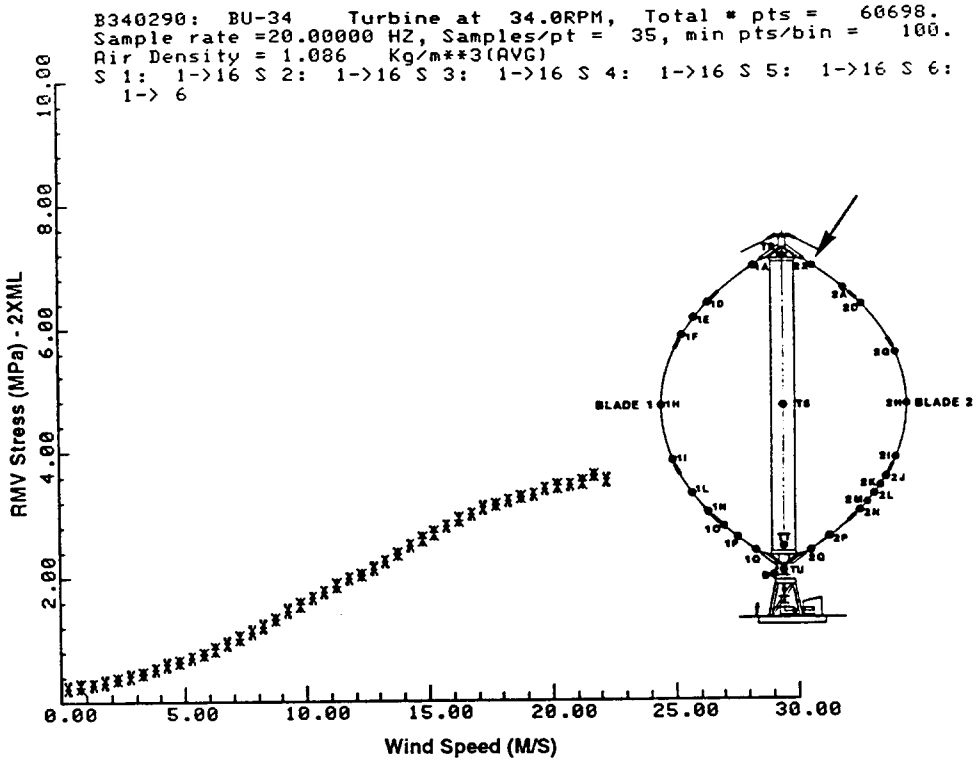

Figure B-21. RMV Stress vs. Wind Speed at 34 RPM - 2XML

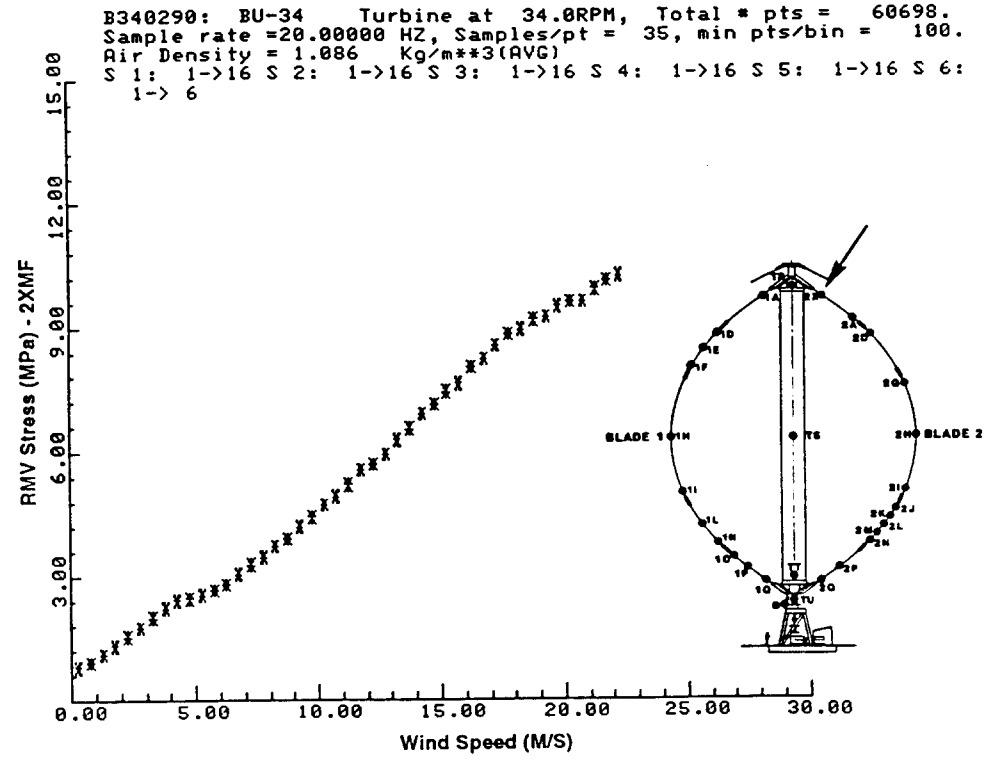

Figure B-22. RMV Stress vs. Wind Speed at 34 RPM - 2XMF

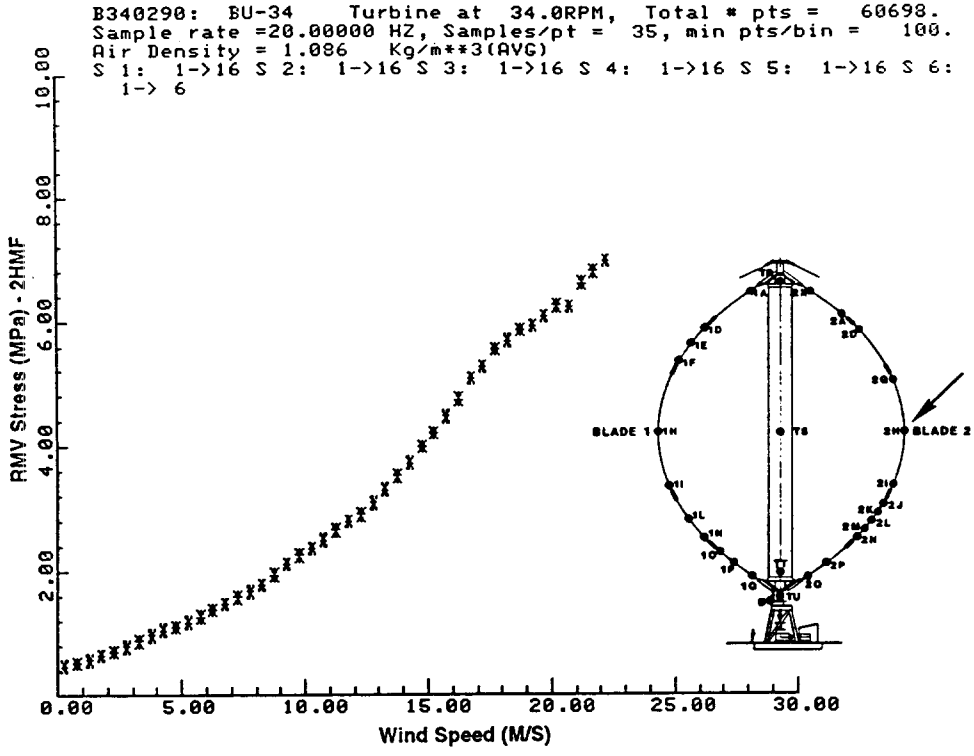

Figure B-23. RMV Stress vs. Wind Speed at 34 RPM - 2HMF

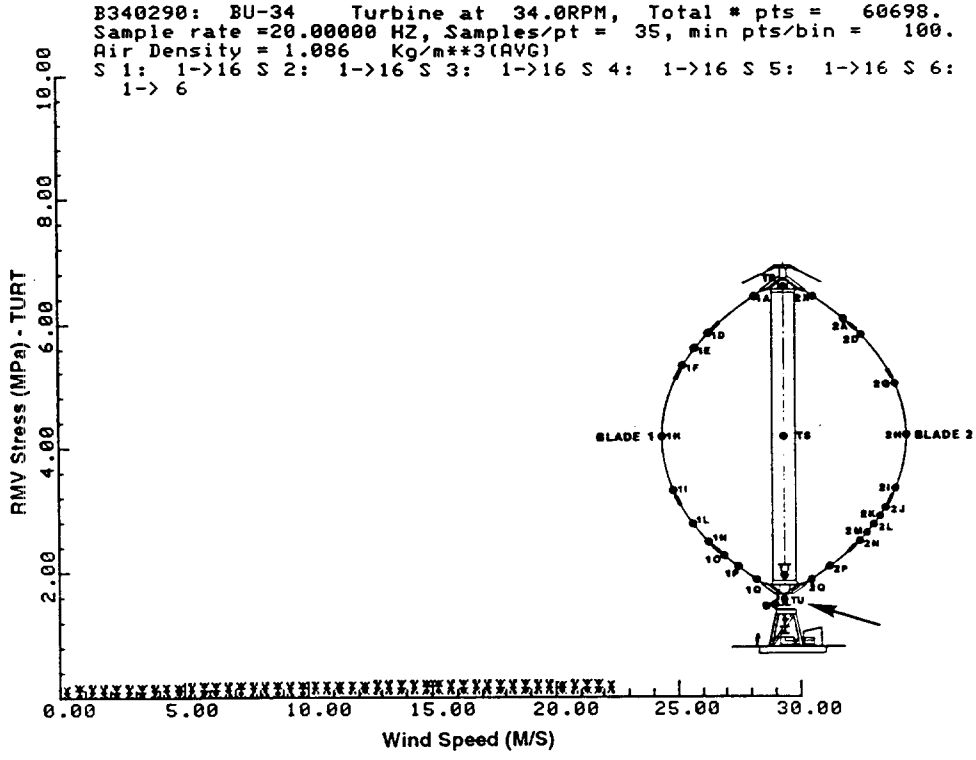

Figure B-24. RMV Stress vs. Wind Speed at 34 RPM - TURT

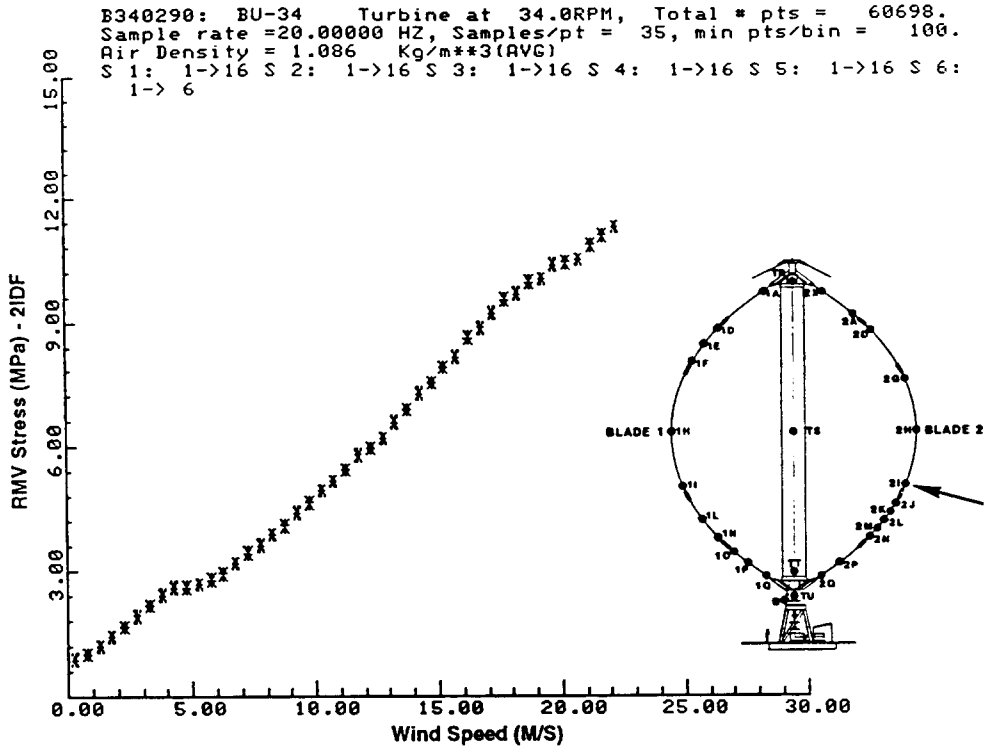

Figure B-25. RMV Stress vs. Wind Speed at 34 RPM - 2IDF

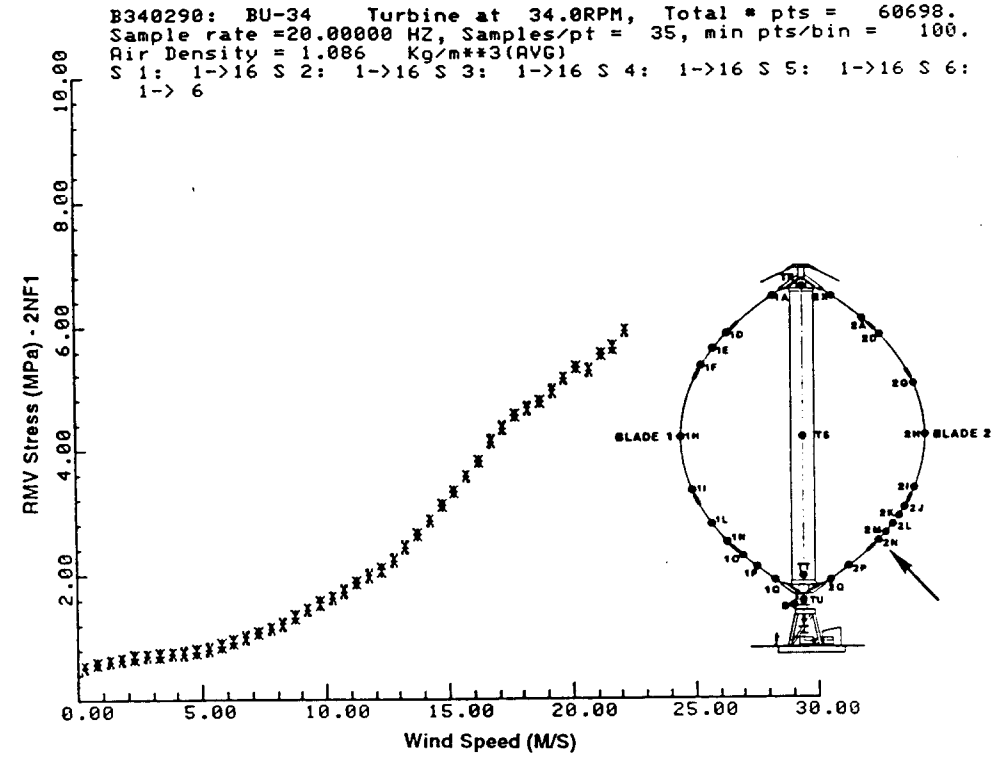

Figure B-26. RMV Stress vs. Wind Speed at 34 RPM - 2NF1

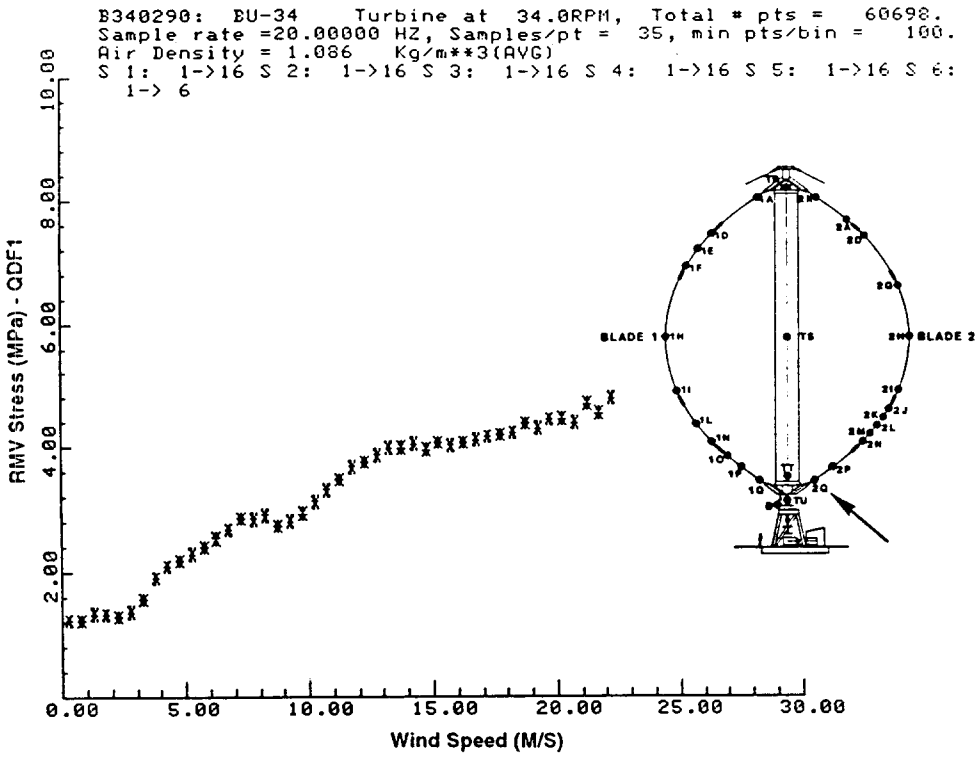

Figure B-27. RMV Stress vs. Wind Speed at 34 RPM - QDF1

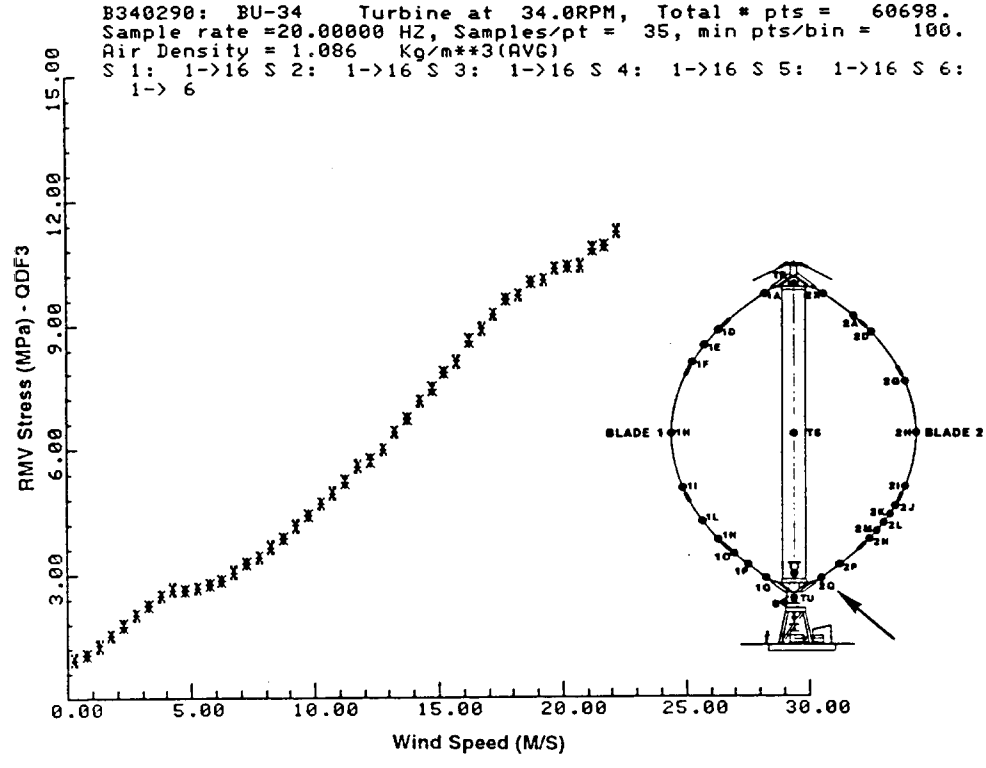

Figure B-28. RMV Stress vs. Wind Speed at 34 RPM - QDF3

APPENDIX C

RMV Stresses at 38 RPM

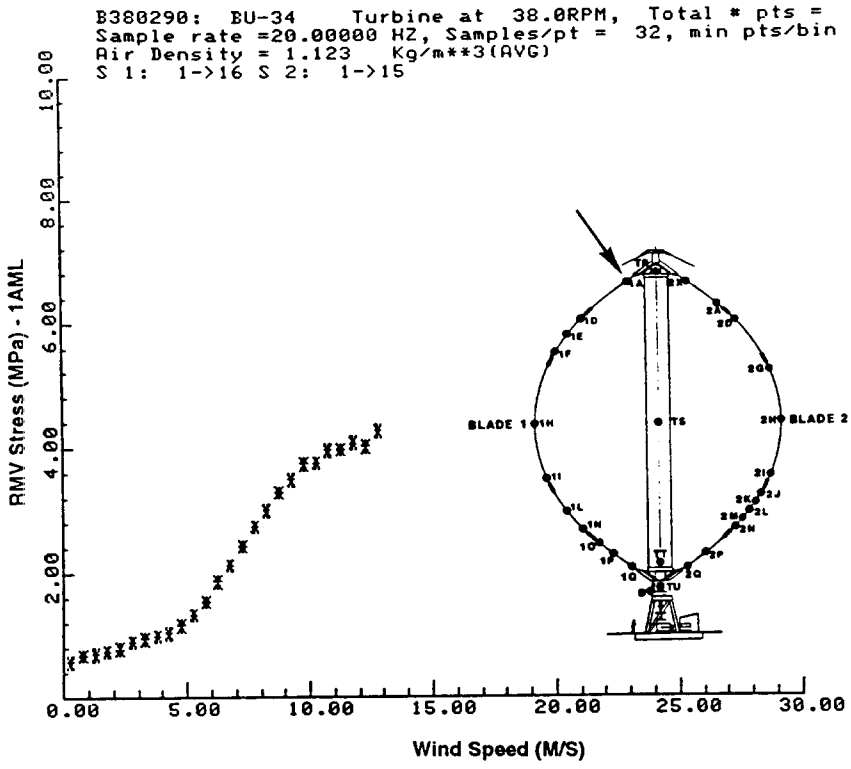

Figure C-1. RMV Stress vs. Wind Speed at 38 RPM - 1AML

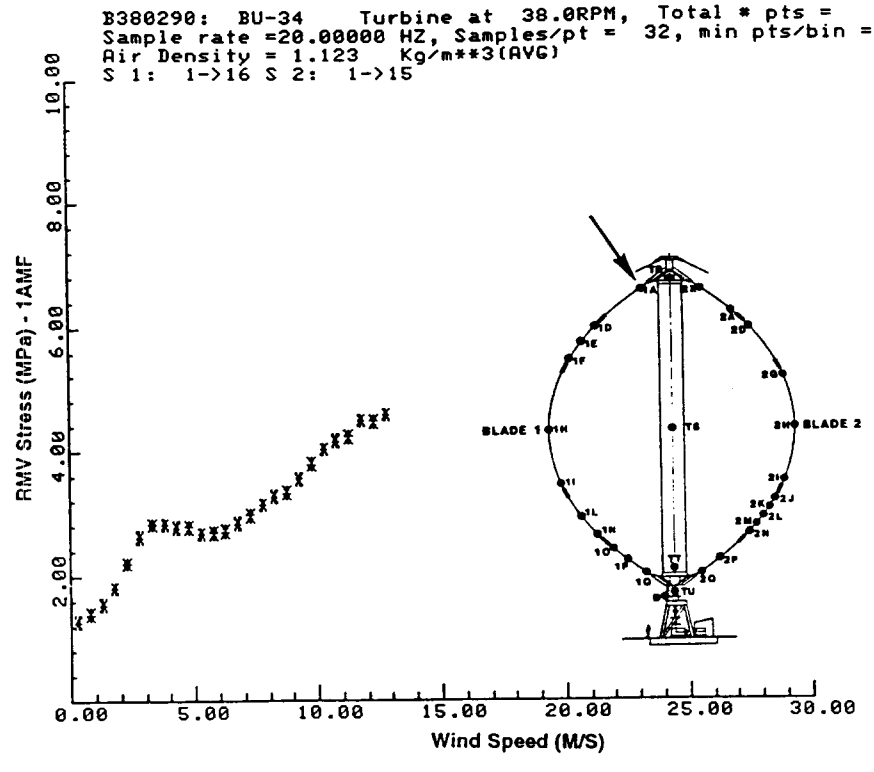

Figure C-2. RMV Stress vs. Wind Speed at 38 RPM - 1AMF

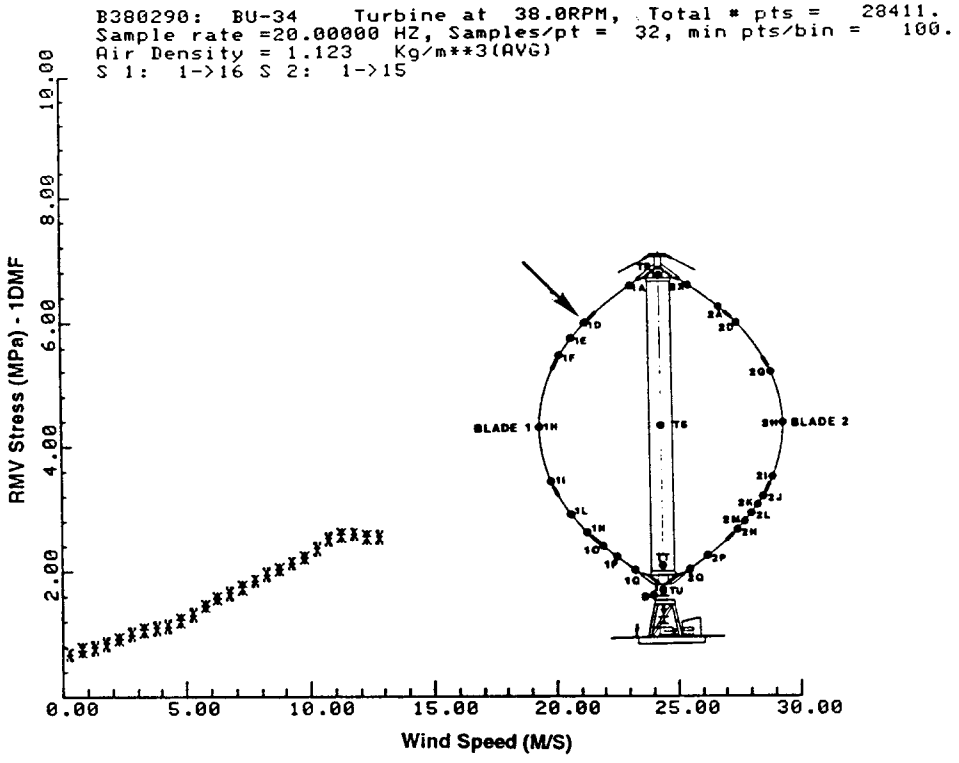

Figure C-3. RMV Stress vs. Wind Speed at 38 RPM - 1DMF

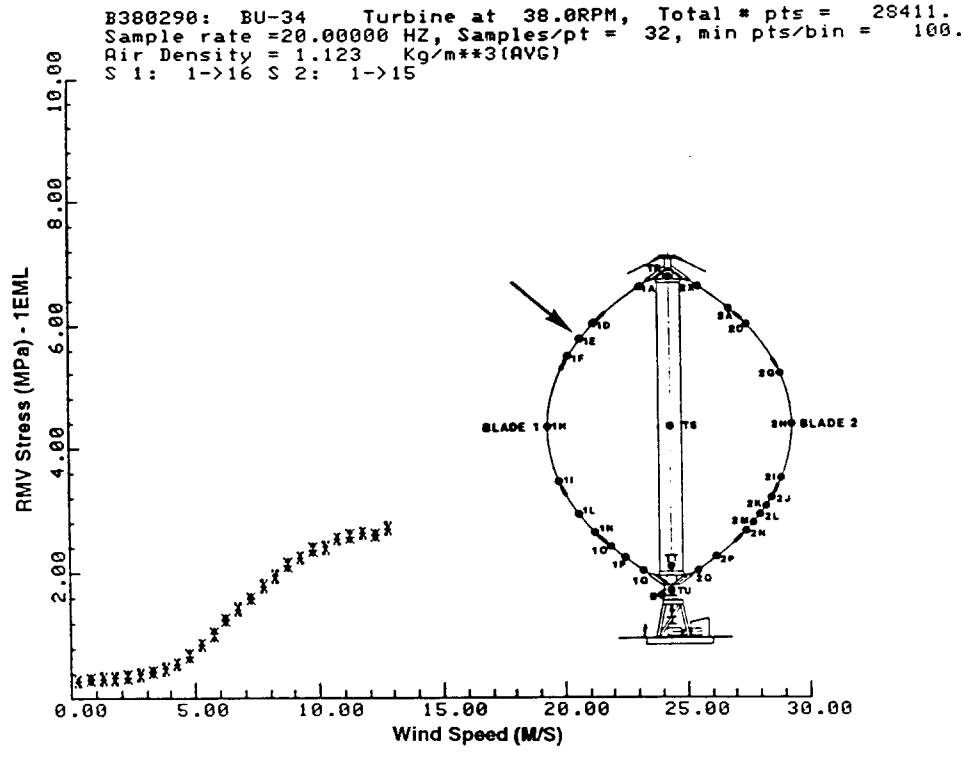

Figure C-4. RMV Stress vs. Wind Speed at 38 RPM - 1EML

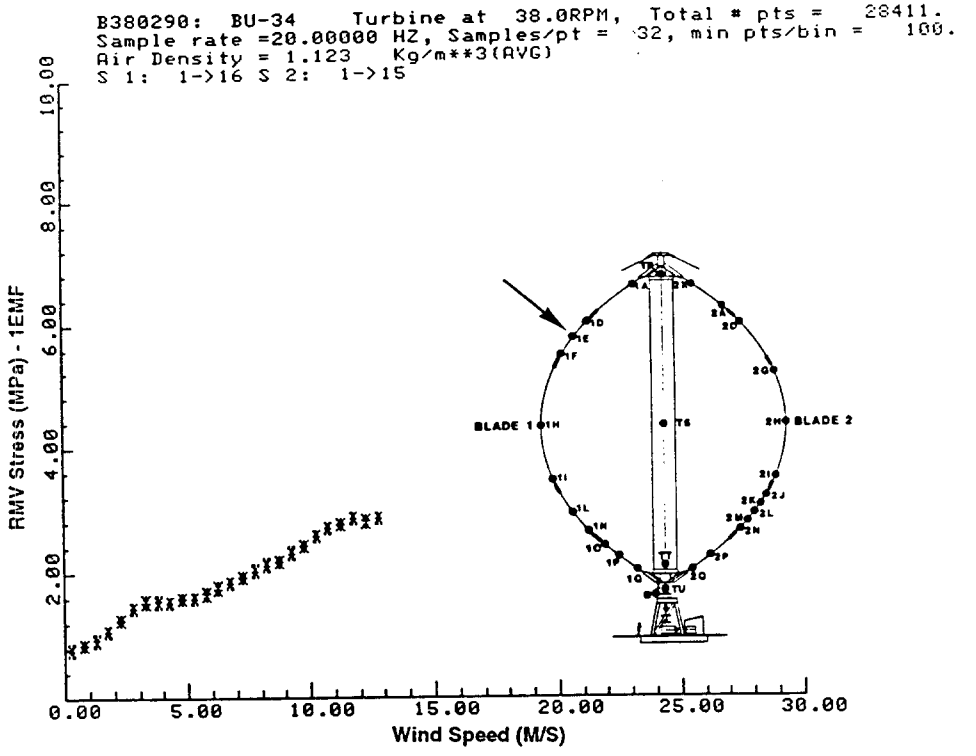

Figure C-5. RMV Stress vs. Wind Speed at 38 RPM - 1EMF

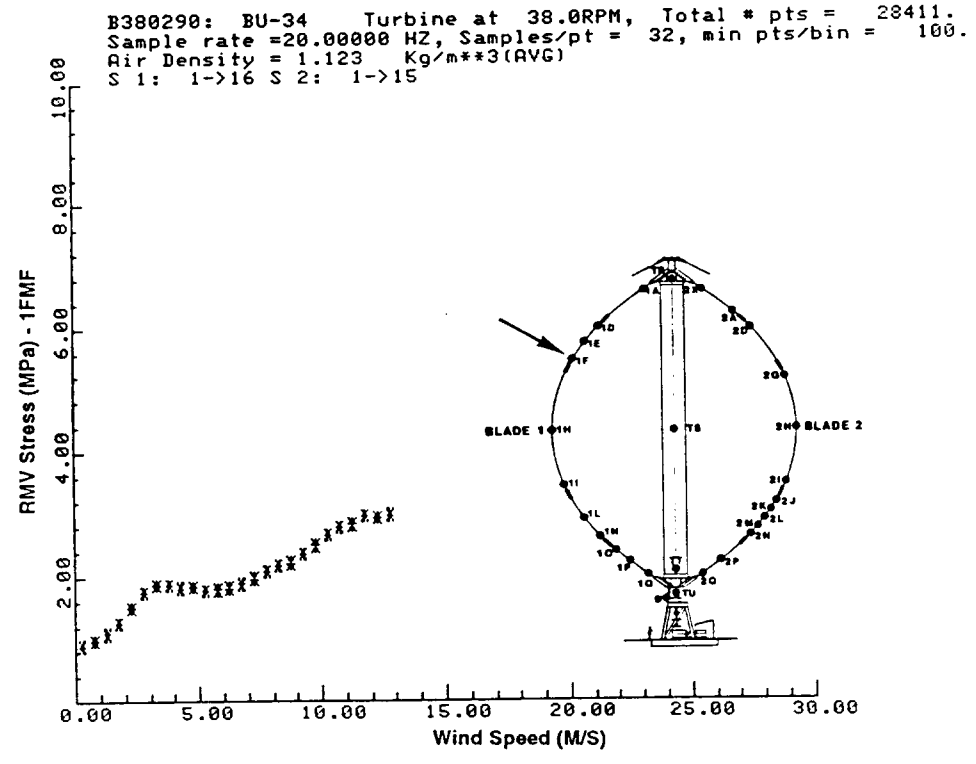

Figure C-6. RMV Stress vs. Wind Speed at 38 RPM - 1FMF

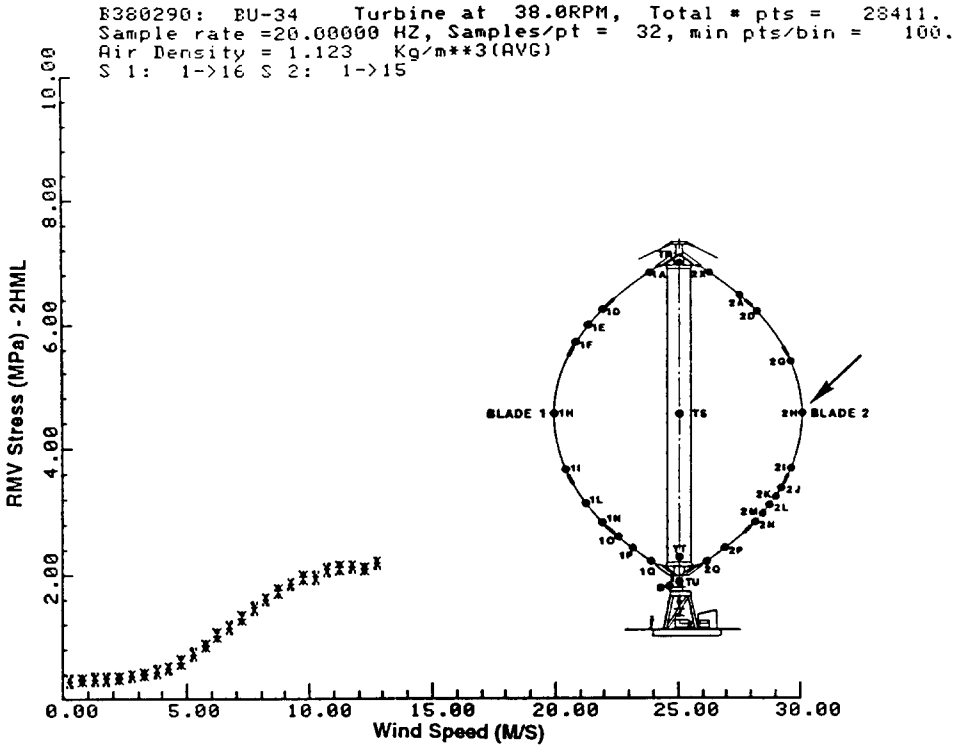

Figure C-7. RMV Stress vs. Wind Speed at 38 RPM - 2HML

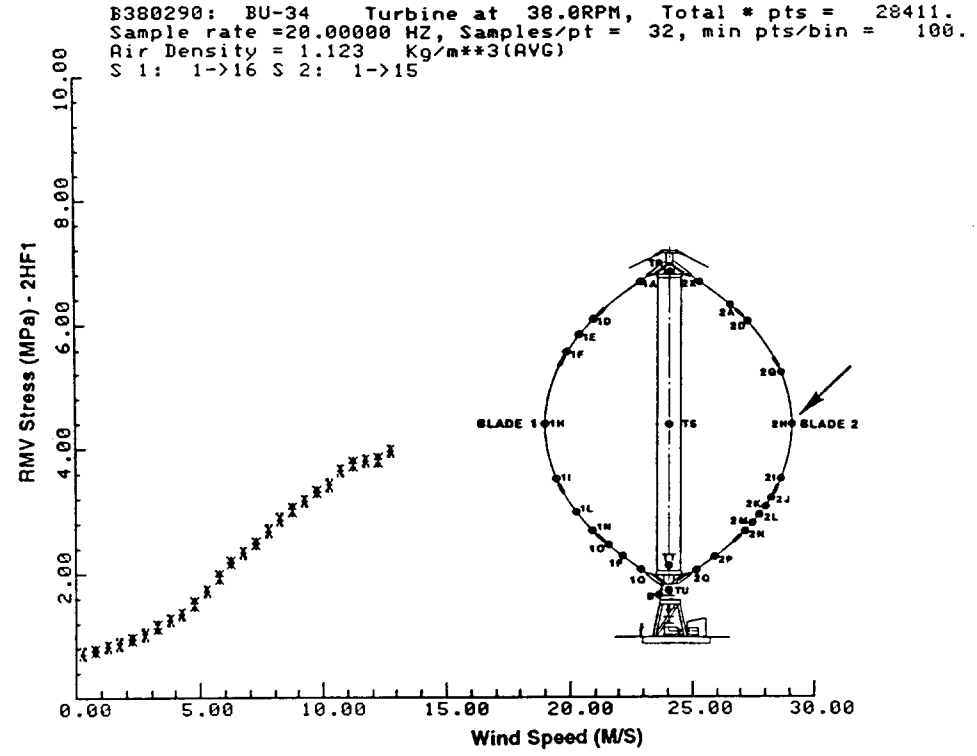

Figure C-8. RMV Stress vs. Wind Speed at 38 RPM - 2HF1

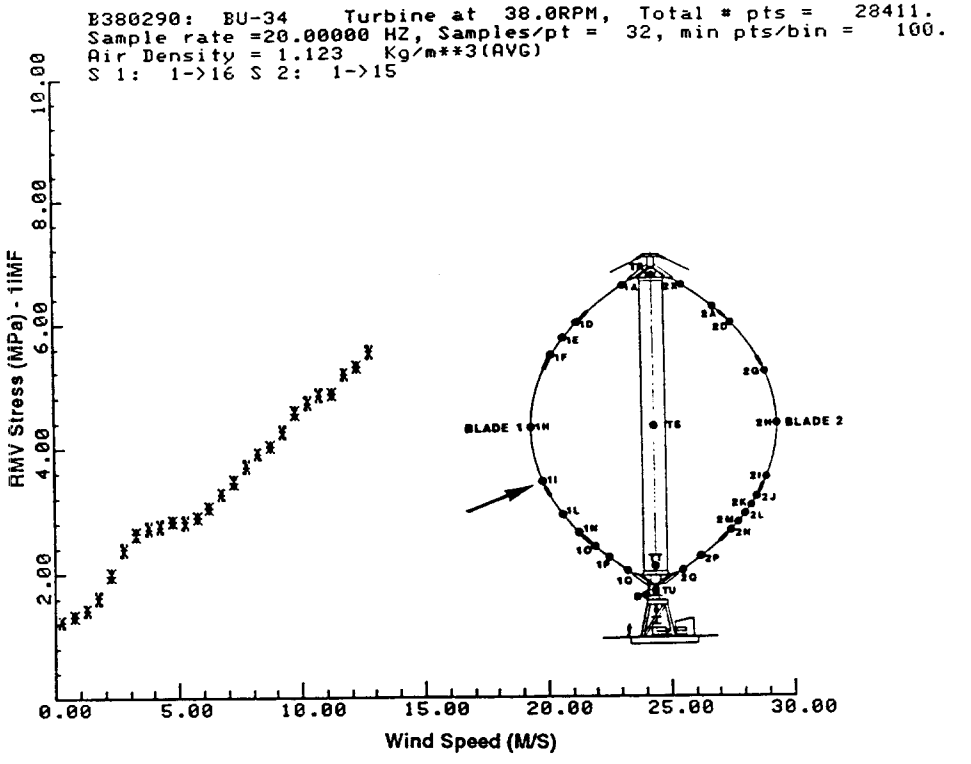

Figure C-9. RMV Stress vs. Wind Speed at 38 RPM - 1IMF

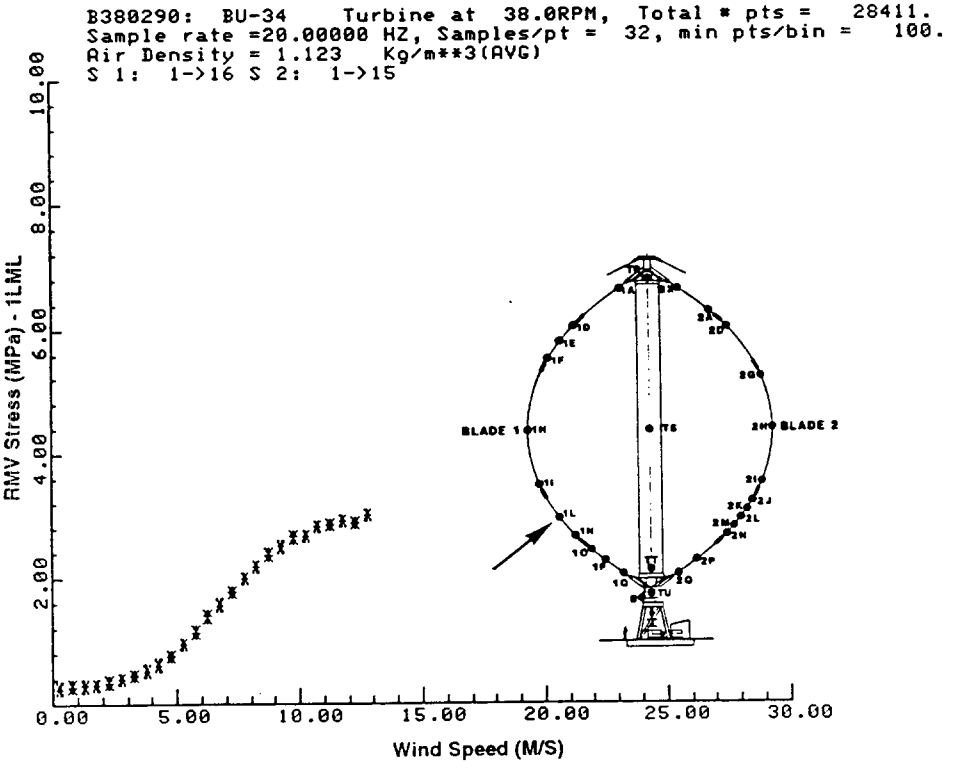

Figure C-10. RMV Stress vs. Wind Speed at 38 RPM - 1LML

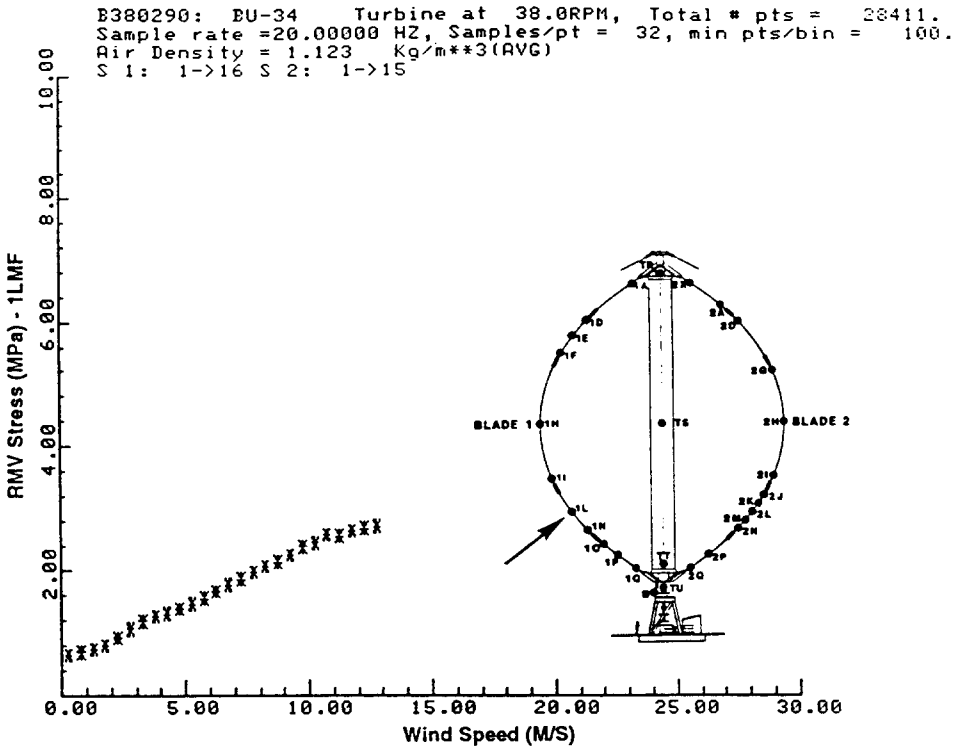

Figure C-11. RMV Stress vs. Wind Speed at 38 RPM - 1LMF

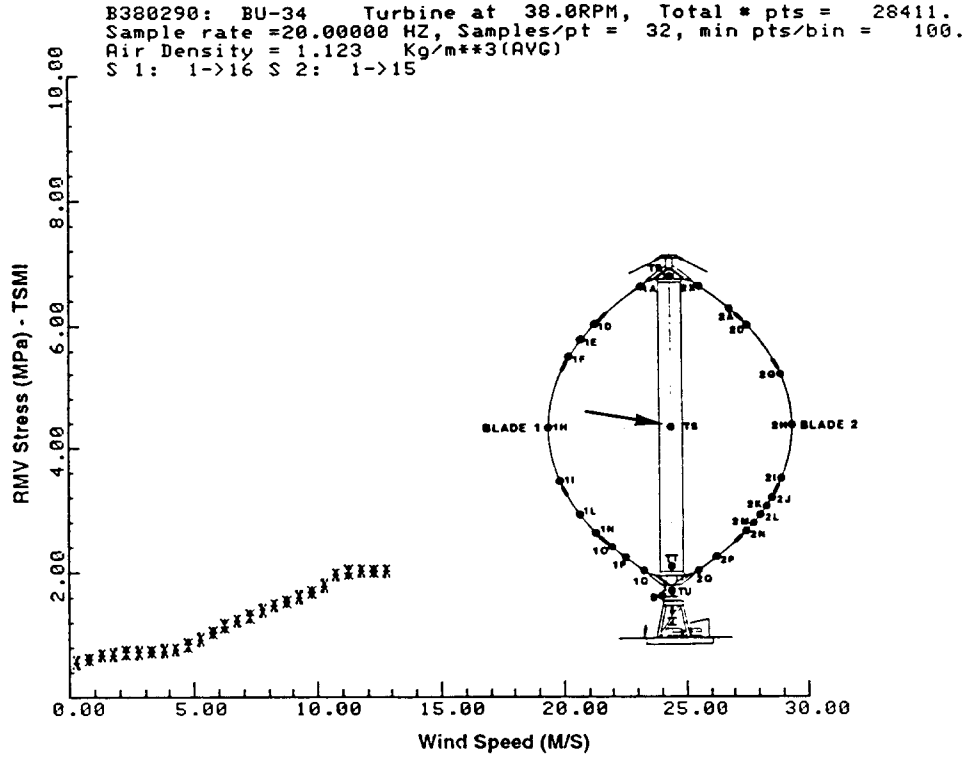

Figure C-12. RMV Stress vs. Wind Speed at 38 RPM - TSMI

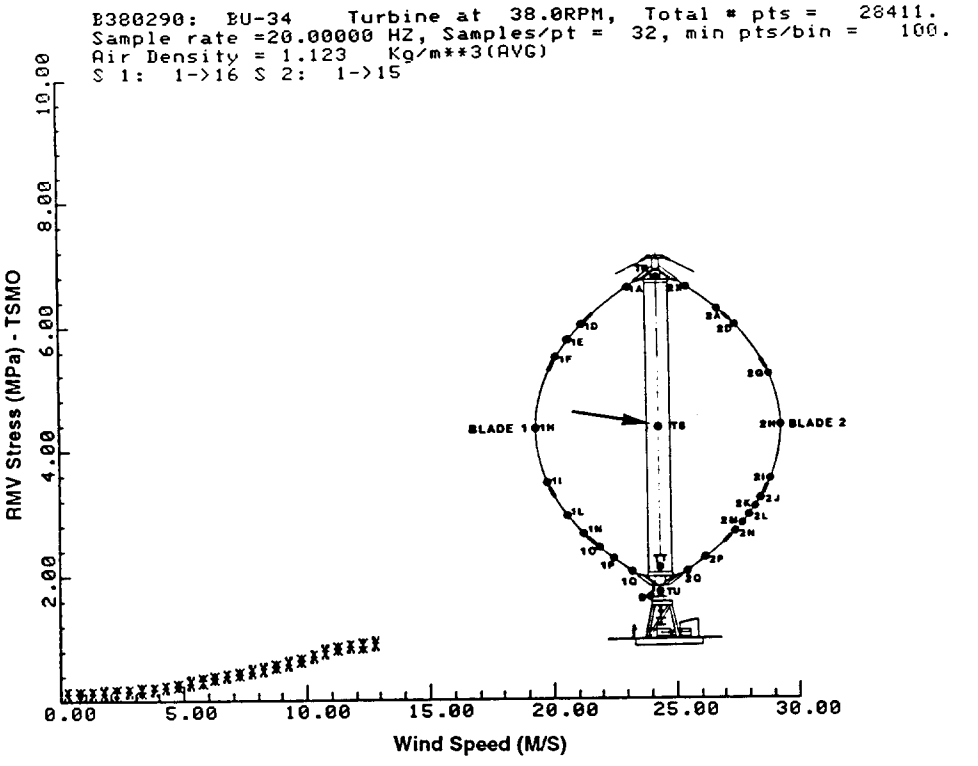

Figure C-13. RMV Stress vs. Wind Speed at 38 RPM - TSMO

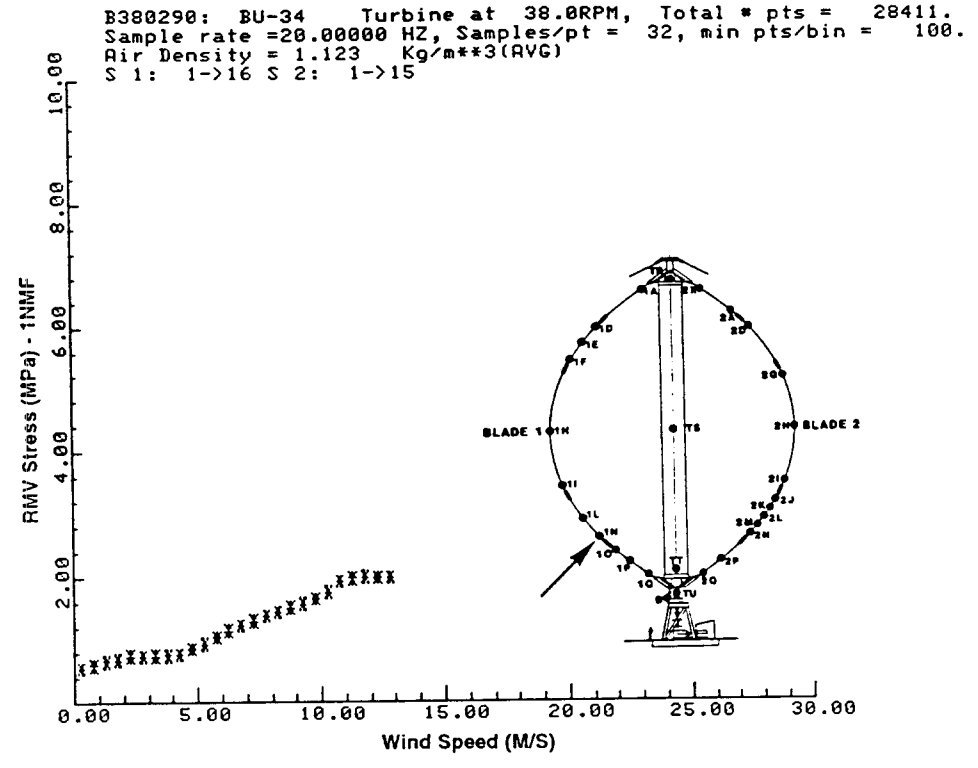

Figure C-14. RMV Stress vs. Wind Speed at 38 RPM - 1NMF

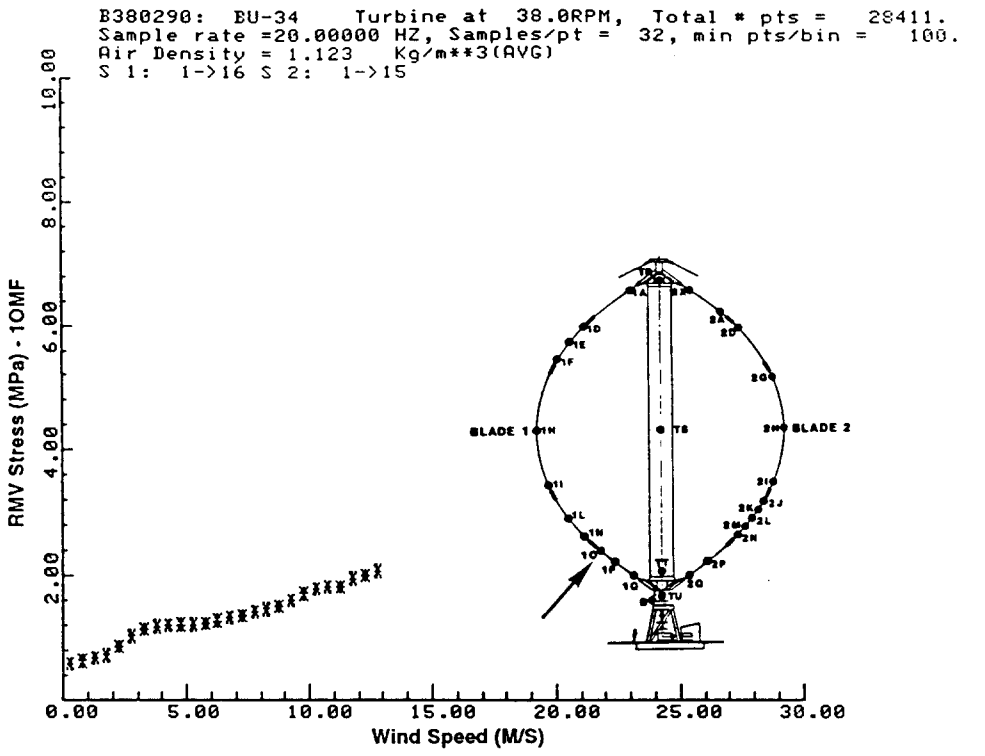

Figure C-15. RMV Stress vs. Wind Speed at 38 RPM - 1OMF

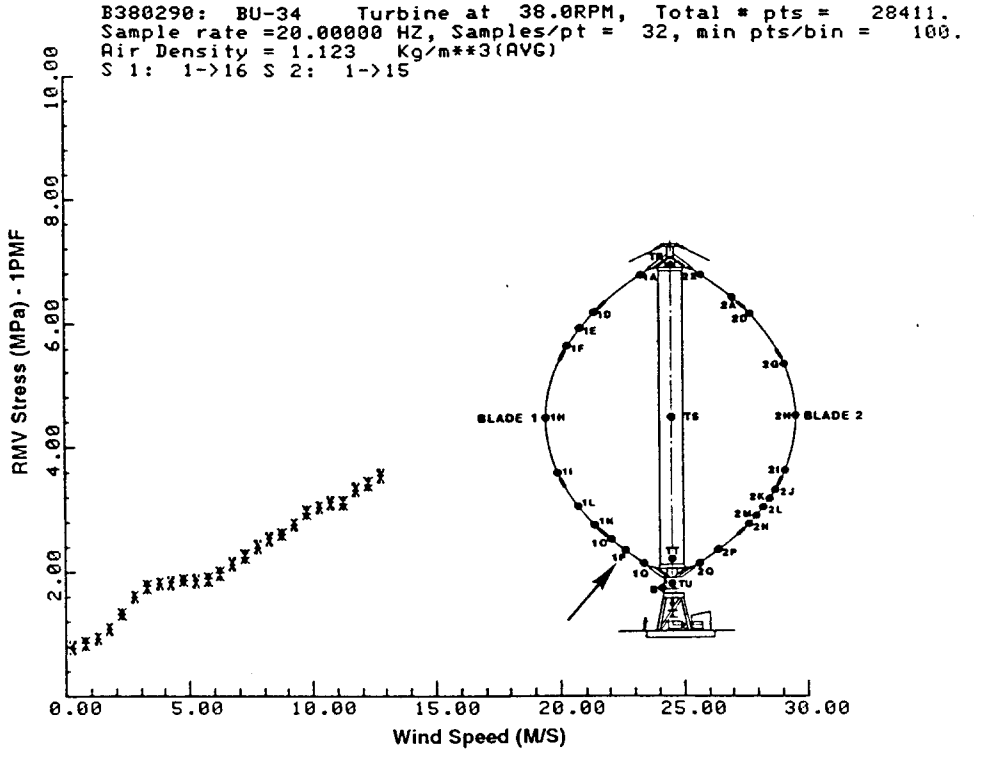

Figure C-16. RMV Stress vs. Wind Speed at 38 RPM - 1PMF

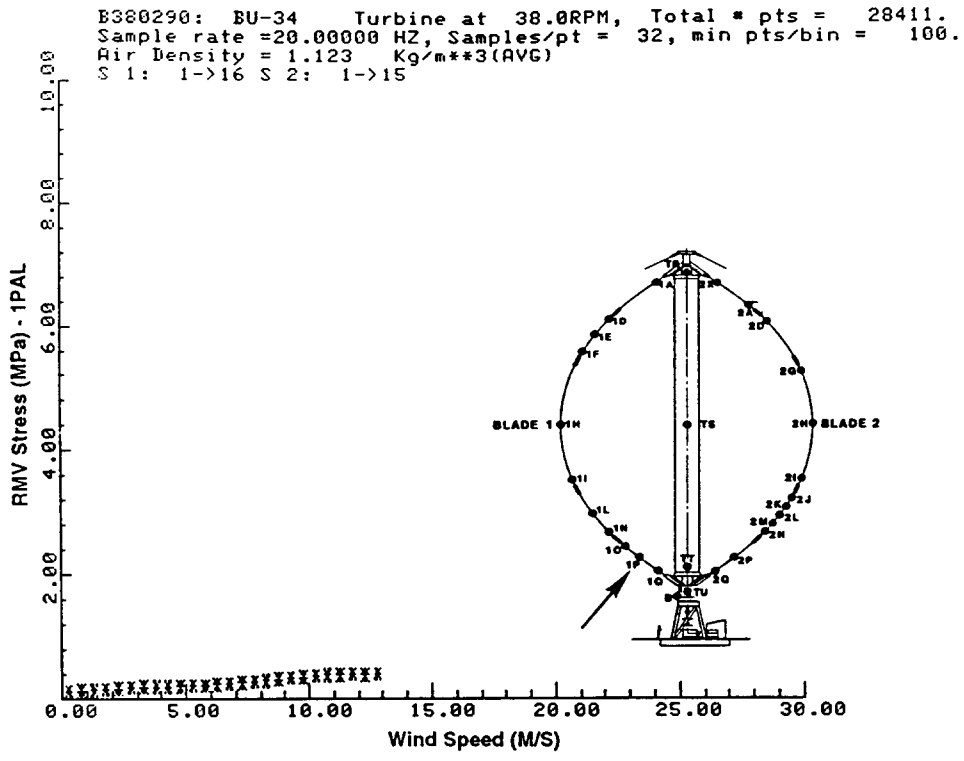

Figure C-17. RMV Stress vs. Wind Speed at 38 RPM - 1PAL

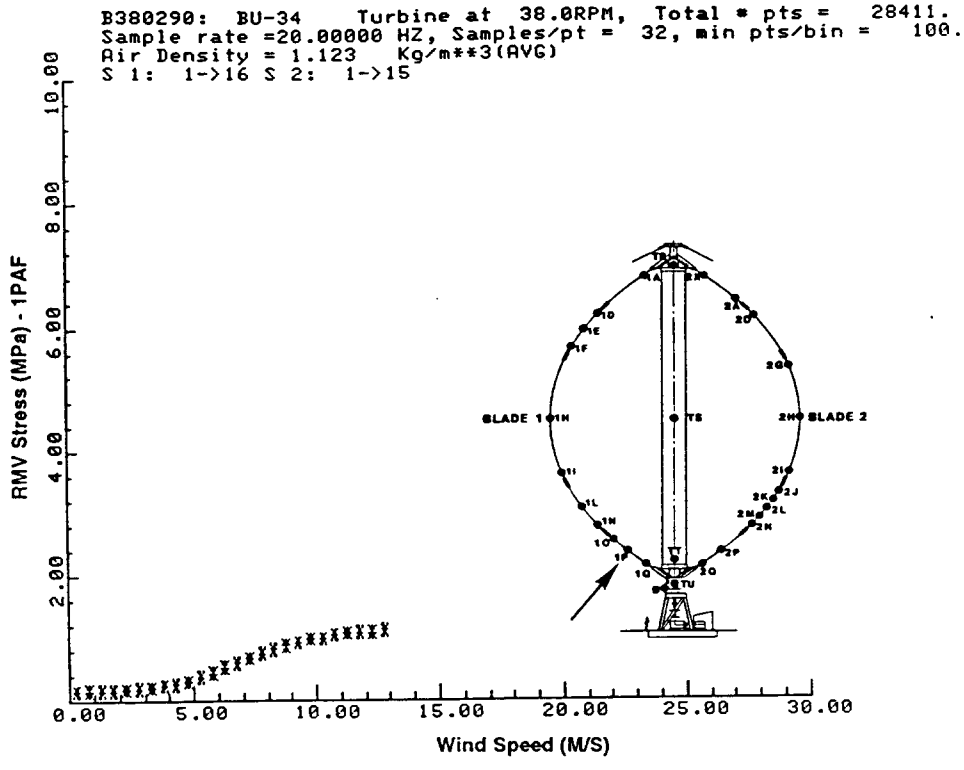

Figure C-18. RMV Stress vs. Wind Speed at 38 RPM - 1PAF

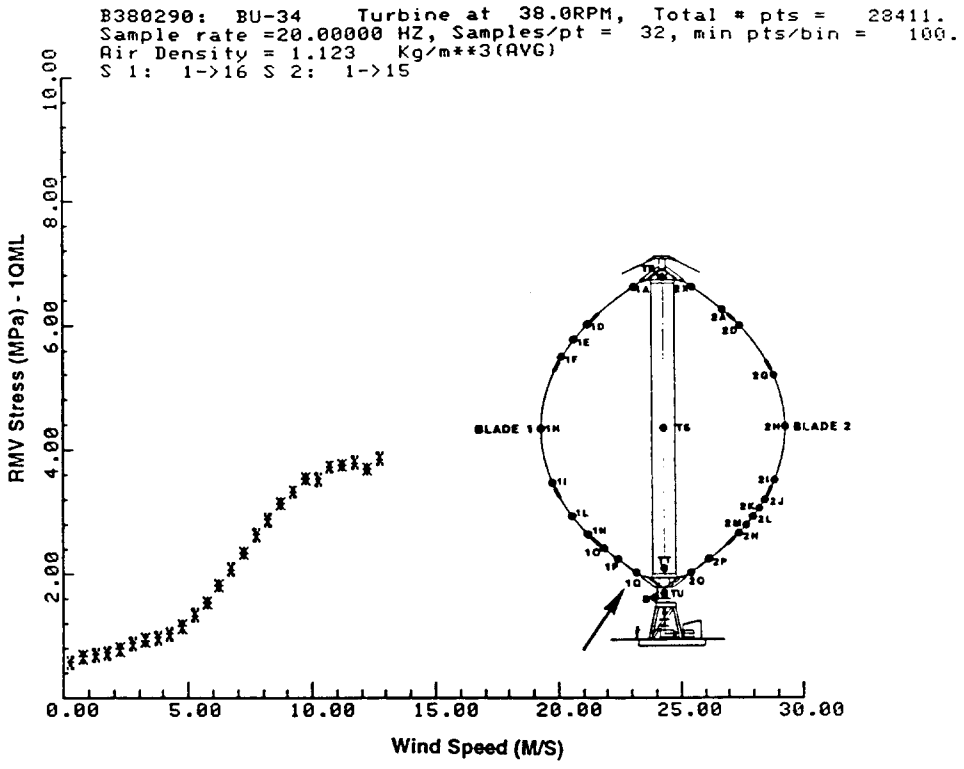

Figure C-19. RMV Stress vs. Wind Speed at 38 RPM - 1QML

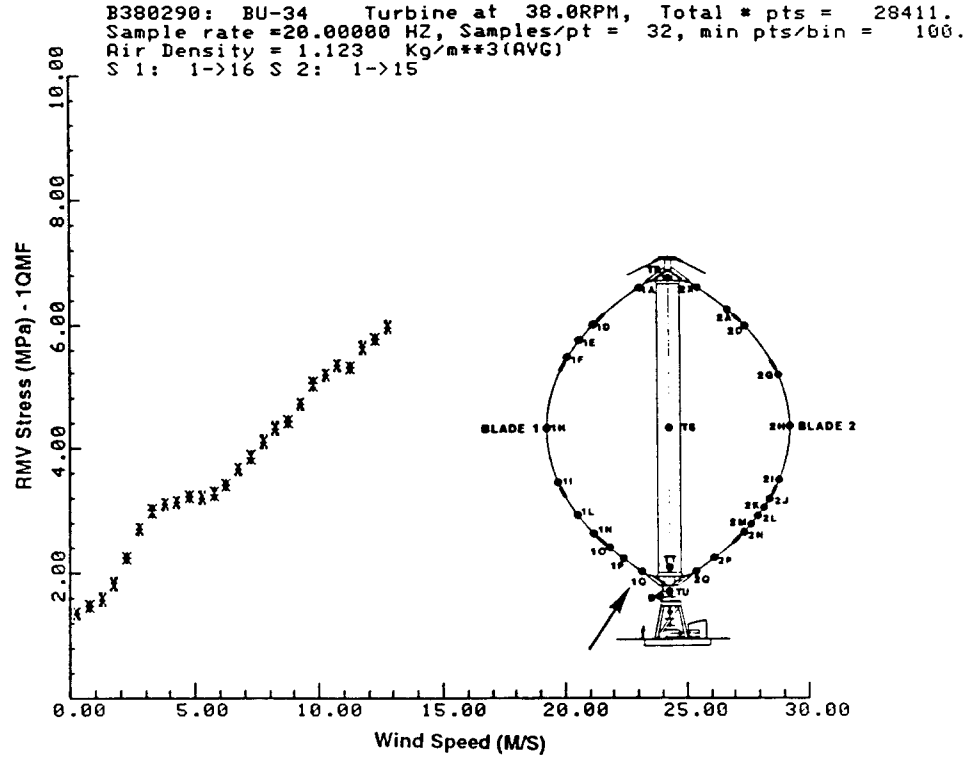

Figure C-20. RMV Stress vs. Wind Speed at 38 RPM - 1QMF

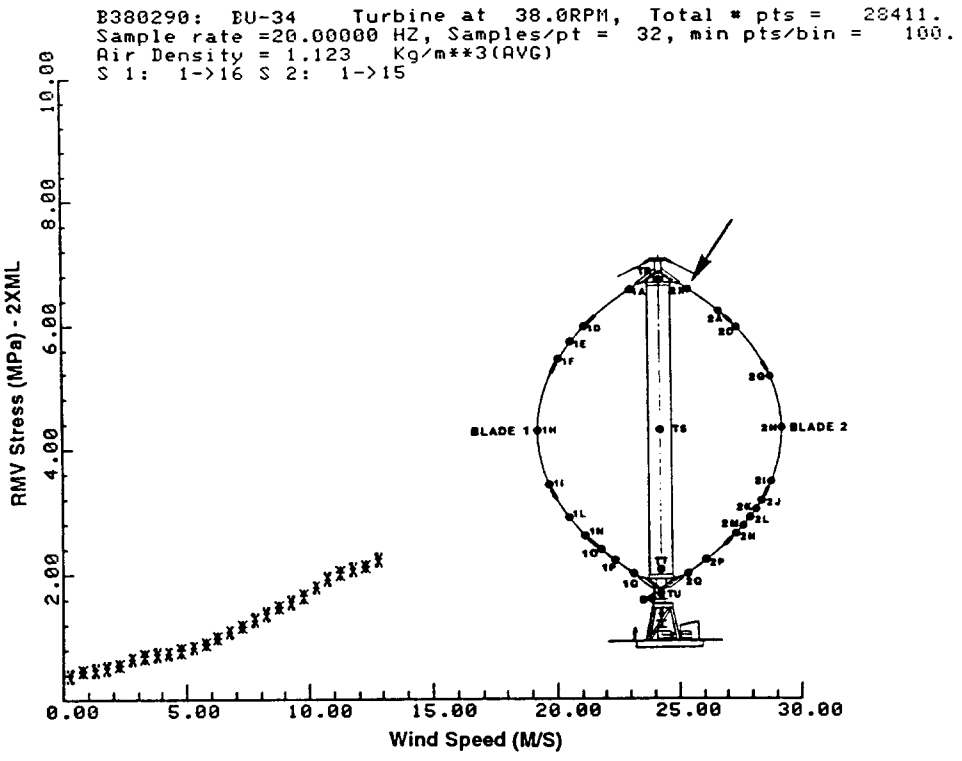

Figure C-21. RMV Stress vs. Wind Speed at 38 RPM - 2XML

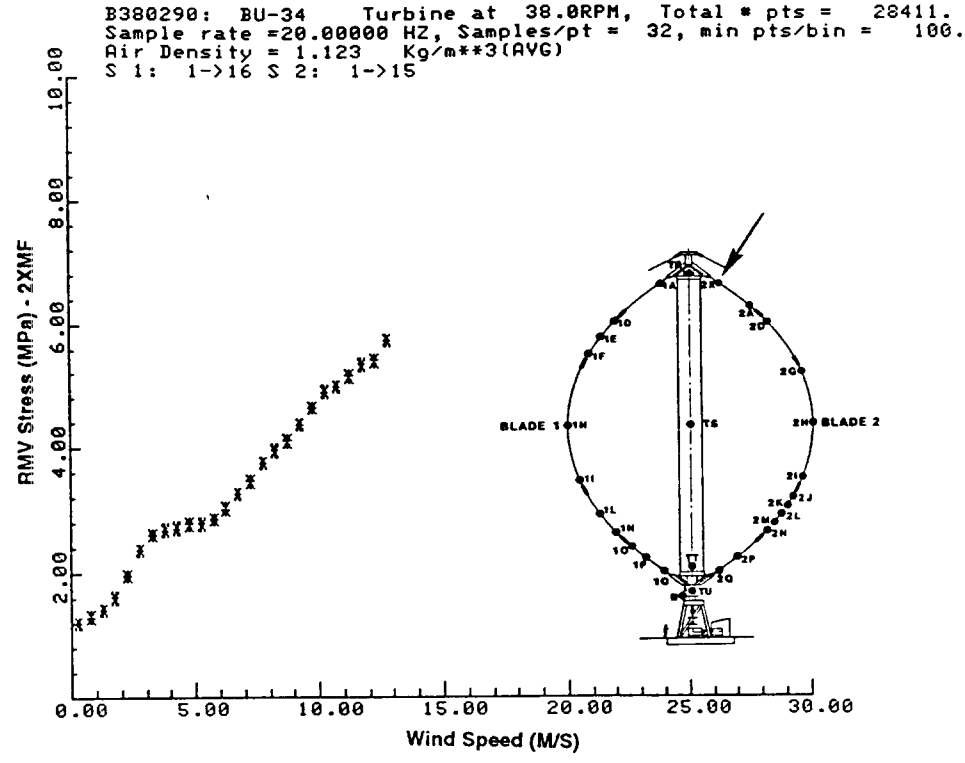

Figure C-22. RMV Stress vs. Wind Speed at 38 RPM - 2XMF

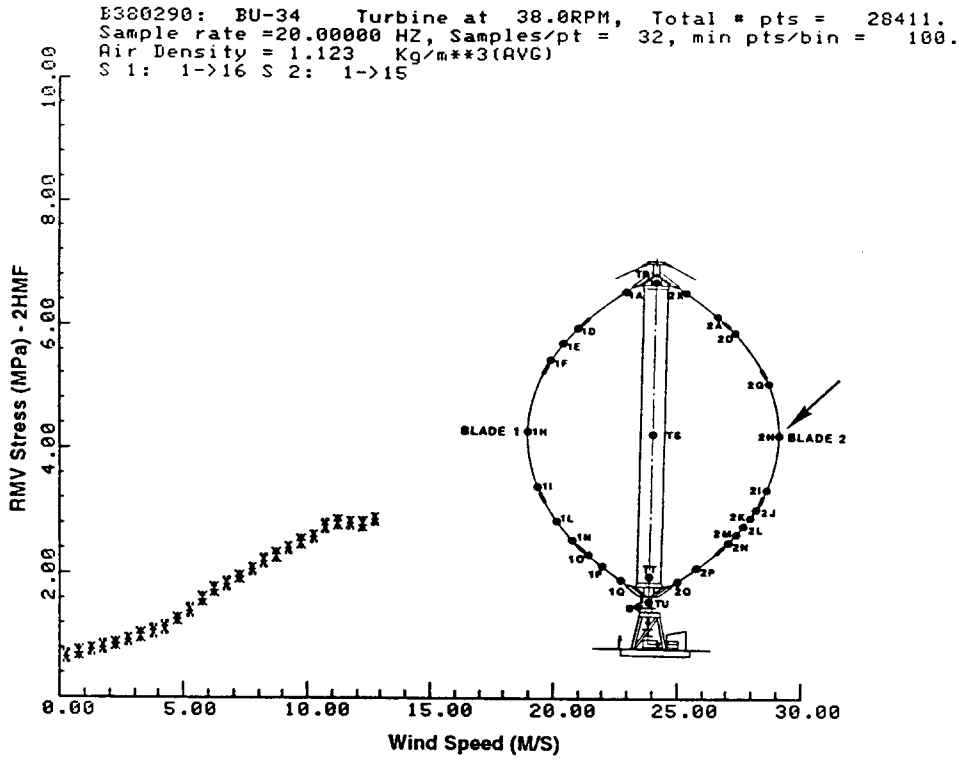

Figure C-23. RMV Stress vs. Wind Speed at 38 RPM - 2HMF

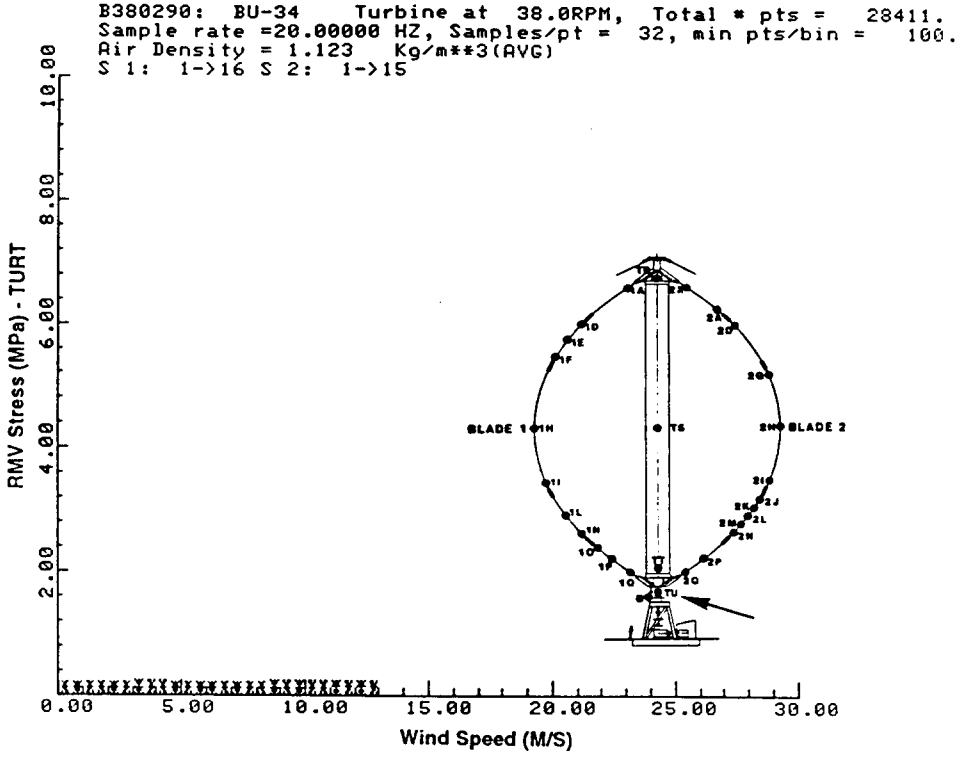

Figure C-24. RMV Stress vs. Wind Speed at 38 RPM - TURT

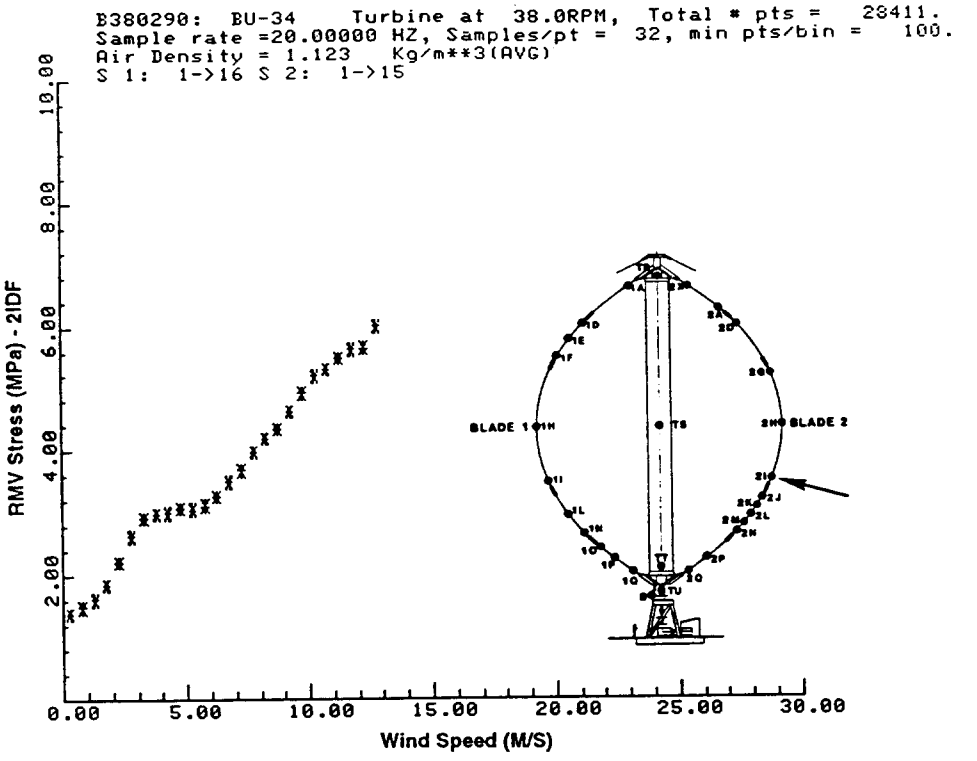

Figure C-25. RMV Stress vs. Wind Speed at 38 RPM - 2IDF

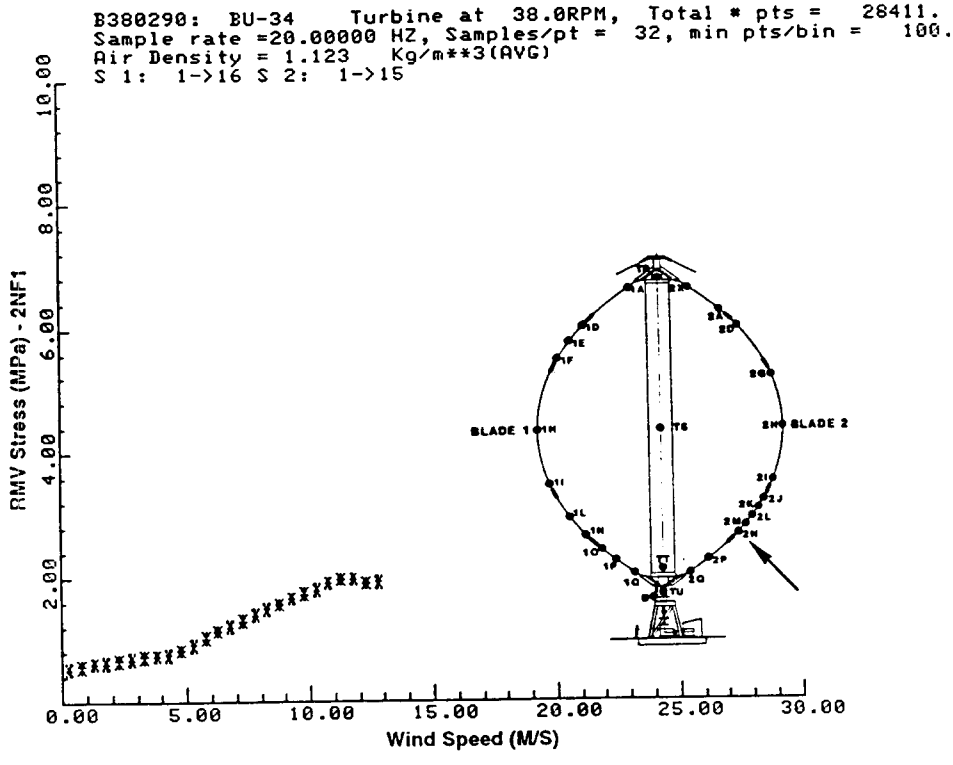

Figure C-26. RMV Stress vs. Wind Speed at 38 RPM - 2NF1

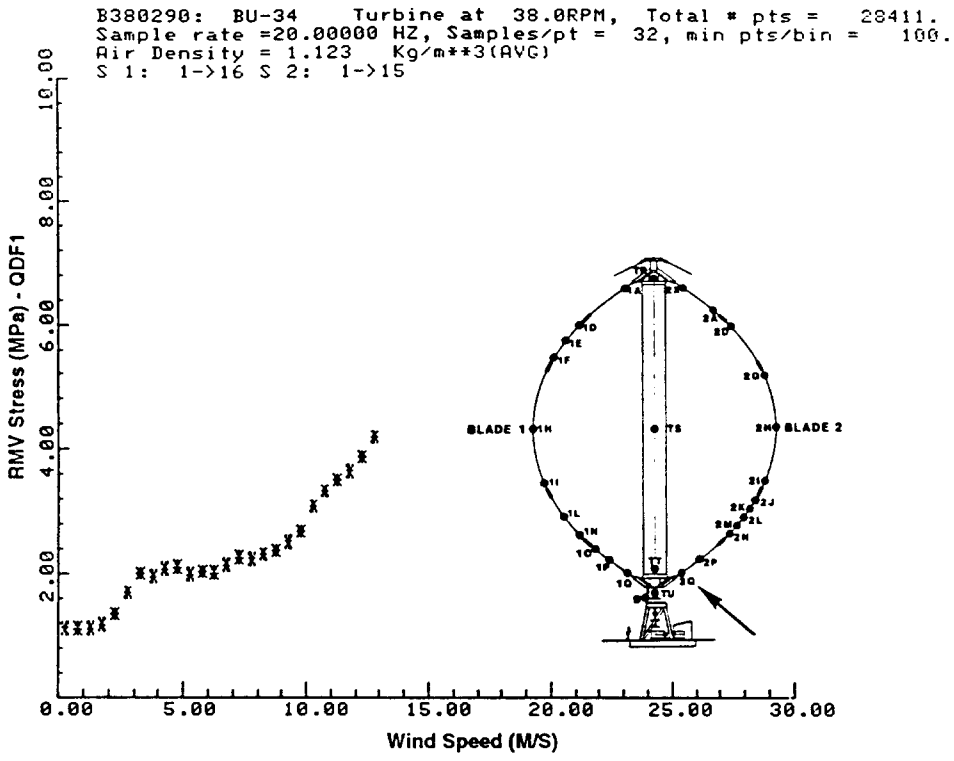

Figure C-27. RMV Stress vs. Wind Speed at 38 RPM - QDF1

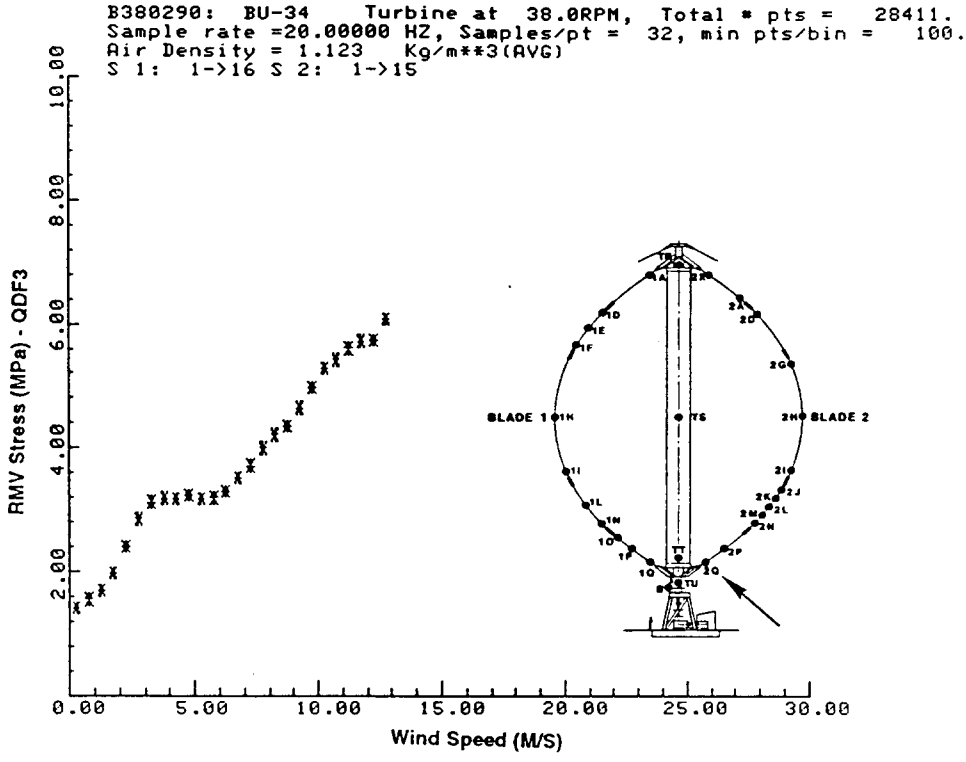

Figure C-28. RMV Stress vs. Wind Speed at 38 RPM - QDF3

DISTRIBUTION:

D. K. Ai
Alcoa Technical Center
Aluminum Company of America
Alcoa Center, PA 15069

Dr. R. E. Akins
Washington & Lee University
P.O. Box 735
Lexington, VA 24450

Dr. Mike Anderson
Renewable Energy Systems, Ltd.
Eaton Court, Maylands Avenue
Hemel Hempstead
Herts HP2 7DR
UNITED KINGDOM

Dr. M. P. Ansell
School of Material Science
University of Bath
Claverton Down
Bath BA2 7AY
Avon
UNITED KINGDOM

Holt Ashley
Dept. of Aeronautics and
Astronautics Mechanical Engr.
Stanford University
Stanford, CA 94305

K. Bergey
University of Oklahoma
Aero Engineering Department
Norman, OK 73069

Ir. Jos Beurskens
Programme Manager for
Renewable Energies
Netherlands Energy Research
Foundation ECN
Westerduinweg 3
P.O. Box 1
1755 ZG Petten (NH)
THE NETHERLANDS

J. R. Birk
Electric Power Research Institute
3412 Hillview Avenue
Palo Alto, CA 94304

N. Butler
Bonneville Power Administration
P.O. Box 3621
Portland, OR 97208

Dr. R. N. Clark
USDA
Agricultural Research Service
Southwest Great Plains Research
Center
Bushland, TX 79012

C. Coleman
Northern Power Systems
Box 659
Moretown, VT 05660

Otto de Vries
National Aerospace Laboratory
Anthony Fokkerweg 2
Amsterdam 1017
THE NETHERLANDS

E. A. DeMeo
Electric Power Research Institute
3412 Hillview Avenue
Palo Alto, CA 94304

C. W. Dodd
Universal Data Systems
5000 Bradford Drive
Huntsville, AL 35805

J. B. Dragt
Institute for Wind Energy
Faculty of Civil Engineering
Delft University of Technology
Stevinweg 1
2628 CN Delft
THE NETHERLANDS

A. J. Eggers, Jr.
RANN, Inc.
260 Sheridan Ave., Suite 414
Palo Alto, CA 94306

John Ereaux
RR No. 2
Woodbridge, Ontario L4L 1A6
CANADA

Dr. R. A. Galbraith
Dept. of Aerospace Engineering
James Watt Building
University of Glasgow
Glasgow G12 8QG
ENGLAND

A. D. Garrad
Garrad Hasson
9-11 Saint Stephens Street
Bristol BS1 1EE
ENGLAND

P. R. Goldman
Wind/Hydro/Ocean Division
U.S. Department of Energy
1000 Independence Avenue
Washington, DC 20585

Dr. I. J. Graham
Dept. of Mechanical Engineering
Southern University
P.O. Box 9445
Baton Rouge, LA 70813-9445

Professor G. Gregorek
Aeronautical & Astronautical
Dept.
Ohio State University
2300 West Case Road
Columbus, OH 43220

Professor N. D. Ham
Aero/Astro Dept.
Massachusetts Institute of
Technology
77 Massachusetts Avenue
Cambridge, MA 02139

Loretta Helling
Librarian
National Atomic Museum
Albuquerque, NM 87185

T. Hillesland
Pacific Gas and Electric Co.
3400 Crow Canyon Road
San Ramon, CA 94583

Eric N. Hinrichsen
Power Technologies, Inc.
P.O. Box 1058
Schenectady, NY 12301-1058

W. E. Holley
U.S. WindPower
6952 Preston Avenue
Livermore, CA 94550

M. A. Ilyan
Pacific Gas and Electric Co.
3400 Crow Canyon Road
San Ramon, CA 94583

K. Jackson
Dynamic Design
123 C Street
Davis, CA 95616

O. Krauss
Division of Engineering Research
Michigan State University
East Lansing, MI 48825

V. Lacey
Indal Technologies, Inc.
3570 Hawkestone Road
Mississauga, Ontario L5C 2V8
CANADA

A. Laneville
Faculty of Applied Science
University of Sherbrooke
Sherbrooke, Quebec J1K 2R1
CANADA

G. G. Leigh
New Mexico Engineering
Research Institute
Campus P.O. Box 25
Albuquerque, NM 87131

L. K. Liljegren
120 East Penn Street
San Dimas, CA 91773

R. R. Loose, Director
Wind/Hydro/Ocean Division
U.S. Department of Energy
1000 Independence Ave., SW
Washington, DC 20585

Robert Lynette
R. Lynette & Assoc., Inc.
15042 NE 40th Street
Suite 206
Redmond, WA 98052

Peter Hauge Madsen
Riso National Laboratory
Postbox 49
DK-4000 Roskilde
DENMARK

David Malcolm
R. Lynette & Associates, Inc.
15042 N.E. 40th Street, Suite 206
Redmond, WA 98052

Prof. J. F. Mandell
Montana State University
302 Cableigh Hall
Bozeman, MT 59717

Bernard Masse
Institut de Recherche d'Hydro-Quebec
1800, Montee Ste-Julie
Varennes, Quebec J3X 1S1
CANADA

Gerald McNerney
U.S. Windpower, Inc.
6952 Preston Avenue
Livermore, CA 94550

R. N. Meroney
Dept. of Civil Engineering
Colorado State University
Fort Collins, CO 80521

Alan H. Miller
NREL
1617 Cole Boulevard
Golden, CO 80401

R. H. Monroe
Gougeon Brothers
100 Patterson Avenue
Bay City, MI 48706

D. Morrison
New Mexico Engineering
Research Institute
Campus P.O. Box 25
Albuquerque, NM 87131

V. Nelson
Department of Physics
West Texas State University
P.O. Box 248
Canyon, TX 79016

J. W. Oler
Mechanical Engineering Dept.
Texas Tech University
P.O. Box 4289
Lubbock, TX 79409

Dr. D. I. Page
Energy Technology Support Unit
B 156.7 Harwell Laboratory
Oxfordshire, OX11 ORA
UNITED KINGDOM

Chuck Paquette
The American Wind Energy Association
777 N. Capitol Street, NE
Suite 805
Washington, DC 20002

Ion Paraschivoiu
Dept. of Mechanical Engineering
Ecole Polytecnique
CP 6079
Succursale A
Montreal, Quebec H3C 3A7
CANADA

Troels Friis Pedersen
Riso National Laboratory
Postbox 49
DK-4000 Roskilde
DENMARK

Helge Petersen
Riso National Laboratory
Postbox 49
DK-4000 Roskilde
DENMARK

Dr. R. Ganesh Rajagopalan
Assistant Professor
Aerospace Engineering Department
Iowa State University
404 Town Engineering Bldg.
Ames, IA 50011

Raj Rangi
Manager, Wind Technology
Dept. of Energy, Mines and Resources
580 Booth 7th Floor
Ottawa, Ontario K1A OE4
CANADA

Markus G. Real, President
Alpha Real Ag
Feldeggstrasse 89
CH 8008 Zurich
Switzerland

R. L. Scheffler
Research and Development Dept.
Room 497
Southern California Edison
P.O. Box 800
Rosemead, CA 91770

L. Schienbein
7080 Donlon Way, Suite 210A
Dublin, CA 94568

Thomas Schweizer
Princeton Economic Research, Inc.
12300 Twinbrook Parkway
Rockville, MD 20852

David Sharpe
Dept. of Aeronautical Engineering
Queen Mary College
Mile End Road
London, E1 4NS
UNITED KINGDOM

J. Sladky, Jr.
Kinetics Group, Inc.
P.O. Box 1071
Mercer Island, WA 98040

M. Snyder
Aero Engineering Department
Wichita State University
Wichita, KS 67208

L. H. Soderholm
Agricultural Engineering
Room 213
Iowa State University
Ames, IA 50010

Peter South
ADECON
6535 Millcreek Dr., Unit 67
Mississauga, Ontario L5N 2M2
CANADA

W. J. Steeley
Pacific Gas and Electric Co.
3400 Crow Canyon Road
San Ramon, CA 94583

Forrest S. Stoddard
West Texas State University
Alternative Energy Institute
WT Box 248
Canyon, Texas 79016

Derek Taylor
Alternative Energy Group
Walton Hall
Open University
Milton Keynes MK7 6AA
UNITED KINGDOM

G. P. Tennyson
DOE/AL/ETWMD
Albuquerque, NM 87115

Walter V. Thompson
410 Ericwood Court
Manteca, CA 95336

R. W. Thresher
NREL
1617 Cole Boulevard
Golden, CO 80401

K. J. Touryan
3701 Hawkins Street, NE
Albuquerque, NM 87109-4512

W. A. Vachon
W. A. Vachon & Associates
P.O. Box 149
Manchester, MA 01944

P. Vittecoq
Faculty of Applied Science
University of Sherbrooke
Sherbrooke, Quebec J1K 2R1
CANADA

T. Watson
Canadian Standards Association
178 Rexdale Boulevard
Rexdale, Ontario M9W 1R3
CANADA

L. Wendell
Battelle-Pacific Northwest
Laboratory
P.O. Box 999
Richland, WA 99352

W. Wentz
Aero Engineering Department
Wichita State University
Wichita, KS 67208

R. E. Wilson
Mechanical Engineering Dept.
Oregon State University
Corvallis, OR 97331

M. Zuteck
MDZ Consulting
931 Grove Street
Kemah, TX 77565

400	R. C. Maydew
1434	D. W. Lobitz
1434	D. R. Martinez
1511	G. F. Homicz
1514	J. G. Arguello
1514	H. S. Morgan
1540	J. R. Asay
1544	R. C. Reuter, Jr.
1545	C. R. Dohrmann
1552	J. H. Strickland
1562	K. E. Metzinger
1562	E. D. Reedy
2741	T. G. Carne
2741	G. H. James III
2741	J. P. Lauffer
2741	R. Rodeman
3161	P. S. Wilson
6000	D. L. Hartley
6214	H. M. Dodd (50)
6214	T. D. Ashwill
6214	D. E. Berg
6214	S. C. Newton
6214	M. A. Rumsey
6214	L. L. Schluter
6214	W. A. Stephenson
6214	H. J. Sutherland
6214	P. S. Veers
7141	S. A. Landenberger (5)
7151	G. C. Claycomb (3)
7613-2	Document Processing (8) For DOE/OSTI
8523-2	Central Technical Files

* U.S. GOVERNMENT PRINTING OFFICE 1992—774-122/80075